NORTH ATLANTIC TREATY ORGANISATION

RESEARCH AND TECHNOLOGY ORGANISATION

AC/323(SCI-040)TP/45

www.rta.nato.int

RTO AGARDograph 300 **SCI-040**
Flight Test Techniques Series – Volume 23

Flight Test Measurement Techniques for Laminar Flow

(Les techniques de mesure en vol des écoulements laminaires)

This AGARDograph has been sponsored by the

Flight Test Technology Team (FT3) of the

Systems Concepts and Integration Panel (SCI) of RTO.

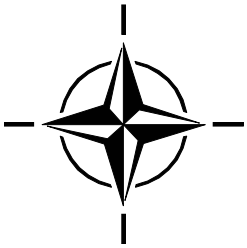

Published October 2003

This page has been deliberately left blank

Page intentionnellement blanche

NORTH ATLANTIC TREATY ORGANISATION

RESEARCH AND TECHNOLOGY ORGANISATION

AC/323(SCI-040)TP/45

www.rta.nato.int

RTO AGARDograph 300 **SCI-040**
Flight Test Techniques Series – Volume 23

Flight Test Measurement Techniques for Laminar Flow

(Les techniques de mesure en vol des écoulements laminaires)

Edited by D. Fisher, K.H. Horstmann and H. Riedel

This AGARDograph has been sponsored by the
Flight Test Technology Team (FT3) of the
Systems Concepts and Integration Panel (SCI) of RTO.

The Research and Technology Organisation (RTO) of NATO

RTO is the single focus in NATO for Defence Research and Technology activities. Its mission is to conduct and promote co-operative research and information exchange. The objective is to support the development and effective use of national defence research and technology and to meet the military needs of the Alliance, to maintain a technological lead, and to provide advice to NATO and national decision makers. The RTO performs its mission with the support of an extensive network of national experts. It also ensures effective co-ordination with other NATO bodies involved in R&T activities.

RTO reports both to the Military Committee of NATO and to the Conference of National Armament Directors. It comprises a Research and Technology Board (RTB) as the highest level of national representation and the Research and Technology Agency (RTA), a dedicated staff with its headquarters in Neuilly, near Paris, France. In order to facilitate contacts with the military users and other NATO activities, a small part of the RTA staff is located in NATO Headquarters in Brussels. The Brussels staff also co-ordinates RTO's co-operation with nations in Middle and Eastern Europe, to which RTO attaches particular importance especially as working together in the field of research is one of the more promising areas of co-operation.

The total spectrum of R&T activities is covered by the following 7 bodies:

- AVT Applied Vehicle Technology Panel
- HFM Human Factors and Medicine Panel
- IST Information Systems Technology Panel
- NMSG NATO Modelling and Simulation Group
- SAS Studies, Analysis and Simulation Panel
- SCI Systems Concepts and Integration Panel
- SET Sensors and Electronics Technology Panel

These bodies are made up of national representatives as well as generally recognised 'world class' scientists. They also provide a communication link to military users and other NATO bodies. RTO's scientific and technological work is carried out by Technical Teams, created for specific activities and with a specific duration. Such Technical Teams can organise workshops, symposia, field trials, lecture series and training courses. An important function of these Technical Teams is to ensure the continuity of the expert networks.

RTO builds upon earlier co-operation in defence research and technology as set-up under the Advisory Group for Aerospace Research and Development (AGARD) and the Defence Research Group (DRG). AGARD and the DRG share common roots in that they were both established at the initiative of Dr Theodore von Kármán, a leading aerospace scientist, who early on recognised the importance of scientific support for the Allied Armed Forces. RTO is capitalising on these common roots in order to provide the Alliance and the NATO nations with a strong scientific and technological basis that will guarantee a solid base for the future.

Published October 2003

ISBN 92-837-1107-6

Flight Test Measurement Techniques for Laminar Flow

(RTO AG-300 Vol. 23 / SCI-040)

Executive Summary

The advantages of laminar flow technology have been well known for decades. Experiments in Germany, the United Kingdom, and the United States date back to the 1930's. One application of some of the early research was the use of a laminar flow airfoil on the P-51 fighter aircraft.

Laminar flow can be obtained on an aircraft by shaping the airfoil and creating a favorable pressure gradient resulting in "Natural Laminar Flow," (NLF). Another method, "laminar flow control," (LFC) is to apply active suction through a porous surface, removing the local turbulence disturbances. A third method is to combine the two, using LFC near the leading edge and NLF on the aft portion of the airfoil. This is referred to as "Hybrid Laminar Flow Control."

Laminar flow technology is one that requires flight testing to obtain the proper noise environment, Reynolds number, scale, and environmental conditions. One of the most extensive laminar flow flight tests was performed on the X-21A in the 1960's by Northrop and the U.S. Air Force. Those tests used LFC in which small portions of the boundary layer near the surface were removed with suction through narrow slots in the skin. That technology was not adopted by the transport aircraft manufacturers because of the added weight and complexity of manufacturing and operating the systems, the low cost and availability of fuel at the time, and the lack of a good solution for the insect contamination problem.

However, the capability of manufacturing close tolerances today with computer-controlled milling machines, materials such as perforated titanium, and insect contamination alleviation techniques makes a laminar flow on a transport aircraft a closer reality.

This AGARDograph addresses proven flight test techniques that have been tested and applied over the last several decades. It illustrates the problems required to overcome, suggests equipment and instrumentation that might be used, and discusses environmental effects and flight test procedures. It provides options for obtaining good results using different flight test techniques, from very simple to more complex.

Les techniques de mesure en vol des écoulements laminaires

(RTO AG-300 Vol. 23 / SCI-040)

Synthèse

Les avantages des technologies de l'écoulement laminaire sont connus depuis des décennies. Les expériences réalisées en Allemagne, au Royaume-Uni et aux Etats-Unis datent des années 1930. L'une des applications de ces premiers travaux de recherche a été l'adoption d'un profil de voilure à écoulement laminaire sur l'avion de combat P-51.

En aéronautique, l'écoulement laminaire peut être obtenu en façonnant le profil de telle manière à créer un gradient de pression qui produit un « écoulement laminaire naturel » (NLF). Une autre méthode, appelée « contrôle de l'écoulement laminaire » (LFC) consiste à créer une dépression active à travers une surface poreuse, éliminant ainsi les perturbations locales occasionnées par les tourbillons. Une troisième méthode représente une combinaison des deux premières, et applique le LFC à une zone proche du bord d'attaque et le NLF à la partie arrière du profil de voilure. Cette méthode s'appelle « contrôle hybride de l'écoulement laminaire ».

La mise au point des technologies de l'écoulement laminaire nécessite la réalisation d'essais en vol afin d'obtenir les conditions de milieu sonore, de nombre Reynolds, d'échelle et d'environnement appropriées. L'un des essais en vol de l'écoulement laminaire le plus coûteux a été réalisé sur le X-21A dans les années soixante par Northrop et l'US Air Force. Ces essais ont fait appel au LFC. En l'occurrence, des petits morceaux de la couche limite proche de la surface ont été enlevés par la technique de dépression active à travers des fentes étroites pratiquées dans le revêtement. Cette technique n'était pas adoptée par les constructeurs d'avions de transport en raison du poids supplémentaire et de la complexité de la fabrication et de l'exploitation des systèmes, ainsi que du coût modéré du carburant et de sa grande disponibilité à l'époque, et du problème de contamination par les insectes.

Cependant, aujourd'hui, avec les tolérances serrées autorisées par les fraiseuses numériques, les matériaux tels que le titane perforé, et les techniques d'atténuation de la contamination causée par les insectes, l'application du concept d'écoulement laminaire aux avions de transport paraît de plus en plus faisable.

Cette AGARDographie examine des techniques d'essais en vol éprouvées, qui ont été essayées et mises en œuvre au cours des dernières décennies. Elle fait ressortir les problèmes qui sont à résoudre, propose différents équipements et de l'instrumentation susceptibles d'être mis en œuvre, et examine les effets sur l'environnement, ainsi que les procédures d'essais en vol. Elle présente différentes options de techniques d'essais en vol, permettant d'obtenir de bons résultats, allant du très simple au plus complexe.

Table of Contents

List of Figures

List of Tables

Nomenclature

Acronyms

AC, ac	Alternating current
ACEE	Aircraft energy efficiency program
AGL	Above ground level
ALT	Attachment line transition
ATC	Air traffic control
ATTAS	Advanced Technologies Testing Aircraft System
CFC	Carbon fiber composite
CFD	Computational Fluid Dynamics
CFI	Crossflow instability
DAST	Drone for aerostructural testing
DC, dc	Direct current
DLR	Deutsches Zentrum für Luft- und Raumfahrt
DNW	Deutsch-Niederländischer Windkanal
FAA	Federal Aviation Authority (U.S.)
FBPF	Fan blade passing frequency
F. S.	Fuselage station
FTF	Flight test fixture
GASP	Global atmospheric sampling program
HARV	High Alpha Research Vehicle
HLF	Hybrid laminar flow
HLFC	Hybrid laminar flow control
ICBM	Intercontinental ballistic missile
IR	Infrared
KIAS	Knots indicated airspeed
KKK	Kryo-Windkanal Köln
LC	Liquid crystal
LDA	Laser Doppler anemometer
LEFT	Leading-edge flight test
LF	Laminar flow
LFC	Laminar flow control
LSTM	Lehrstuhl für Strömungsmechanik der Universität Erlangen
LWK	Laminarwindkanal Stuttgart
L2F	Laser two-focus anemometer
MMO	Maximum operating Mach number
MOSFET	Metal-oxide-semiconductor field effect transistor
NIST	National Institute of Standards and Technology
NLF	Natural laminar flow
O. D.	Outside diameter

PCM	Pulse code modulation
PGME	Propylene glycol monomethyl ether
PRT	Platinum resistance thermometer
PSD	Power spectral density
PSE	Parabolized stability equations
RFI	Radio frequency interference
RMS	Root-mean-square
SPL	Sound pressure level
TACT	Transonic aircraft technology
TDC	Top dead center
TP	Test point
T-S	Tollmien-Schlichting
TSI	Tollmien-Schlichting instability
U.K.	United Kingdom
U.S.	United States
USAF	United States Air Force
VSTFE	Variable-Sweep Transition Flight Experiment

Symbols

A	Calibration constant in King's Law
a	Calibration constant in King's Law
B	Calibration constant in King's Law
B. L.	Boundary layer
b	Width of disturbance or step, calibration constant in King's Law
C_D	Drag coefficient
C_L	Lift coefficient
C_p	Pressure coefficient
c	Wing or HLF nacelle fan cowl chord length
C_d	Section drag coefficient
C'_f	Skin friction coefficient
C_l	Section lift coefficient
dB	Decibel
E	Anemometer output bridge voltage
E_{ac}	Aircraft electrical power voltage
E	Output voltage
$\overline{E}$	Output voltage mean value
e'	Fluctuating value of output voltage
f	Frequency
$G_x(f)$	Power spectral density function
g	Standard gravitational constant

H	Harmonic frequency
H, h	Altitude
h	Disturbance or step height, 0.06 mm
h_p	Pressure altitude
I	Current amperage
k	Thermal conductivity of the air
k_{crit}	Critical disturbance height
L	Lift
M	Mach number
Ma_∞	Free-stream flight Mach number
N_1	Engine fan speed, percent of maximum
N_{1C}	Corrected engine fan speed
n	Amplification factor exponent, exponent in King's Law
$p_{pr}/p_{t\infty}$	Traversing probe pressure normalized by free-stream total pressure
p	Pressure
p'	Fluctuating pressure
$p_{t,\infty}$	Free-stream total pressure
$p_{t,\text{probe}}$	Probe total pressure
q, q_∞	Free-stream dynamic pressure
R	Resistance
Re_c	Reynolds number based on chord length, c
$\text{Re}_{k,\,crit}$	Reynolds number based on critical disturbance height
Re_{Tr}	Reynolds number based on end of transition
Re_{tr}	Reynolds number based on beginning or onset of transition
Re_w	Reynolds number based on sensor wire diameter, w
Re_x	Reynolds number based on longitudinal coordinate, x
Re_Θ	Reynolds number based on attachment line momentum thickness, Θ
t_a	Temperature of the airflow
Tr_f	Boundary layer transition front location = $(x_{tr}/c + x_{Tr}/c)/2$
t_w	Nacelle wall temperature, temperatures of the hot-wire sensor
$t_{t\infty}$	Free-stream total temperature
Tu	Turbulence intensity
$Tu(u')$	Turbulence intensity based on velocity fluctuation, u'
$Tu(v')$	Turbulence intensity based on velocity fluctuation, v'
t	Temperature
u_k^*	Shear stress velocity
U	Local velocity
U	Flow velocity, velocity near edge of boundary layer
U_∞	Free-stream velocity, true airspeed

U_k	Velocity within the boundary layer at the disturbance height
u/*U*	Local to free-stream velocity ratio
u, *v*, *w*	Velocity components in the direction of the axes of the rectangular Cartesian system x, y, z
u', *v'*, *w'*	Velocity fluctuations associated with u, v, w respectively
V	Aircraft velocity
V_c	Calibrated velocity
x_{Tr}	Location at end of boundary layer transition
x_{tr}	Location at onset of boundary layer transition
x	Longitudinal coordinate measured from fan cowl leading edge
x, *y*, *z*	Rectangular Cartesian coordinates
x/c	Normalized longitudinal coordinate
x/L	Distance from cone apex normalized by cone length
α	Angle of attack
α_h	Heat transfer coefficient
β	Yaw angle
Δc_l	Lift coefficient increment
Δp	Differential pressure
Δt	Temperature error
ε_φ	Directional radiation
η_F	Flap angle
θ	Circumferential angle
Θ	Momentum thickness
λ	Heat conductivity of the fluid
ρ	Density
$\overline{(\rho u)'}/\overline{(\rho U_\infty)}$	Normalized mass flow fluctuations
σ	Sea level density ratio of the air, root-mean-square (RMS) gust velocity
τ_{0k}	Wall shear stress at the disturbance location
τ_w	Wall shear stress
$\bar{\tau}_w$	Mean shear stress
τ'_w	Fluctuating value of shear stress
ν	Kinematic viscosity
φ	Wing leading edge sweep angle, circumferential angle
Ω	Resistance, Ohms

Subscripts

IAS	Indicated airspeed
∞	Free-stream conditions
ρ	Density

AGARDograph Series 160 and 300

The Systems Concepts and Integration (SCI) Panel has a mission to distribute knowledge concerning advanced systems, concepts, integration, engineering techniques, and technologies across the spectrum of platforms and operating environments to assure cost-effective mission area capabilities. Integrated defence systems, including air, land, sea, and space systems (manned and unmanned) and associated weapon and countermeasure integration are covered. Panel activities focus on NATO and national mid- to long-term system level operational needs. The scope of the Panel covers a multidisciplinary range of theoretical concepts, design, development, and evaluation methods applied to integrated defence systems.

One of the technical teams formed under the SCI Panel is dedicated to Flight Test Technology. Its mission is to disseminate information through publication of monographs on flight test technology derived from best practices which support the development of concepts and systems critical to maintaining NATO's technological and operational superiority. It also serves as the focal point for flight test subjects and issues within the SCI Panel and ensures continued vitality of the network of flight test experts within NATO.

These tasks were recognized and addressed by the former AGARD organization of NATO in the form of two AGARDograph series. The team continues this important activity by adding to the series described below.

In 1968, as a result of developments in the field of flight test instrumentation, it was decided that monographs should be published to document best practices in the NATO community. The monographs in this series are being published as individually numbered volumes of the AGARDograph 160 Flight Test Instrumentation Series.

In 1981, it was further decided that specialist monographs should be published covering aspects of Volume 1 and 2 of the original Flight Test Manual, including the flight testing of aircraft systems. The monographs in this series (with the exception of AG 237, which was separately numbered) are being published as individually numbered volumes of the AGARDograph 300 Flight Test Techniques Series.

At the end of each AGARDograph 160 Flight Test Instrumentation Series and AGARDograph 300 Flight Test Techniques Series volume is an annex listing all of the monographs published in both series.

Acknowledgements

The authors would like to thank the following for their contributions to this AGARDograph: Mr. Richard E. Davis, NASA Langley Research Center, Hampton, VA USA, for Chapter 3.3, Atmospheric particulates and Chapter 4.6, Atmospheric particulate instrumentation; Dr. Stan Miley, Old Dominion University, Norfolk, VA USA and Harry Chiles, NASA Dryden Flight Research Center, Edwards, CA USA, for Chapter 4.2.3, Hot-film and hot-wire anemometry; and Mr. Clifford J. Obara, NASA Langley Research Center, Hampton, VA USA, for Chapter 4.2.8, Sublimating chemicals technique.

The authors would also like to thank Graphic Artist Justine Mack for the many figures and illustrations, and Editorial Assistants Angela Hammons and Anna Grayson for the final layout. The authors are especially grateful to Editor Muriel Khachooni for her helpful comments, hard work and persistence in seeing this AGARDograph to completion. All work at the NASA Dryden Flight Research Center, Edwards, CA USA.

The authors would also like to recognize the patience and support of the NATO Research Technology Agency Flight Test Technology Team, champions Mr. Hans Galleithner, DLR, Institute of Flight Research, Oberpfaffenhofen, Wessling, Germany and Mr. Glenn Bever, NASA Dryden Flight Research Center, Edwards, CA USA; LTC Scott Campbell, RTA/SCI Panel Executive, Neuilly-sur-Seine Cedex, France; members Prof. N. Alemdaroglu, Middle East Technical University, Ankara, Turkey, Prof. L.M.B. da Costa Campos, Instituto Superior Tecnico, Lisboa Codex, Portugal, Mr. Roger Crane, 412th Test Wing, Edwards AFB, CA USA, Mr. R. Detrick, Naval Test Wing Atlantic, Patuxent River, MD USA, Mr. J. Dumoulin, Centre d'Essais en Vol Base d'Essais d'Istres, Istres Air, France, Mr. R. Erdos, National Research Council of Canada, Ottawa, Ontario, Canada, Mr. Ir. R. Krijn, National Aerospace Laboratory (NLR), Amsterdam, The Netherlands, Mr. D. Morley, BAE SYSTEMS, Warton, Preston, England, Capt. Roberto Sabatini, Pratica di Mare, Pomezia (Roma), Italy, and Mrs. B. A. Wood, MoD Boscombe Down, Salisbury, Wiltshire, U.K.

This page has been deliberately left blank

Page intentionnellement blanche

1.0 Introduction

One of the technologies that has the potential for providing the greatest increase in aircraft efficiency is the reduction of the viscous drag of the wing and empennage. Maintaining laminar flow on 50 percent of the chord length results in one-half the amount of viscous drag compared to fully turbulent flow. For transport aircraft carrying up to 100 passengers this probably can be obtained using natural laminar flow. For larger aircraft active methods are necessary, such as local or full chord boundary layer suction.

Flight tests to explore the advantages of laminar flow date back to the 1930s with experiments in Germany [1], the United Kingdom [2], and the United States [3]. Table 1 lists publications describing many of the laminar flow flight tests to date [1-71].

The advantages of laminar flow technology are well-known and have been used extensively for more than 40 years in the design of high-performance sailplanes and much less frequently for light aircraft. The corresponding large number of experiences with sailplanes cover Reynolds numbers between 0.5 and 3 million and those with light aircraft up to nearly 8 million, both for unswept wings.

During World War II, the U. S. National Advisory Committee for Aeronautics (NACA) designed and tested low-drag laminar airfoils for the military. “In application, the laminar flow airfoil was used in the design of the wings for the North American P-51 Mustang, as well as some other aircraft. Operationally, the wing did not enhance performance as dramatically as tunnel tests suggested. For the best performance, manufacturing tolerances had to be perfect and maintenance of wing surfaces needed to be thorough. The rush of mass production during the war and the tasks of meticulous maintenance in combat zones never met the standards of NACA laboratories. Still, the work on the laminar flow wing pointed the way to a new family of successful high-speed airfoils,” Billstein. [72].

In the 1950s, Werner Pfenninger led successful flight tests using suction through thin slots in the wing to control the boundary layer. This method, referred to as laminar flow control (LFC), was first used in flight on the F-94 airplane and later on the swept-wing X-21A airplane. As a flight experiment, the X-21A aircraft was very successful, obtaining laminar flow at Reynolds numbers of up to 46 million. However, the technology to reliably manufacture wings to the close tolerances required was not available. In addition, the insect contamination problem at the leading edge had not been solved. Laminar flow control was considered in the design for the Lockheed C-5A airplane, Chuprun and Cahill, [73], but the lack of a requirement for a long-range aircraft and the low cost of fuel at the time offset the added weight, maintenance, and complexity of a laminar flow aircraft, Braslow [74].

After the energy crisis of the 1970s, the interest in laminar flow was revived and flight-testing resumed. The manufacturing problems regarding steps and gaps at joints and surface waves that plagued the X-21 have been solved with modern aircraft manufacturing techniques. The development and use of perforated titanium skins has been a huge improvement over the X-21–type slotted surfaces. The use of hybrid laminar flow control, where suction is used near the leading edge and natural laminar flow is used to midchord of the airfoil, may be used and exploited in a future transport. A leading-edge Krueger flap device has been shown to be effective in protecting the leading edge from insect contamination. Anti-ice devices have also been developed for a laminar flow aircraft. Still, there is a large risk for an aircraft manufacturer to undertake a new aircraft with LFC or hybrid LFC, trading off the additional costs of manufacturing complexity, LFC systems, and aircraft maintenance, with the cost of savings in fuel.

The exploitation of laminar flow technology on transport aircraft will require a large investment. It will require new designs, ground tests, and many flight tests to maximize the benefits of laminar flow. The content of this AGARDograph may help to select the best equipment and techniques to measure the benefits of laminar flow.

Table 1.0 Laminar Flow Control Flight Tests

Publication Dates	Country	Experiment/ aircraft	Experimenters/ Authors	Techniques	Reference	Comments
1934	Germany	Klemm L26 Va	Stüper	Traversing probe through B.L., raised pitot	1	NLF
1938	U.K.	Farnborough/ Cambridge flight tests, Aircraft not identified.	B. Melvill Jones	B.L. rake, surface pitot	2	NLF
1939	U.S.	NACA, Northrop A-17A	J. Bicknell	Surface pitot, traversing wake probe	3	NLF
1941	U.S.	NACA, B-18 laminar flow airfoil	J.W. Wetmore, J.A. Zalovcik, R.C. Platt	B.L. and wake rakes, raised pitot	4	NLF
1945	U.S.	P-47D	J. A. Zalovcik	B.L. and wake rake	5	NLF
1950-52	U.K.	ARC, Kingcobra, Hurricane	F. Smith, D. J. Higton, R. H. Plascott, A. R. Bramwell	Wake rake	6,7	NLF
1957	U.S.	F-94	W. Pfenninger, E.E. Groth, B.H. Carmichael, R. C. Whites	B.L. rake, surface total pressure probe microphones, china clay, fluorene	8	LFC
1958-1959	U.S.	F-104	J.G. McTigue, R.D. Banner, J.D.Overton, G. Petty, Jr.	Chemical sublimation, heated temperature resistance gages	9,10	Supersonic NLF
1964-1966	U.S.	Northrop X-21A	W. Pfenninger, R.W. Sudderth, W.G. Wheldon, R.C. Whites, R.F. Carmichael, D.E. Pelke, E. Groth	B.L. and wake rakes, raised pitots, microphones	11–14	LFC
1966	U.K	Lancaster, Lincoln	R.R. Landeryou, P.G. Porter, M. Gaster	Hot films, B.L. rakes, surface probes, B.L. traversing probe	15	LFC
1978	U.S.	JetStar	D.F. Fisher, J.B. Peterson	Raised pitot	16	NLF
1979-1985	U.S.	F-111	L.J. Runyan, L.L. Steers, L.C. Montoya, B. Trujillo, R.R. Meyer, L.A. Jennett	Oil flows	17–20	NLF

Table 1.0 Laminar Flow Control Flight Tests (cont.)

Publication Dates	Country	Experiment/ aircraft	Experiments/ Authors	Techniques	Reference	Comments
1984	U.S.	Rutan VariEze, Rutan Long-EZ, Rutan Laser, Biplane Racer, Gates Learjet Model 28/29 Longhorn, Cessna P-210 Centurian, Beech 24R Sierra, Bellanca Skyrocet II, Beech T-34C gloves	B.J. Holmes, C.J. Obara, L.P. Yip	Chemical sublimation, surface total pressure tubes connected to observer earplug	21	NLF
1984-1986	U.S.	Cessna Citation III, Model 650	R.A. Rozendaal, W.H. Wentz, A. Ahmed, R. Nyenhuis	Hot Films, Chemical sublimation	22–24	NLF
1987	U.S.	JetStar	D.F. Fisher, M.C. Fischer, A.G. Powell, R.E. Davis, D.V. Maddalon, R.D. Wagner, L.A. Jennett, A.L. Braslow	Raised pitot, Knollenberg probe, charging patch	25–29	LFC
1987	Germany	SB13 sailplane wing Do 228 TNT propeller, BO105 helicopter rotor blades, LFU205 wing glove	H. Körner, K.H. Horstmann, H. Köster, A. Quast, G. Redeker	Oil flow, surface static pressure Surface static pressure Acenaphthene IR imaging, surface static pressure	30, 31	NLF
1980s	U.S.	B-757	L.J. Runyan, G.W. Bielak, R.A. Behbehani, A.W. Chen, R. A. Rozendaal	Microphones, Hot films	32	NLF
1987-1990	U.S.	F-14	R.R. Meyer, B. Trujillo Anderson, D.W. Bartlett, H.R. Chiles, F.S. Collier, Jr., V.V. Tat, R.D. Wagner	Hot films, boundary-layer rakes, surface pitot tubes, liquid crystals	33–38	NLF

Table 1.0 Laminar Flow Control Flight Tests (cont.)

Publication Dates	Country	Experiment/ aircraft	Experiments/ Authors	Techniques	Reference	Comments
1987-1991	Germany	VFW614/ ATTAS wing glove	K. H. Horstmann, G. Redeker, A. Quast, U. Dressler, H. Bieler, H. Köster, P. Thiede, J. Szodruch, H. P. Kreplin, G. Hoehler	IR imaging, surface static pressure, hot films, roughness elements	40, 41, 43	NLF
1988-1992	Germany	LFU205 wing glove	K. H. Horstmann, A. Quast, G. Redeker, U. Dressler, H. Bieler, H. Köster, P. Thiede, J. Szodruch, H. Körner, H. P. Kreplin, G. Hoehler, S. Miley	IR imaging, surface static pressure, hot film, hot wires	39–46	NLF
1992-1996	Germany	Do 228 wing glove	K.H. Hortsmann, R. Müller, C.H. Rohardt, A. Quast, H. Echtle, W. Wohlrath, P. Dick, D. Welte, H.W. Stock, B. Moeken, H. Körner, B. Wagner	IR imaging, wake rakes, surface static pressure, hot film	47–49	NLF
1992	France	Dassault Falcon 50, NLF stub wing on truncated fin, HLF wing glove	C. Bulgubure, D. Arnal	IR imaging, hot films, wake rake, surface static pressure, IR imaging, hot films, video cameras	50	NLF HLF
1996	Italy	Piaggio P180	G. Sacco, I.A.M.R. Piaggo	Sublimating chemicals, boundary layer tripping	51	NLF
1996	European Community	Fokker 100 wing glove	N. Voogt	IR imaging, hot films, surface static pressure, wake rakes	52	NLF
1996	Russia	Tupolev Tu-22M wing glove	A. Bolsunowsky, N. Buzoverya, A. Kotscheev, G. Cheryemukkin, A. Shapiro, Yu. Zavershnev, M. Tabulov, V. Turitschev	Hot films, surface static pressure	53	NLF

Table 1.0 Laminar Flow Control Flight Tests (cont.)

Publication Dates	Country	Experiment/ aircraft	Experiments/ Authors	Techniques	Reference	Comments
1992-2000	European Community	Airbus A320 fin	J.J. Thibert, A. Quast, J.P. Robert, W. Kühn, T. Strahmann, G. Höhler, J.C. Ghnassia, T. Kuon, V. Rouquière, R. Henke, C. Capbern, A.T. Davies, R. Hinsinger, T.L. Santana, G. H. Schrauf	IR imaging, hot films, surface static pressure, wake rakes, boundary layer rakes, trailing cone, pressure belts	54–58	HLF
1999	Germany	Grob 109B	S. Becker, F. Durst, H. Lienhart, B. Ewald, E. Krause, W. Nietsche	Laser Doppler anemometer, hot-film, piezo array, computational Preston tube	59 60	NLF NLF
1990s	U.S.	F-16XL	B. Trujillo Anderson, M. Bohn-Mayer, L.A. Marshall	Hot films	61, 62	Supersonic LFC
1990s	U.S.	Pegasus® Wing Glove	A. Bertelrud, G. de la Tova, P.J. Hamory, R. Young, G.K. Noffz, M. Dodson, S.S. Graves, J.K. Diamond, J.E. Bartlett, R. Noack, D. Knoblock	Hot films	63	Hypersonic NLF
Nacelles						
1986-87	U.S.	OV-1B w/NLF nacelle	C.J. Obara, E.C. Hastings, Jr., J.A. Schoenster, T.L. Parrot, B.J. Holmes, G.K. Faust, P. Mungur, S.S. Dodbele, M.G. Jones	Sublimating chemicals, liquid crystals, surface, static pressure, microphones	64, 65	NLF
1992 1996 1996	Germany U.K.	VFW614/ ATTAS nacelle	P.P. Shipley, N.T. Birch, H. Riedel, K.H. Horstmann, P. Lücking, M. Sitzmann	IR imaging, surface static pressure, surface temperature, hot films, liquid crystals, accelerometers, probe microphones, Kulite transducer, boundary layer rakes, base pressure	66, 67	NLF

Table 1.0 Laminar Flow Control Flight Tests (concl.)

Publication Dates	Country	Experiment/ aircraft	Experiments/ Authors	Techniques	Reference	Comments
1994 1996 1999	Germany U.K.	VFW614/ ATTAS nacelle	B. Barry, S. J. Parke, N.W. Bown, H. Riedel, M. Sitzmann, A.J. Mullender	IR imaging, surface static pressure, surface temperature, hot films, liquid crystals, accelerometers, probe microphones, Kulite transducer, boundary layer rakes, base pressure	68–70	DATUM (conventional) HLF (gloves)
1996	U.S.	Airbus A300	F.W. Tegarden	IR imaging, surface static pressure, hot films	71	HLF (gloves)

2.0 Boundary Layer Transition and Laminar Flow Concepts

2.1 Transition mechanisms and transition prediction

Modern transonic transport aircraft are characterized by a swept wing resulting in high cruise speed and high efficiency. Because of the wing sweep angle, the boundary layer is highly three-dimensional and several instability mechanisms of the laminar boundary layer can cause transition. Figure 2.1-1 gives an overview of the flow in the boundary layer of a swept wing. The incoming flow can be split into spanwise and chordwise components. The spanwise component induces a finite velocity at the attachment line along the leading edge. The streamlines just outside of the boundary layer are highly curved in the planform plane at the leading edge region as a result of pressure gradients transverse to the local flow direction. The boundary layer flow with low velocities near the wing surface is much more affected by these pressure gradients, as indicated in figure 2.1-1 by the full and the dotted lines. This behavior leads to skewed velocity profiles in the boundary layer where the flow direction and the flow velocity are changing with the distance from the wall. Splitting up these velocity profiles in the direction of the outer flow and perpendicular to it, a streamwise and a crossflow velocity distribution can be obtained, as also shown in figure 2.1-1. The streamwise velocity profile is very similar to that of a two-dimensional flow, whereas the crossflow profile shows a different shape. It is characterized by a maximum near the surface, decreasing to zero at the surface and at the outer edge of the boundary layer including a point of inflexion. These complicated flow patterns considerably influence the transition of the laminar flow on swept wings. Essentially the following three transition mechanisms, or combinations of them, can occur:

- Transition resulting from or caused by Tollmien-Schlichting instability (TSI)
- Transition resulting from or caused by crossflow instability (CFI)
- Attachment line transition (ALT)

In the case of Tollmien-Schlichting instability (TSI), unstable waves grow in the flow direction and lead through a complicated process to transition and turbulent flow. The governing parameters are the pressure gradient in flow direction and the Reynolds number, see Schlichting [75]. The stronger the pressure-drop in the chord direction the higher the stability of the boundary layer and the farther the extension of the laminar flow. With increasing Reynolds number the stability of the boundary layer is reduced, as is the extent of the laminar flow.

For crossflow instability (CFI), the travelling waves across the main flow direction or stationary vortices in the flow direction that occur are governed by the sweep angle, the pressure gradient in flow direction, and the Reynolds number, see Cumpsty and Head [76]. Increasing the wing sweep angle induces larger crossflow rates accompanied by stronger crossflow instability. The same mechanism appears with increasing pressure-drop. High Reynolds numbers lead, like TSI, to increasing instability.

For attachment line transition (ALT) the spanwise flow along the attachment line can become unstable and turbulent depending on leading-edge sweep angle, leading-edge radius (flow acceleration in the attachment line region) and Reynolds number, see Poll [77]. Increasing leading-edge sweep angle, increasing leading-edge radius, and increasing Reynolds number induce increasing instability. In the case of leading-edge transition, the result will be a fully turbulent boundary layer covering the entire wing surface.

For transition prediction many different methods exist. For low Reynolds numbers and unswept wings several empirical relations have been used successfully, e.g. Granville [78]. For high Reynolds numbers and swept wings a more reliable procedure that can determine the transition location governed by TSI or CFI is the application of laminar boundary layer linear local stability theory. Starting at the line of neutral stability, the amplification rates of disturbances at given wavelengths and frequencies are calculated, integrated to provide amplification ratios along the surface, and finally expressed by an amplification exponent N (N-factor) of the envelope (consisting of all wavelength-frequency combinations along the surface). The

maximum limiting N-factor indicating transition must be determined empirically by stability analysis of a measured pressure distribution and the subsequent evaluation of the N-factor at the measured transition location. For validation it is necessary to compare theory and experiment for many different flow conditions.

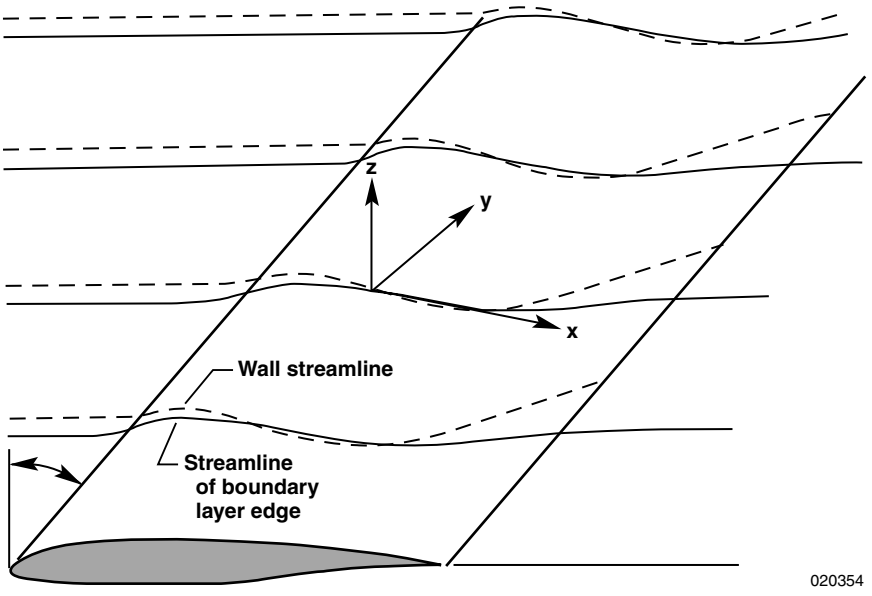

(a) Overview.

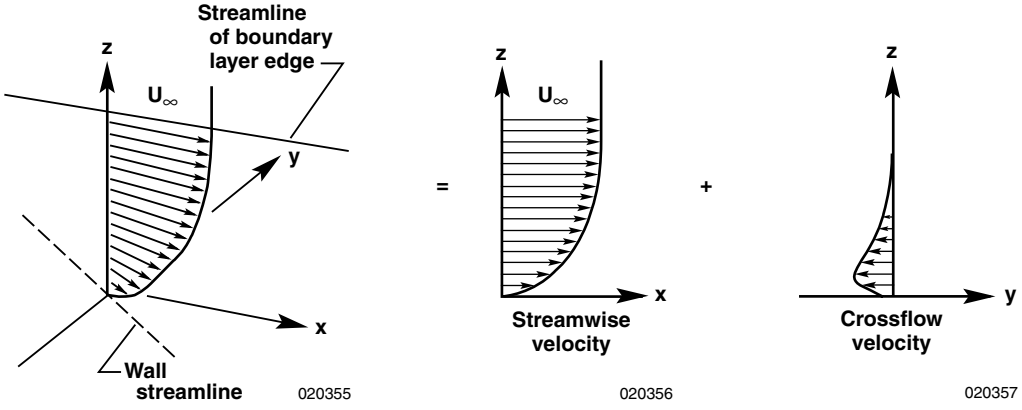

(b) Boundary layer edge. (c) Streamwise. (d) Crossflow.

Figure 2.1-1. Flow pattern and boundary layer velocity distribution on an infinite swept wing.

In the last two decades stability methods have been developed that describe the transition phenomenon more accurately than the local linear stability theory. The *nonlocal linear stability theory* takes into account curvature, compressibility effects, and the flow equation perpendicular to the surface. The *nonlocal nonlinear stability theory* (PSE) is able to compute the interference of different instability modes and their nonlinear behavior until transition. In principle these methods allow the theoretical determination of the transition location if a useful set of initial disturbances can be supplied as input data.

Several wind tunnel and flight tests have shown that the reliability and the dependency of the transition criterion on other parameters (such as Reynolds number and Mach number) of these sophisticated methods are not better than those of the simple local linear methods. Further, it could be shown that it is recommendable to use a 2-N-factor criterion, one for TSI in flow-direction and one for CFI in cross-direction, leading to a diagram as sketched in figure 2.1-2, [79].

As to attachment line transition, Cumpsty and Head [76], Pfenninger [13], and Poll [77] have shown that the transition phenomenon depends on the momentum thickness Reynolds number, Re_Θ, based on the attachment line momentum thickness, Θ. In early flight and wind tunnel experiments Pfenninger and Poll showed that the attachment line boundary layer remains laminar and stable as long as

$$Re_\Theta < 100.$$

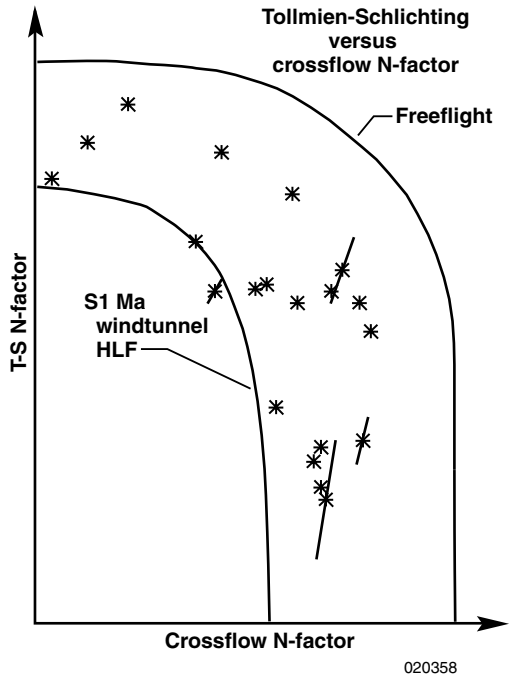

Figure 2.1-2. Limiting N-factors for laminar flow due to unstable waves induced by Tollmien-Schlichting instability (TSI) and crossflow instability (CFI) calculated by means of the linear stability theory and measured transition locations in flight and in a wind tunnel, respectively.

2.2 Concepts for laminar flow

Sailplanes and small general aviation aircraft that have small sweep angles of the leading edge on wing and tail planes and also have ultrasmooth surfaces tend to have a certain range of natural laminar boundary layer (NLF, natural laminar flow) starting at the leading edge and extending downstream to a chord position that depends on the shape of the local pressure distribution and on the local Reynolds number. At the small Reynolds numbers of sailplanes, ranging typically from 0.5 to 3.0 million, the laminar flow can extend downstream to chord locations between 50 percent and 90 percent. To achieve these values the section geometry needs a special design and the surface has to be smoothed with 1000–grit sandpaper.

Figure 2.2-1 shows the lift coefficient versus drag coefficient of a typical sailplane airfoil. In a certain range of lift coefficients the drag of a laminar airfoil amounts to one-half of the value of a fully turbulent one. The width of the lift range of low drag of the laminar drag bucket amounts to about $\Delta c_l = 0.6$ to 1.0, mainly depending on airfoil thickness and Reynolds number. At the high Reynolds numbers the width of the laminar drag bucket becomes smaller. The limits of the NLF concept has been shown with the NLF experiment on the Fokker F100 aircraft. The F100 wing has a leading edge sweep angle of 21° and enables Reynolds numbers up to more than 25 million. At these high Reynolds numbers the width of the laminar drag bucket is strongly reduced to $\Delta c_l = 0.2$.

At moderate to high Reynolds numbers, and sweep angles, or both, the boundary layer has to be controlled actively to maintain laminar flow. This is called LFC (laminar flow control) and is achieved by applying suction through the surface on the boundary layer. The flow can be sucked off through small slots in the surface arranged in the spanwise direction. This was first tested in flight by W. Pfenninger [11].

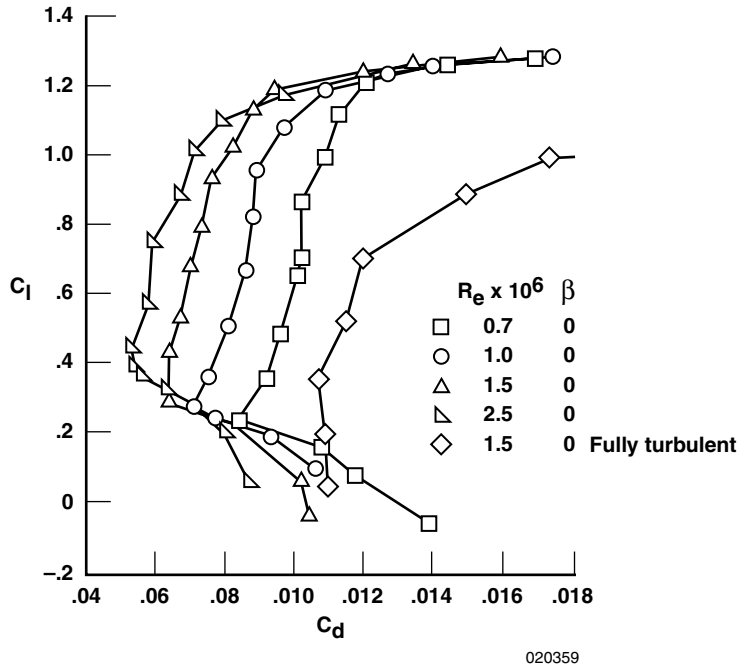

Figure 2.2-1. Typical lift coefficient versus drag coefficient behavior of a laminar flow airfoil at Reynolds numbers between 1 and 3 million.

Another possibility is to suck off the flow through a porous surface of small narrowly spaced holes. Typical values of the diameter of these holes amount to about 50 μm combined with a spacing of about 0.5 mm. This technique was not possible until laser drilling technology was developed. The first flight tests with applied hole suction were also performed by Werner Pfenninger [13].

By applying boundary layer suction, all three types of instabilities of the laminar boundary layer (Tollmien-Schlichting, crossflow, and attachment line) can be stabilized and the point of transition shifted downstream. If suction is applied along the whole wing chord, the boundary layer can be kept laminar up to the trailing edge. In the region of the wing box a suction system would substantially reduce the height of the wing box and thus markedly increase the weight of the wing.

This disadvantage can be avoided using hybrid laminar flow control (HLFC), by which suction is only applied in the region of the leading edge box. Thus, with an appropriate airfoil contour, and depending on Reynolds number and leading edge sweep angle, the flow can be kept laminar up to about 50 percent of chord length. Only the suction system itself, located in the leading edge box, causes additional weight; whereas the wing box remains unchanged. Such an HLFC system was proven in the laminar flow flight tests with the Boeing 757 (wing) [32] and the Airbus A320 (fin) [58].

This page has been deliberately left blank

Page intentionnellement blanche

3.0 Experimental Boundary Conditions

In order to obtain the full benefit of the application of laminar flow technology, and also generally when employing this technology, several obstacles have to be overcome before a commercially viable laminar flow aircraft can be developed and produced. Apart from weather and climatic conditions in which an aircraft operates, these obstacles relate to environmental and manufacturing aspects and include the following:

- Aerodynamic surface contamination by insects
- Manufacturing quality, with special reference to manufacturing roughness
- Atmospheric particulates
- Atmospheric turbulence, noise, and vibration.

3.1 Surface contamination by insects

One of the critical items for laminar flow technology—for the NLFC as well as for the HLFC concept—is contamination of leading edges by insects. The strength of contamination shows broad variations. A strong gradient of insect density caused by altitude is generally observed. Croome and Holmes [80] reported a curve-fit diagram of their measured data:

$$\text{Insect density} = 1.4158 + 2402.95 * \text{Altitude}^{-0.901416}$$

with insect density as the number of insects per 10^6 ft^3 and the altitude in ft. This formula clearly shows that a high risk of insect strike is strongly limited to the ground-near region up to some hundred feet. During strong thermal convection the risk of insect contamination is increased. This fact is well-known to glider pilots, who use the thermal updrafts to climb to higher altitudes. But even in this case the higher insect density is restricted to the lower region of convection space, below 5000 ft.

Temperature and wind speed have a strong influence on the insect density. At temperatures below 10 to 15 °C the number of insects is drastically reduced. Wind speeds above 5 m/sec also cause a reduction of insect density. Ground moisture is generally important. In desert regions an insect problem is relatively low and in warm boggy areas the density is quite high.

Insect contamination reduces the benefits of laminar flow markedly, even at moderate Reynolds numbers. Figure 3.1-1 shows lift versus drag coefficient curves measured with a laminar flow glove on the DLR Dornier Do 228 test aircraft. The solid line indicates the clean glove and the dashed line the fully turbulent glove simulated by tripped transition at 5 percent of chord on both surfaces. The measurements performed with the contaminated glove for four different flights have a relatively small scatter. They clearly show that the laminar flow benefits are nearly fully lost and that an anticontamination system is indispensable for achieving the full benefits of laminar flow.

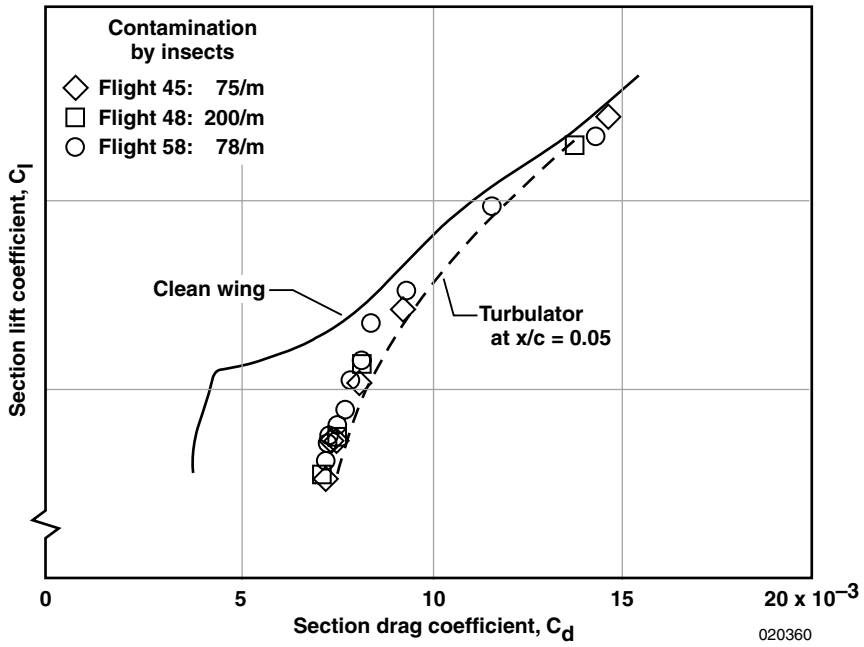

Figure 3.1-1. Influence of insect contamination on wing section drag coefficient for a laminar flow glove on the DLR Do228.

3.2 Manufacturing roughness

Laminar flow is much more sensitive to any kind of disturbance than turbulent flow. This means that new requirements for wing surface quality must be established. Wind tunnel and flight experiments show that, because of the impact of disturbances on the laminar boundary layer, three different situations must be identified. For very low disturbance heights, up to a so-called "critical height," (1) the disturbances do not influence the development of the boundary layer. For disturbance heights above this critical value, (2) the extent of the laminar boundary layer is reduced more and more as disturbance height increases until (3) transition (called "bypass transition") finally occurs at the disturbance itself. Consequently the following three questions arise:

1. What is the critical disturbance height up to which no impact on the laminar boundary layer occurs?
2. What is the disturbance height which induces transition at the location of the disturbance?
3. How can the distance be described between the locations of disturbance and transition?

For manufacturing issues in particular, the first question is of interest. For the critical disturbance height of circular wires crosswise to flow direction Goldstein [81] offers the relation

$$(u_k^* \times k_{crit})/\upsilon = 7$$

with the shear stress velocity $u_k^* = (\tau_{0k}/\rho)^{1/2}$ and τ_{0k} as the wall shear stress at the disturbance location. Assuming accelerated or constant speed flow, this relation can be converted to

$$\mathrm{Re}_{k,\,crit} = (\mathrm{U_k} \times k_{crit})/\upsilon = 50,$$

where $\mathrm{U_k}$ denotes the velocity within the boundary layer at the disturbance height. Following Goldstein, for values of Re_k below 50, circular wire disturbances will not affect the laminar boundary layer. Fage and Preston [82] determined that for circular wires, values of Re_k above 400 will always force bypass transition. For the case of reduced extent of laminar flow at Re_k above 50 and below 400, no publications are known.

Unfortunately, the critical values of Re_k strongly depend on the type and shape of disturbance. The boundary layer reacts more strongly to sharp-edged and three-dimensional disturbances.

Of special interest is the influence of typical technical roughness elements, such as two-dimensional forward and backward steps, streamwise and transverse gaps, as well as three-dimensional circular disturbances (like a head of a rivet or a screw).

Some flight investigations with these different types of disturbances have been performed on the VFW 614/ATTAS glove [40] and on the Dornier Do 228 glove [49]. All the different disturbance configurations tested have a common behavior, shown in Figure 3.2-1 with reference to the influence of a forward and backward step on transition location. In cases with a large extent of laminar flow, the laminar flow is most sensitive to the disturbances when they are located in the region between 5 and 20 percent of chord length. In this range the largest reduction in laminar flow extent is observed. A possible explanation is that for the first 5 percent of chord length, the boundary layer is stable and the created disturbances are damped, whereas downstream of 20 percent, the boundary layer thickness is large compared with the disturbance height so the disturbances have no effect.

The strong influence of the type of disturbance and the impact on the laminar boundary layer is shown in Figures 3.2-2 to 3.2-4. All cases are associated with the same flight condition and with the same representative disturbance height, unit h being about 0.06 mm. Forward-facing steps of 1h and 2h have no effect on the extent of laminar flow, as shown in Figure 3.2-2. A step with the height of 3h has also no effect on the boundary layer development if it is located downstream of 12 percent of chord length, but between 5 percent and 12 percent a strong reduction of laminar flow extent with a maximum at 8 percent can be observed.

For the rearward-facing step in figure 3.2-3, only a disturbance height of 1h has no effect on the laminar boundary layer. For the rivet-head type disturbance simulation in figure 3.2-4, all three disturbance heights have a strong impact on the extent of the laminar boundary layer. These four examples of disturbance effect measurements clearly show that the above relations for calculation of allowable disturbance heights can only serve as a very rough guideline.

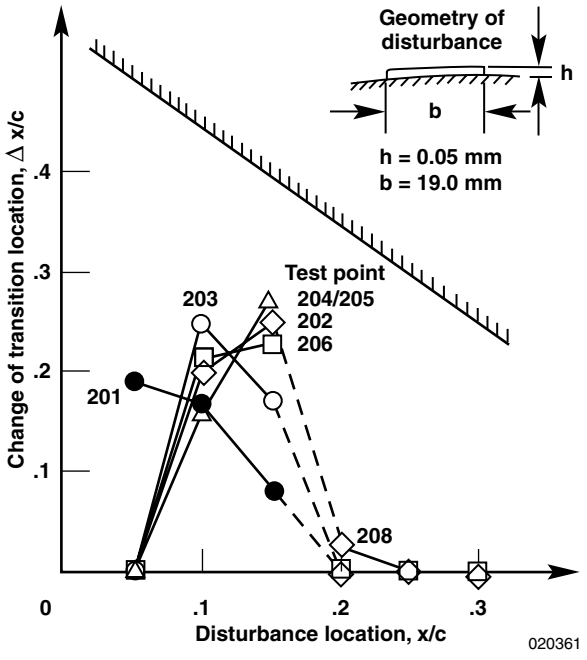

Figure 3.2-1. Reduced extent of laminar flow by means of a tape disturbance depending on the disturbance location, measured at the VFW614/ATTAS glove.

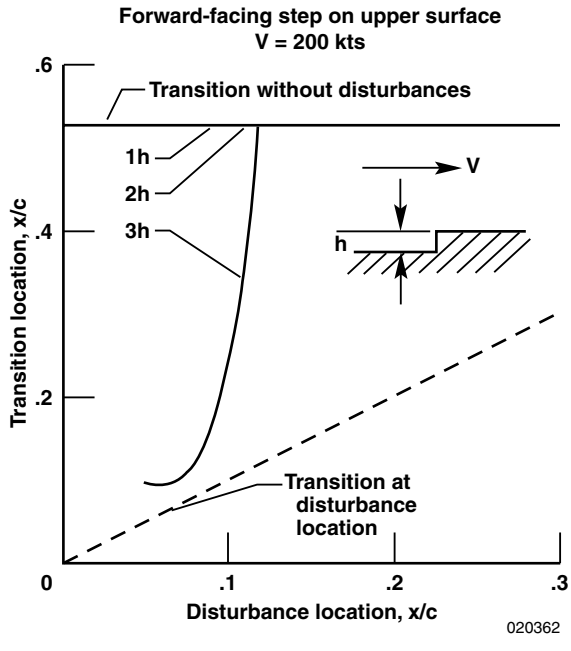

Figure 3.2-2. Reduced extent of laminar flow induced by a forward-facing step on the Dornier Do 228 laminar flow glove.

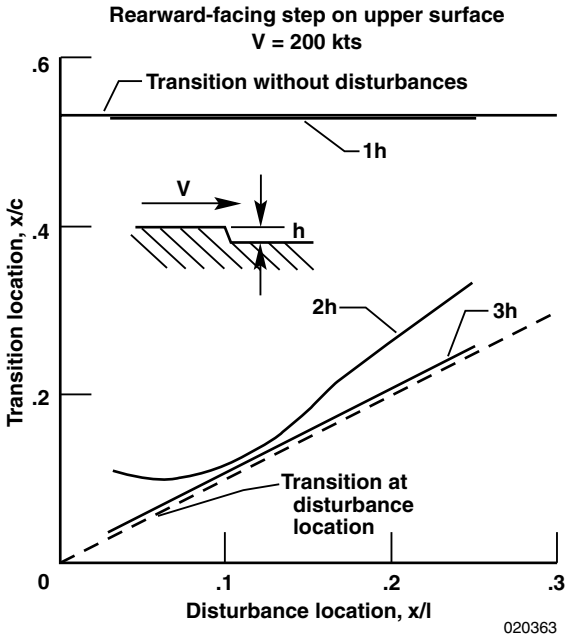

Figure 3.2-3. Reduced extent of laminar flow induced by a rearward-facing step at the Dornier Do 228 laminar flow glove.

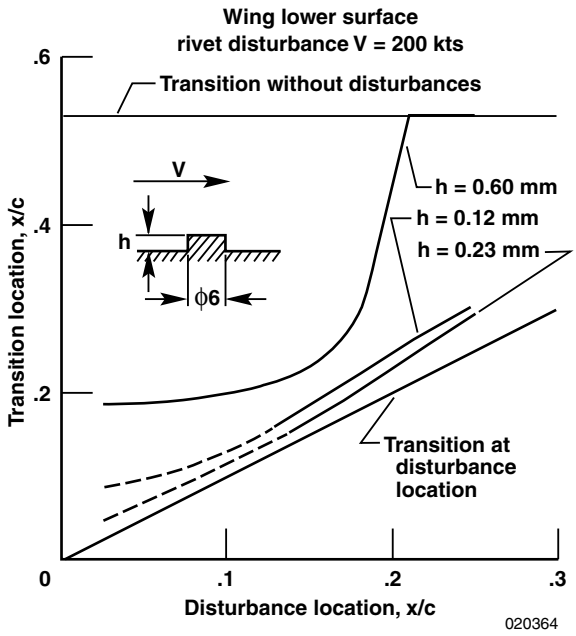

Figure 3.2-4. Reduced extent of laminar flow induced by a rivet type of disturbance at the Dornier Do 228 laminar flow glove.

3.3 Atmospheric particulates

R. E. Davis, NASA Langley Research Center, Hampton, VA

3.3.1 Mechanism for laminar flow loss in particulate concentrations

Atmospheric particulates can cause loss of laminar flow on an aircraft laminar flow surface. G.R. Hall of Northrop aircraft developed a theory [83] to explain the loss of LF during cloud encounters with the X-21A. This theory predicted the size, shape, and concentrations of cloud particles that would trip laminar flow on the X-21A airfoil. The mechanism of laminar flow loss is that the wakes from individual cloud or haze particles that penetrate into an initially laminar boundary layer can initiate local turbulent spots in the layer. If the cloud-haze particles are large enough, are of the right shape, and are present in sufficient concentration, they can “trip” the flow in the boundary layer, causing it to transition; the effect is slight in thin haze, and grows markedly as concentration increases. Airfoil shape has an effect, in that thicker airfoils deflect smaller-sized particles more readily. Hall concluded that, for the X-21A, airfoil particles larger than 32 μm would cause problems at an altitude of 40,000 ft, and particles larger than 17 μm would cause problems at a 25,000 ft altitude. Pfenninger [84] suggested that wing sweep may also be a key factor in LF loss, because wing sweep leads to spanwise flow, increased turbulence production, and increased time of particle residence in the boundary layer. Indeed, LF loss had not been mentioned in LF investigations preceding that with the X-21A. Therefore, LF loss problems are expected to be more severe for swept-winged aircraft.

3.3.2 Impact of cloud encounters on LFC aircraft feasibility

In view of demonstrated impact from clouds on LF during the X-21A program, meteorological studies were carried out by the USAF [85] to assess the likely impact of cloud encounters on the feasibility of flying LFC-configured C-5-type transports on long-range transport routes. These studies indicated that clouds would be encountered around 6 percent of the time at cruise altitudes on international military transport aircraft routes, and that simple altitude changes could normally be used to restore LF. This result suggested that, while LF is degraded during cloud encounters, the probability of cloud encounters is not so high as to make

LF-configured aircraft impractical for everyday use. Additional studies, supported by the NASA Aircraft Energy Efficiency Program (ACEE), were carried out using data from atmospheric particle-sampling probes flown in the NASA Lewis Research Center Global Atmospheric Sampling Program (GASP) [86, 87]. These studies derived cloud-particle encounter data for several long-range commercial airline routes worldwide over a range of altitudes; the results show that cloud-encounter probability varied with altitude, geographic location, and season. However, the overall result indicated that clouds or haze should be encountered around 6 percent of the time, on average, and that LF could be restored through altitude changes. Thus, the results from the GASP particle sampler study are consistent with the meteorologically-derived results in the earlier USAF study.

3.4 Turbulence, noise, and vibration

In Sections 4.3, 4.4 and 4.5 discussion shows the influence of turbulence, noise, and vibration on the development of the transition process of the laminar boundary layer to be quite weak or rarely observed in flight.

With respect to the influence of noise for those flight tests with laminar flow gloves on LFU 205, VFW614/ATTAS, Dornier Do 228 and Fokker F100, investigations with one engine shut down have been performed. Except in one case with the VFW614/ATTAS, no influence of noise on the extent of laminar flow has been observed, see Horstmann [40].

In case of the VFW614/ATTAS test, it was known from ground tests that at a power setting of 90 percent the engine fan noise has a very high intensity peak at a frequency of 6 kHz, which is inside the Tollmien-Schlichting frequency range expected. Figure 3.4-1 shows a downstream movement of the transition line of about 10 percent when the fan speed is reduced from 92 percent to 50 percent.

During strong turbulence of medium scale, an influence on the extent of laminar flow is also visible but the reason is the deformation of the pressure distribution by gusts. The effect of small-scale turbulence in flight tests as a receptivity problem of the laminar boundary layer has not yet been reported. In the glider pilot scene, small-scale turbulence effects on the glider performance are under discussion.

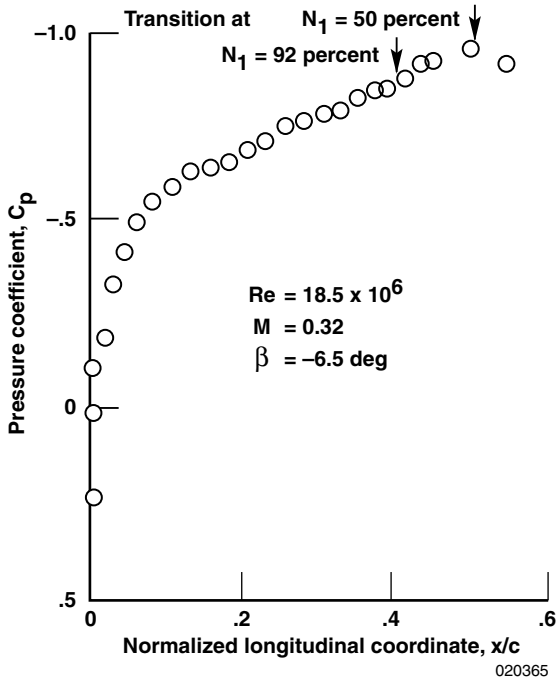

Figure 3.4-1. Reduced extent of laminar flow on the VFW614/ATTAS laminar flow glove as a result of fan-speed induced noise.

This page has been deliberately left blank

Page intentionnellement blanche

4.0 Measurement techniques

This chapter describes many of the techniques used in laminar flow flight tests. Special care and attention is needed so as to not cause the boundary layer to transition from laminar to turbulent flow because of the instrumentation. Requirements for good pressure measurements for laminar flow are given in Section 4.1 “Pressure Measurements.” Section 4.2 “Boundary Layer Measurements,” describes the many ways to determine the location of boundary layer transition. No one method can be used in all circumstances. Each method has its own application. Some, like the infrared image technique, can give global results, whereas others, such as the traversing pitot technique, can identify the beginning and end of boundary layer transition. Many techniques can only indicate if transition has occurred. Finally, measurement techniques are described for acoustics, vibration, atmospheric turbulence, and atmospheric particulates, each of which can also effect the boundary layer transition process.

4.1 Pressure measurements

An excellent source of information on nearly all aspects of in-flight pressure measurements is ADARDograph No. 160 of the AGARD Flight Test Instrumentation Series, Volume 11, on Pressure and Flow Measurement [88]. In this chapter only specific items will be discussed, namely those that are related to surface and wake pressure measurements by means of multipressure transducers for the determination of local characteristics of laminar flow sections of wing or tail planes.

Measurement of surface or wake pressures in flight tests are generally performed by means of differential pressure transducers. These instruments allow a smaller scale-range than absolute transducers and are thus more accurate. In flight tests, even at stationary conditions it cannot be assumed that the climb or sink rate is zero. Consequently, the transfer functions of the pressure tubes on both sides of the transducer have to be known in order to correct the measured pressures. For steady conditions with usual sink or climb rates the transfer function measurements can be avoided by means of a simple test setup, shown in figure 4.1-1. The reference port (static port of the aircraft) and the measurement port (e.g. a pressure orifice) are connected by tubes of equal length and equal diameter (providing equal time-delay) to a pressure-test system that provides a constant rate of pressure variation, here symbolized by a combination of altimeter, variometer, and a pressure regulator. Applying different constant pressure rates to the aircraft system that correspond to typical climb or sink rates, the pressure transducer should not show any reaction. In order to achieve this, all pressure tubes on the measurement side of the pressure transducer must have the same diameter and length. The tube on the reference side should have a smaller time delay than the tubes on the measurement side and needs to be equipped with an adjustable flow resistance that must be adapted to minimize the transducer reaction.

Another concern is the disturbance of laminar flow induced by the pressure orifices. Experience from different flight tests show that the hole-diameter of the orifices should not be larger than 0.3 mm. For unswept wings with small pressure variations in a spanwise direction, the orifices can be staggered about 15 degrees to the flow direction, as shown in figure 4.1-2. Thus any flow disturbances emanating from one hole do not pass over those of another hole and the disturbances cannot combine and lead to transition. In any case, the pressure lines must be sealed completely.

Wake measurements for a laminar flow wing using a wake rake in order to determine the drag of a wing section are often strongly influenced by local disturbances of the laminar boundary layer e.g. dust particles, insects, or unsealed pressure orifices. In order to avoid false measurements or additional test flights, it is very useful to install a movable wake rake (e.g. as shown for an A320 aircraft in figure 4.1-3) at the rudder of the fin. Combined with transition visualization by means of an infrared camera, wake measurements become much more reliable and representative.

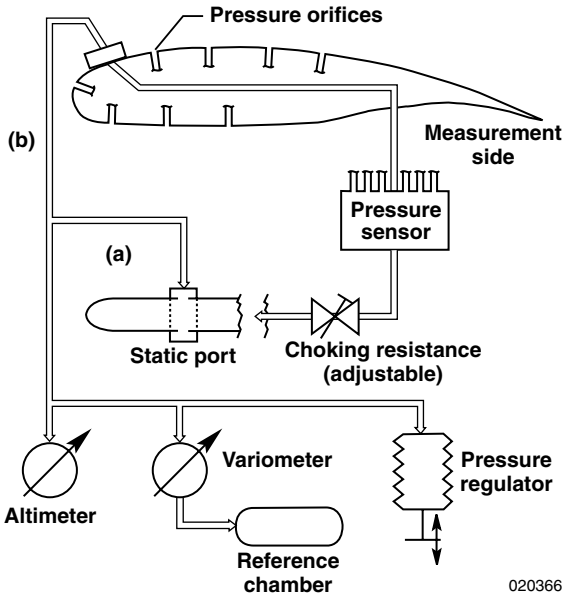

Figure 4.1-1. Simple arrangement for compensation of time delay of the pressure tubes on both sides of a differential pressure transducer.

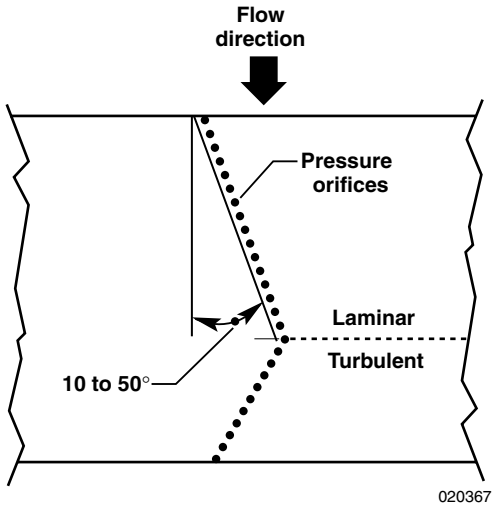

Figure 4.1-2. Arrangement of pressure orifices for laminar flow measurements with minimum interference of orifices at an unswept wing.

Figure 4.1-3. Vertically movable wake rake at the rudder of the A320 fin.

4.2 Boundary layer measurements

4.2.1 INFRARED IMAGE TECHNIQUE

4.2.1.1 Introduction

Transition from laminar to turbulent flow is frequently detected by the well-known oil-flow method or by sublimation techniques using acenaphthene. Both methods have the disadvantage that the flow may be affected by the visualization material itself. Furthermore, both are difficult to apply and to control in flight tests. Other methods like subsurface microphones, hot-wires, or hot-films can give only rough point-by-point information on whether the boundary layer is laminar or turbulent. The transition line must finally be estimated manually or automatically by means of the point information. Furthermore, all three techniques produce additional surface roughness and need time-consuming and expensive preparation and installation.

Use of the infrared image technique avoids these disadvantages [89]. It is a fast and inexpensive (after the purchase of the hardware) technique that gives the full, detailed information of the location of the transition line. In the following chapters application of the infrared image technique for transition detection is described. The basic physical principles as well as the system itself and examples of application are discussed.

4.2.1.2 Skin friction and heat transfer

According to the Reynolds analogy the heat transfer coefficient α_h depends in a simplified form on the following parameters [75]:

$$\alpha_h = \frac{1}{2} c_f' \frac{U\lambda}{\nu}$$

where c_f' is the skin friction coefficient, U the local velocity, λ the heat conductivity of the fluid and ν the kinematic viscosity. Note that λ, as far as aircraft are concerned, does not change with pressure. The formula explains the well-known fact that heat transfer in a laminar boundary layer is small because skin friction is small and that heat transfer in a turbulent boundary layer is much increased as a result of increased skin friction.

Figure 4.2.1-1 shows the skin friction coefficient of a flat plate as a function of the local Reynolds number Re_x for three different transition Reynolds numbers, Re_{xTr}. On smooth surfaces the transition Reynolds number depends on the flow quality; Re_{xTr} is of the order of 5×10^6 at free-flight conditions. Neglecting a certain transitional range, we note that at the transition point skin friction jumps by more than a factor of 10. According to the Reynolds analogy, the heat transfer also changes by the same factor.

If there is a temperature difference between the fluid and the aerodynamic surface, the surface will adopt different temperatures, depending on whether the boundary layer is laminar or turbulent. Thus, in turbulent flow, and especially just behind the transition, the heat transfer is high and the surface will adopt nearly the temperature of the fluid. On the other hand, the surface temperature will remain nearly unchanged in the laminar boundary layer just upstream of the transition location, where the wall shear stress is minimum.

It should be noted that the Reynolds analogy is only valid for fully established laminar or turbulent boundary layers. It is not valid in transitional or separated flow.

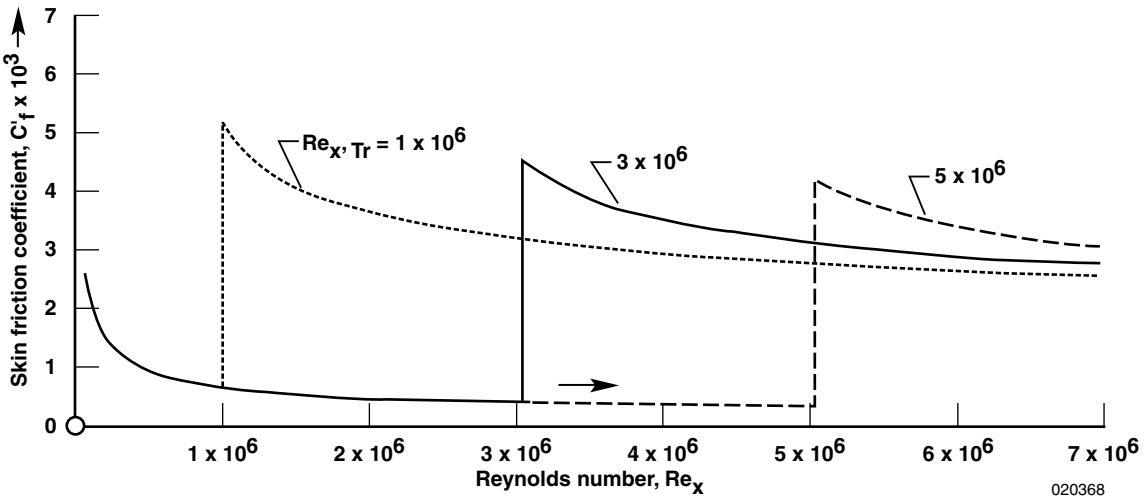

Figure 4.2.1-1. Skin friction coefficient of a flat plate as a function of the local Reynolds number Re_x for three different transition Reynolds numbers Re_{xTr}.

4.2.1.3 Infrared image system

Modern nitrogen-cooled infrared scanner systems are able to resolve radiation temperature differences down to 0.1 °C. Good images are obtained with temperature differences of 1 °C and excellent images with 2 °C differences. As shown in fig. 4.2.1-1, the skin friction changes with transition by approximately a factor of ten. Therefore, on an infrared image, the transition line is marked by a sharp step in the surface temperature that becomes visible on the screen in a change from dark to white, or vice versa.

A representation of the infrared information by a color step image for the detection of the transition location (instead of grey steps as in all figures of this paper) did not provide any advantage. For the purpose of transition detection the color step image is somewhat confusing. However, for shear stress information, it may be useful.

4.2.1.4 The origin of temperature differences

Observations showed that in many wind tunnels, the temperature differences necessary for the infrared picture are present without any internal or external heating of the model surface. This is normally a result of the radiation exchange between the model and the walls of the closed-test section or the walls of the measuring hall, in case of an open-test section. In other cases the temperature differences for a good picture were obtained by switching wind tunnel cooling on and off. This method is only effective if the model surface and the test section surface do not have the same heat capacity (better temperature propagation coefficient). This, for example, is the case if the model surface is of plastic material and the wind tunnel wall of metal.

For free-flight tests radiation into space or sun radiation is used. External heating by radiators is not recommended because of possible reflections into the infrared system. Nevertheless, the most comfortable arrangement is that of an internally heated surface. This can be realized by a graphite-covered glass fabric as used for mould heating. The analogy between measurements with hot films and with an infrared system is quite obvious.

With the exception of the sun radiation, the paint color of a test surface has no influence on the infrared image. Normally test surfaces were covered with sanded and polished white paint, like sailplanes. Markings of red or dark color are not visible on the infrared image. Thus markings were done with heat-conducting silver paint, which naturally have the same temperature as the model surface at their location. But bright

metallic surfaces have a considerably lower radiation coefficient, resulting in less radiation, which the infrared system interprets as a lower temperature.

Radiation properties of different materials with respect to the radiation incidence angle are provided in figure 4.2.1-2 Non-metallic materials (fig. 4.2.1-2(a)) have a wide range of incidence angles where the radiation is nearly constant. On the other hand, metals (fig. 4.2.1-2(b)) retain an astonishingly high level of radiation with decreasing incidence angle. Problems may arise with incidence angles below 20 degrees.

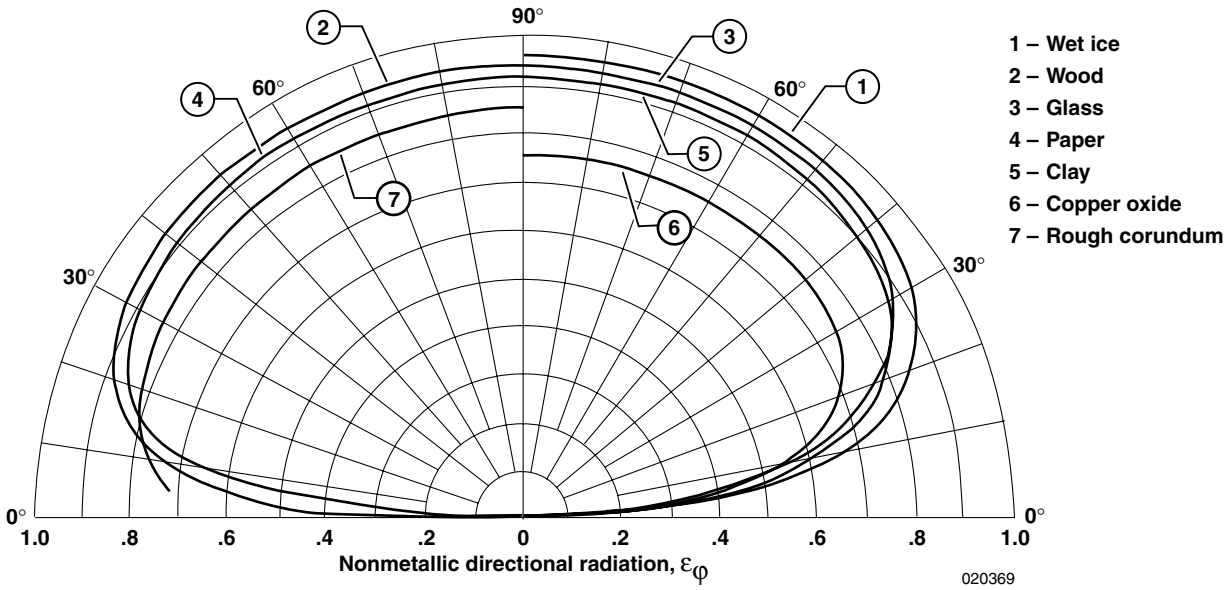

(a) Nonmetallic.

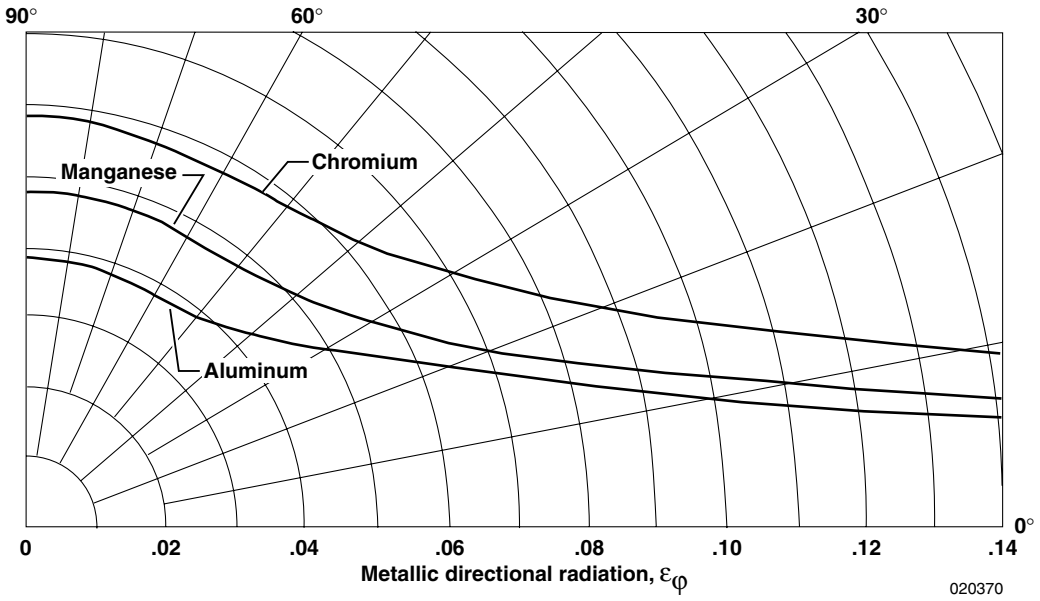

(b) Metallic.

Figure 4.2.1-2. Directional radiation properties of nonmetallic and metallic surfaces.

4.2.1.5 Examples of transition detection by infrared technique

Figure 4.2.1-3 shows an infrared image of an airfoil upper surface, the model being colder than the air. Airflow is from left to right, as in all other figures of this paper. The grey color is darkening from the leading edge to about 70 percent of the chord length, corresponding to a decreasing skin friction of the laminar flow with increasing airfoil chord. Since the model is colder than air, pure white color correlates with high temperatures and high skin friction, whereas the dark color indicates low temperatures and low friction. Downstream of the transition line the skin friction of the fresh turbulent boundary layer is very high, resulting in a white color. Going further downstream of the transition, the friction of the turbulent boundary layer diminishes, resulting in a certain darkening. At the bottom of figure 4.2.1-3 the well-known turbulent wedges originating from aluminium strips are visible. These wedges are characteristic of a laminar boundary layer and do not occur in a turbulent flow. Note that the color in the wedge downstream of the transition location is grey, in contrast to the part of the model without wedges at the same chordwise position. This indicates lower skin friction because of a thicker turbulent boundary layer downstream of the wedges compared to the skin friction in undisturbed flow.

On the upper part of figure 4.2.1-3 a small forward shift of the transition location is visible. This is the result of a line of pressure holes located one behind another. This is a revealing demonstration of subcritical disturbances in a laminar boundary layer that do not result in a turbulent wedge. Nevertheless, the pressure holes do influence the laminar boundary in such a way that the transition point moves upstream.

Figure 4.2.1-4 shows an oil-flow picture and an infrared image of the same wing at identical flow conditions. The aluminium strip was removed for the oil-flow picture. Note that the lens system of the infrared camera apparently distorts the picture in a barrel-like way. The oil-flow picture indicates a laminar separation bubble beginning at $x/c = 0.58$ and a transition location at $x/c = 0.65$. For the transition location, the same value can be derived from the infrared image. The separation line is only barely visible in the infrared image. In this case, the oil has no detectable influence on the development of the laminar boundary layer and on the transition location. A forward-shift of the transition location by the row of pressure holes cannot be detected in the oil flow picture because of the contamination of the orifices by the oil.

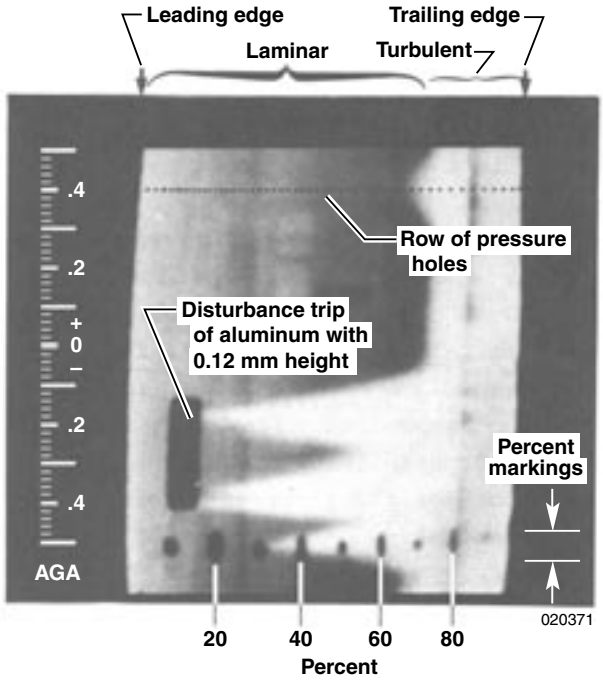

Figure 4.2.1-3. Characteristics of an infrared image.

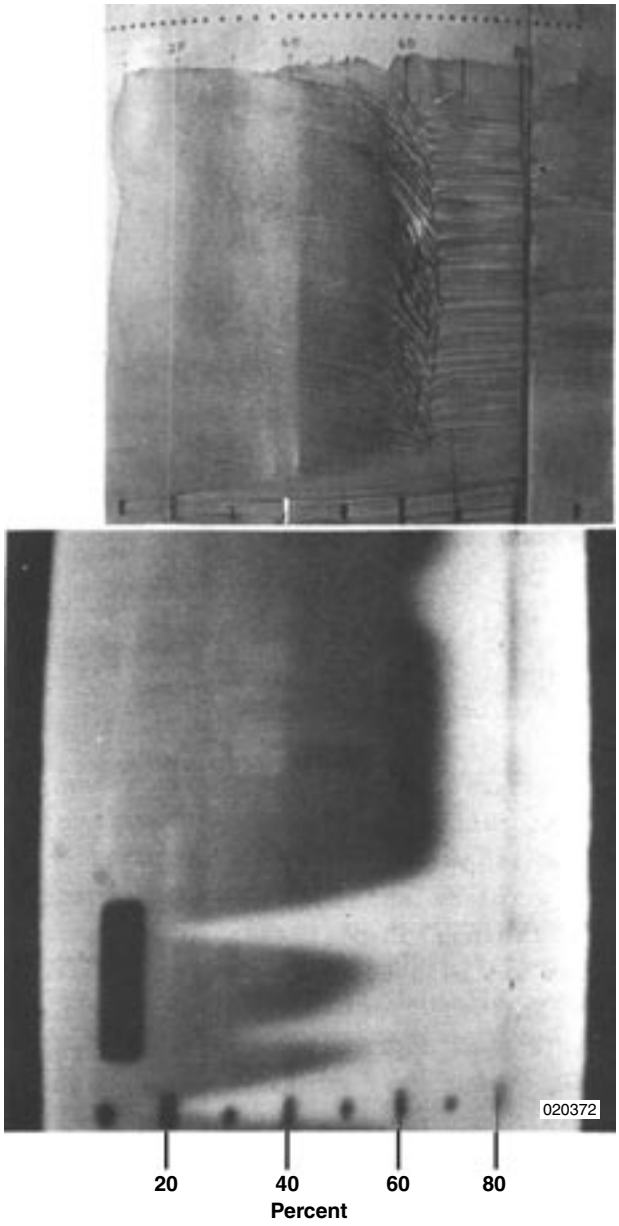

Figure 4.2.1-4. Comparison of an oil-flow picture and an infrared image of the same wing at identical flow conditions.

An infrared image of a wing taken in-flight from the cabin of the small LFU 205 4-seater airplane is shown in figure 4.2.1-5. The wing of the airplane was equipped with a glove for laminar flow investigations [39]. The glove was painted red in order to enhance the influence of sun radiation and to enable the application of the acenaphthene technique. Transition is clearly visible, in this case in the inverted mode.

One of the earliest experiments with transition detection by infrared images showing all types of transition was the ATTAS NLF experiment of DLR in Braunschweig [40]. The DLR VFW 614/ATTAS research aircraft, shown in figure 4.2.1-6, is a 40-seat jet aircraft with a wing having a leading-edge sweep angle of 18 degrees. For these tests a maximum Mach number of $M = 0.7$ and a maximum Reynolds number based on wing chord at the glove center section of $Re = 30 \times 10^6$ could be flown. The landing flap can be operated with reduced flap deflections up to high Mach numbers. Depending on the speed, the yaw angle can be changed between $\beta = \pm 3°$ and $\beta = \pm 5°$, thus leading to a sweep-angle variation of $\varphi = 13°$ to 23°.

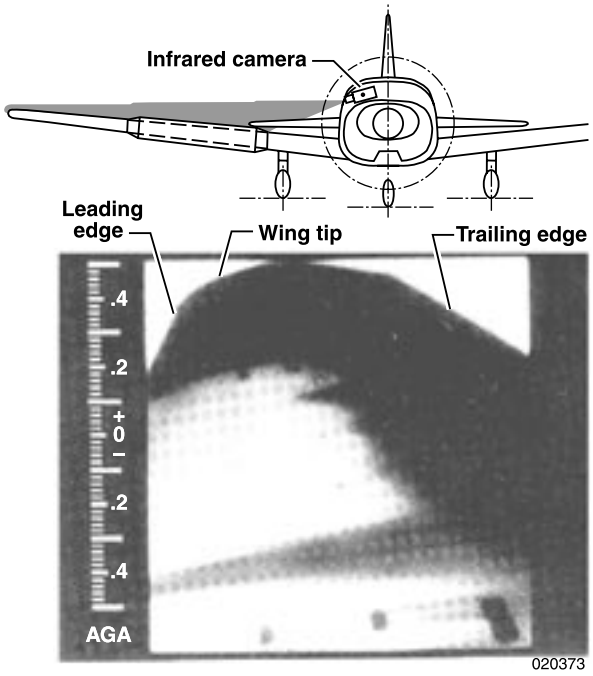

Figure 4.2.1-5. Infrared image of the LFU 205 glove in free flight, inverted image; laminar boundary layer white, turbulent dark.

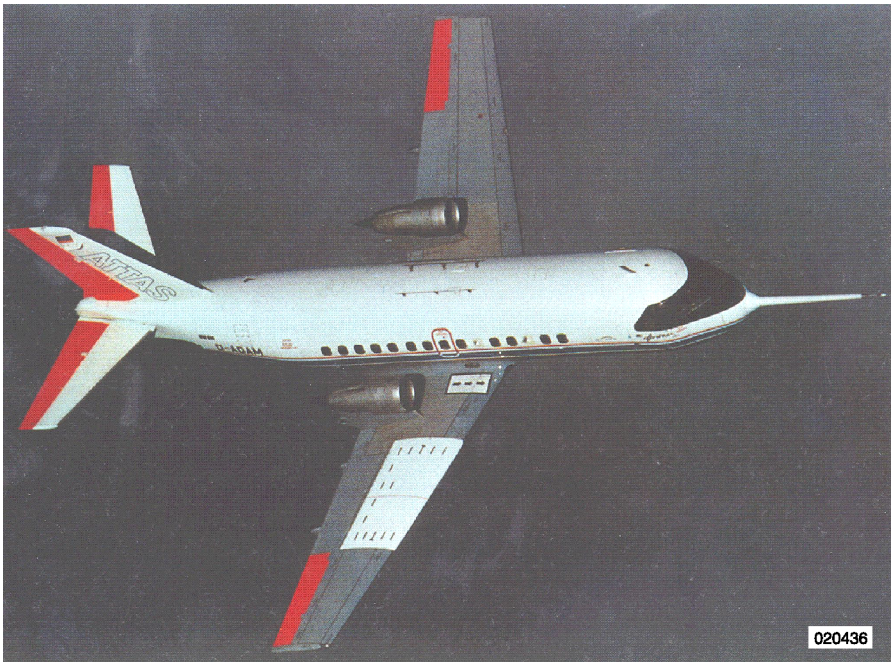

Figure 4.2.1-6. DLR test aircraft VFW614/ATTAS with a glove for natural laminar flow (NLF).

The experimental sensor installation can be seen in figure 4.2.1-7. In three sections, 180 pressure taps are distributed with a hole diameter of 0.3 mm and a minimum spacing of 0.3 percent of chord length at the leading edge of the center section. The pressure measurement system is controlled by the ATTAS experimental system which is specially developed for flight mechanics purposes. In order to allow measurements at climb or descent conditions, the pressure measurement system is dynamically calibrated.

The hot-film system is also connected to the basic experimental system. Two hot-films at the stagnation line allow one to distinguish between attachment line transition and crossflow-induced transition close to the leading edge. The hot-films located downstream provide information about the extent of the transition range and about the frequency range of Tollmien-Schlichting waves.

The infrared camera was installed behind a window specially equipped with quartz glass. A typical infrared image showing TS-governed transition is presented in figure 4.2.1-8. A typical development of the transition line on the glove for different pressure distributions generated by flap deflection is shown in fig. 4.2.1-9. The sketch is composed from three different infrared images taken at the flap deflections of 10°, 5° and 1°. Apart from the four turbulent wedges, induced by upstream disturbances, the transition line is nearly straight at constant chord. This behavior is typical for a transition process governed by Tollmien-Schlichting instability.

At many data points, it was possible to obtain a TSI- and a CFI-governed transition at the same pressure distribution but at different yaw angles. A typical example is shown in fig. 4.2.1-10. At 3° and 0° yaw angle the transition lines coincide. At $\beta = -3°$ the transition line moves rapidly upstream and becomes saw-toothed. This characteristic behavior could be observed at all CF data points and it is well-known from many wind tunnel investigations dealing with laminar-turbulent transition by crossflow vortices. This transition behavior supports the assumption that for this type of airfoil, only a weak interaction of Tollmien-Schlichting waves and crossflow vortices exists.

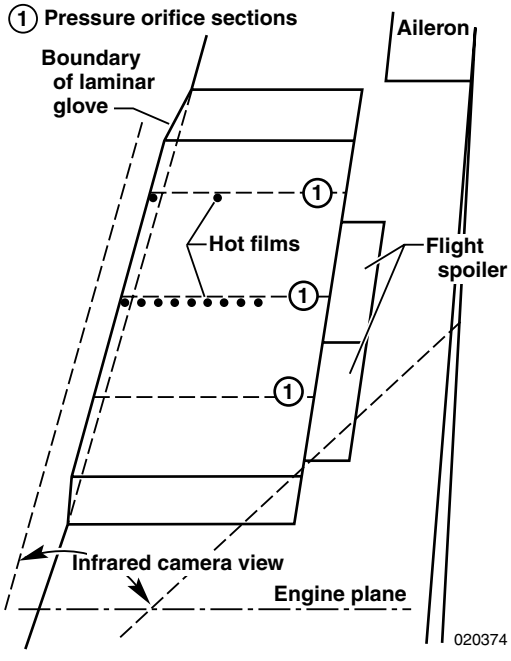

Figure 4.2.1-7. Geometry of glove of the VFW614/ATTAS and instrumentation.

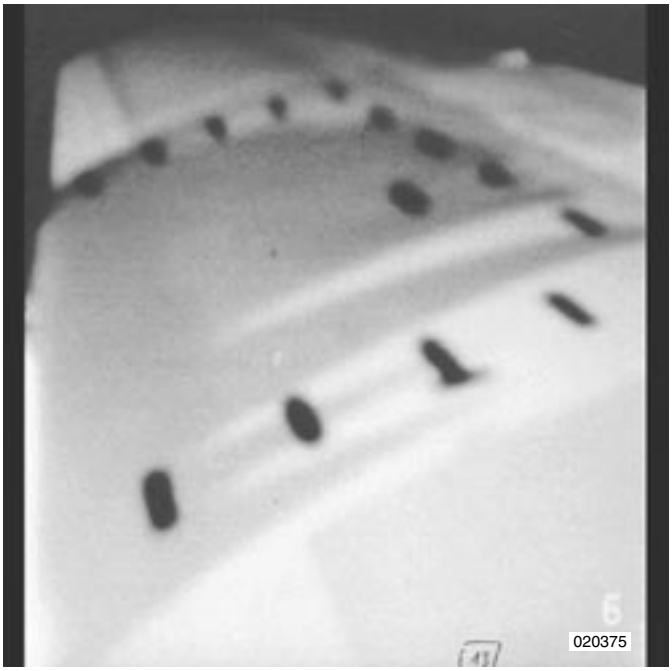

Figure 4.2.1-8. Infrared image of the ATTAS glove taken through a quartz glass window.

At indicated airspeeds above 300 kts, it was possible to achieve attachment line transition. Initiated by a 2-mm-thick wire, the turbulent flow spread outboard towards the tip. This phenomenon could be observed by the infrared image technique as well as by hot-film measurements. With increasing yaw angle, the transition line sweeps further upstream and an increasing part of the glove outboard of the wire disturbance remains completely turbulent, as shown in fig. 4.2.1-11.

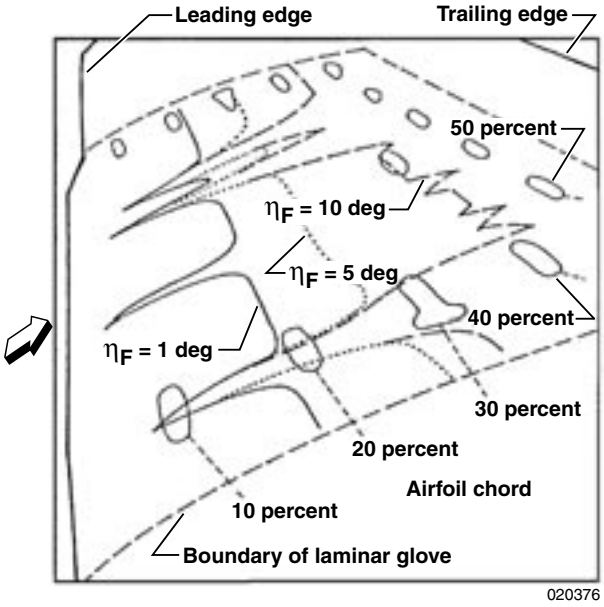

Figure 4.2.1-9. Drawing of transition lines on the VFW614/ATTAS glove for different flap deflections at flow conditions governed by Tollmien-Schlichting instability.

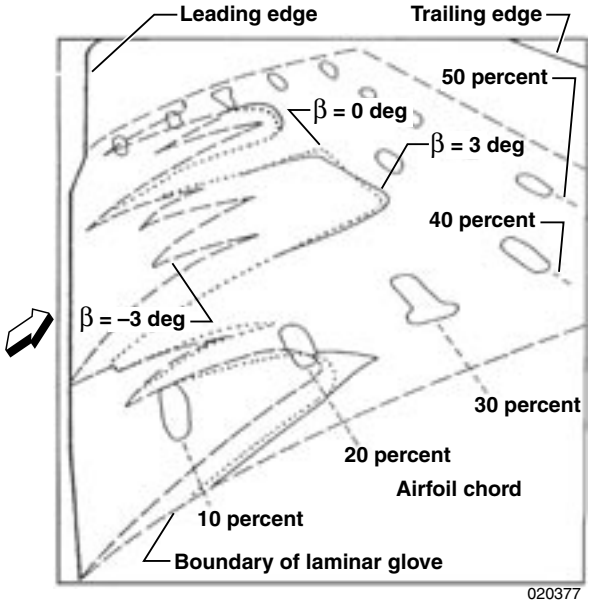

Figure 4.2.1-10. Drawing of transition lines on the VFW614/ATTAS glove for different yaw angles at flow conditions governed by crossflow instability.

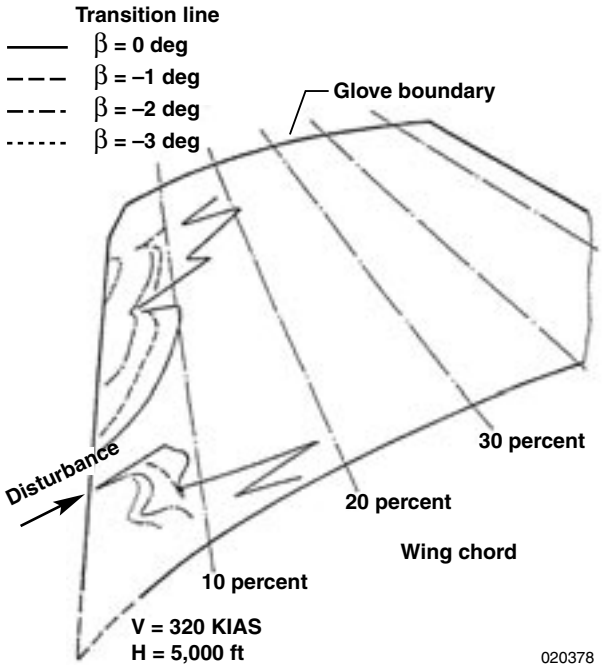

Figure 4.2.1-11. Drawing of transition lines on the VFW614/ATTAS glove for different yaw angles at flow conditions governed by attachment line transition.

4.2.1.6 Problems with infrared systems

If the model represents only a small area of the whole infrared image, the remaining contrast for the model areas is not sufficient for transition detection. This is a result of the automatic mean temperature adjustment of the infrared system. This problem can be solved by using various lens systems for the infrared camera with an adequate focal distance.

For flight tests the infrared cameras often can be installed within the fuselage. The cabin windows then have to be replaced by special IR transmissive windows made from germanium, silicium, or zinc selenide.

As mentioned above, the heat conductivity of the model surface leads to a certain temperature flattening. The order of magnitude of this effect depends on the surface material and the model size. Thus, in the case of tiny flow structures like crossflow-vortices the infrared technique may not show all details.

Metal surfaces should be covered by a plastic film of at least 0.3 mm thickness. The low radiation value of metal surfaces (see Section 3.2.1.4) is combined with a high reflection coefficient of the surface and a good heat transfer of the material. As a result, the weak heat radiation is mostly covered by strong reflecting radiation.

4.2.1.7 Conclusions

The infrared technique is a powerful tool for transition line detection. The whole test object area can be under surveillance for turbulent wedges or even smaller subcritical disturbances in the laminar boundary layer. This technique has been successfully applied in different wind tunnels and in free-flight experiments. In most cases “natural” temperature differences between the model and the fluid gave reasonable or good infrared images. In one case, switching the wind tunnel cooling system on and off gave good results. Nevertheless, the most comfortable approach is to use an internally heated model.

4.2.2 SURFACE TEMPERATURE MEASUREMENTS

4.2.2.1 Introduction

Surface temperature measurements on aerodynamic surfaces can be helpful in detecting the location of the transition front on such surfaces. These measurements are of particular value for those regions of interest that lie outside the field of view of infrared imaging systems, if infrared imaging systems are to be employed to obtain a global view of the location of the transition front. The detection of flow transition by surface temperature measurements utilizes, like the infrared thermograph technique, the physical flow property that different rates of heat transfer exist for the boundary layer flow over the target surface, depending on whether the boundary layer flow is laminar or turbulent. Correspondingly, different surface temperature levels are established in those two flow regions. In general a temperature difference exists between the surface and the edge of the boundary layer (freestream), so that with the heat transfer rate being lower in the laminar boundary layer than in the turbulent one, the surface temperature for the laminar layer surface adjusts itself to the free-stream temperature only gradually, in contrast to the turbulent boundary layer surface temperature in which the effect is rapid. If, for instance, the surface temperature is higher than that of the freestream, the surface of the laminar boundary layer region remains for a certain length of time at a higher temperature level than that of the region of turbulent layer flow over time. This feature is reflected in the observed temperature distribution, and the location of the change in the temperature level marks the location of the transition front.

4.2.2.2 Surface temperature sensors

Basically two types of temperature sensors, thermocouples and platinum resistance thermometers (PRTs), can be used to measure the temperature on aerodynamic surfaces of interest, such as wing, fin, and engine nacelle.

Thermocouples have found a widespread use in aerospace, ranging from turbine monitoring to space simulation testing for rockets and satellites. However, it appears that thermocouples have not yet been applied for transition detection on aerodynamic surfaces. The measurement accuracy of thermocouples depends on whether they are calibrated or not. For instance, for Type-T (copper/constantan) thermocouples of KAYE Instruments, Inc. Bedford, Massachusetts, USA, the KAYE V2835 (calibrated) thermocouple provides a NIST-traceable measured accuracy to 0.02 °C. In contrast, the K255 (not calibrated) thermocouple is 3/16 percent of the measured value. For a limited temperature range of –70 °C to +70 °C, this type of thermocouple would have at 70 °C, an error of 0.1875 percent, which corresponds to approximately 0.13 °C.

Platinum resistance thermometers have found a wide range of application. The most common type of PRT is the Pt 100 having a nominal resistance R_0 of 100 Ω at a temperature of 0 °C. The Pt 100 sensors are available in different tolerance classes based on the required accuracy of the temperature measurement. For class A the possible temperature error is $\Delta t = \pm(0.15 + 0.002|t|)$ °C, where t is the temperature measured in °C. The possible temperature error of class B is $\Delta t = \pm(0.30 + 0.005|t|)$ °C. Thus, for example, for $t = 70$ °C, class A yields a temperature error $\Delta t = \pm 0.29$ °C and class B yields a temperature error $\Delta t = \pm 0.65$ °C.

4.2.2.3 Application of platinum resistance thermometers

Past experience regarding the application of platinum resistance thermometers for the detection of the transition front location on aerodynamic surfaces has resulted in several lessons learned, which are of significance in guaranteeing meaningful surface temperature measurements:

- The surface of the measurement section should consist of a material of low thermal conductivity and low thermal capacity
- The sensors should be installed as close as possible to the surface to be tested
- The structure below the surface should have a sufficient thickness of homogenous material with low thermal conductivity.
- Surface temperature measurements on engine nacelles are in one respect more critical than on other aerodynamic surfaces, like wings and fins, in that the nacelle skin is prone to be affected by heat transfer from the engine.

Typical results were obtained during flight tests with the HLF nacelle on the DLR VFW614/ATTAS flight test aircraft conducted within the framework of a European collaborative program [68–70]. Details of the flight test vehicle are contained in reference [90]. Figure 4.2.2-1 depicts the VFW614/ATTAS in side and plan view and figure 4.2.2-2 shows a partial view of the flight test vehicle in flight with a NLF nacelle installed on the port engine, while the starboard engine has the standard production nacelle. Figure 4.2.2-3 illustrates a close-up view of the installed NLF nacelle.

Figure 4.2.2-4 shows the surface temperature distribution for the HLF nacelle fan cowl at radial $\varphi = 84°$ together with the infrared image of the outboard fan cowl for the condition of cruise with suction applied. Taking into account that the nacelle surface is slightly heated by the engine, the temperature distribution exhibits the expected trend, with a temperature level higher in the laminar flow region on the fan cowl than for the turbulent flow region. Temperature resolution is of such quality that the onset of transition $(x_{tr}/c = 0.55)$ and that of the fully turbulent flow $(x_{Tr}/c = 0.65)$ can be clearly identified. Noting that the carbon fiber composite (CFC) material of the fan cowl is a poor heat conductor, the transition length of $(x_{Tr}/c - x_{tr}/c = 0.10)$ can be expected to be a good approximation of the actual transition length. The location of the transition front, defined by the midpoint Tr_f between x_{tr}/c and x_{Tr}/c is at $x/c = 0.60$, which agrees well with the transition front position at $\varphi = 84°$ on the infrared image.

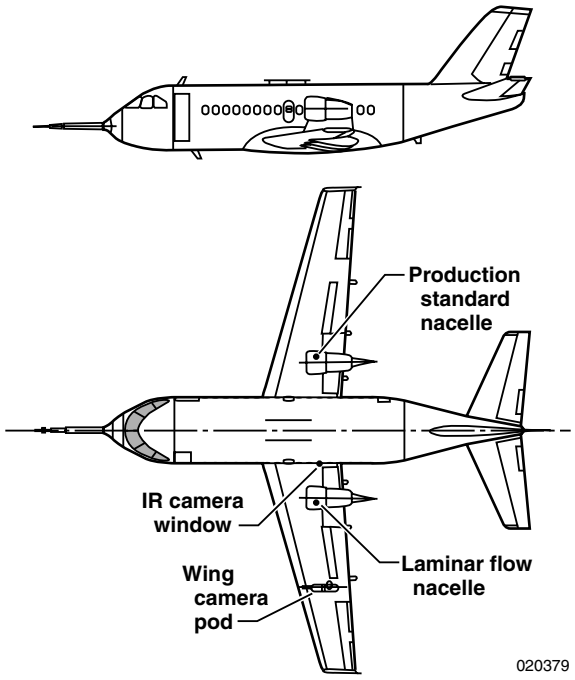

Figure 4.2.2-1. DLR test aircraft VFW614/ATTAS with laminar flow nacelle installed on the port engine.

Figure 4.2.2-2. VFW614/ATTAS in flight with NLF nacelle installed on the port engine.

Figure 4.2.2-3. Closeup view of the NLF nacelle on VFW614/ATTAS aircraft.

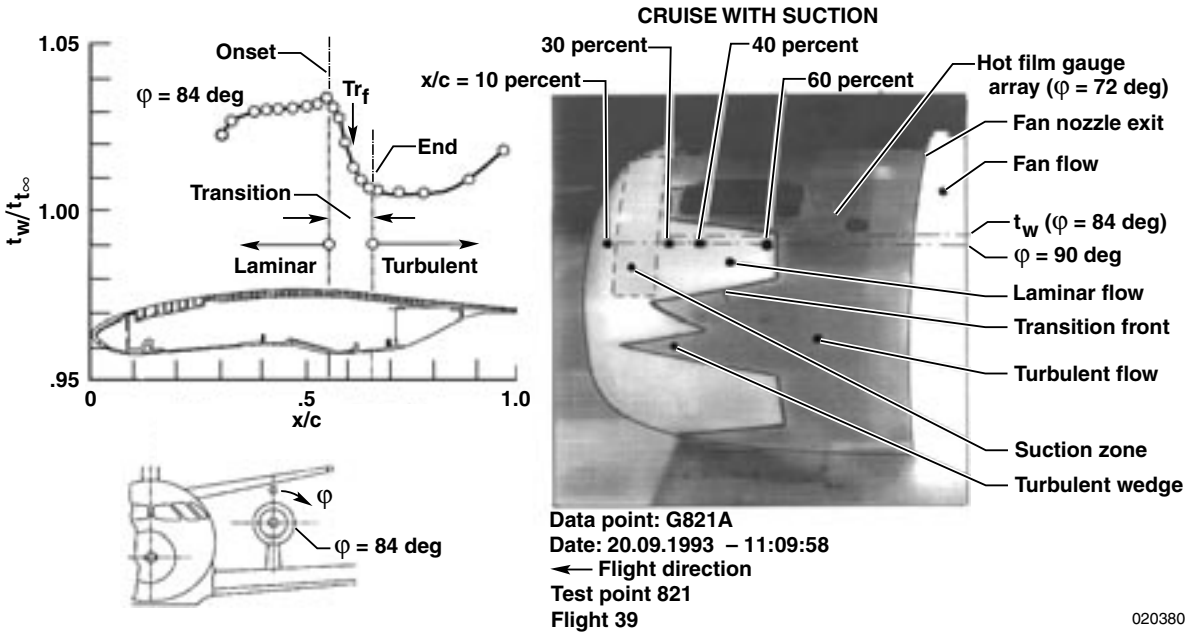

Figure 4.2.2-4. External surface temperature distribution and infrared image on the HLF nacelle of the VFW614/ATTAS aircraft.

4.2.3 HOT-WIRE/HOT-FILM ANEMOMETRY

Stan Miley, Old Dominion University, Norfolk, VA USA and Harry Chiles, NASA Dryden Flight Research Center, Edwards, CA USA

Hot-wire and hot-film anemometry use minute metallic heated elements (heat-flux sensors) to measure fluid flow (liquid or gas) velocity. The metal used for the sensing elements must have a high coefficient of resistivity, that is, the electrical resistance of the metal should have a relatively large, preferably linear, variation with temperature. Suitable metals for this are platinum and nickel. The metallic sensor is incorporated into a four-leg electrical bridge with the opposing adjacent legs set at a particular resistance ratio (commonly 5:1) as illustrated in figure 4.2.3-1. The resistance leg adjacent to the sensor is called the control resistance and is used to set the operating resistance (and accordingly the operating temperature) of the sensor to balance the bridge. As long as the sensor is below its set operating resistance, the bridge is unbalanced and an electrical voltage is generated across the bridge through a feedback amplifier, which causes an electrical current to pass through the sensor. The sensor is subsequently heated through the I^2R (resistance heating) effect and its temperature and electrical resistance increase accordingly. This process will continue until the resistance of the sensor is such as to balance the bridge and consequently null the bridge voltage. Through this feed-back process, any physical effect that removes heat from the sensor and lowers its temperature will result in an increase in the bridge voltage, producing the electrical current necessary to bring the sensor back to its set resistance (in practice, its set temperature). Consequently, the operating circuit is known as a constant temperature (resistance) anemometer. If the metallic sensor is immersed in a fluid flow that has a temperature below that of the sensor, then heat will be removed from the sensor in direct relation to the difference in temperature between the sensor and the flow; to the density of the flowing fluid; and to the velocity of the flowing fluid. A direct functional relationship then is created between the velocity of the flow and the bridge voltage created to force the sensor back to its set temperature, i.e., to electrically balance the bridge. Depending on the size of the metallic sensor and its physical mounting, the anemometer circuit can maintain the bridge voltage relationship to the flow velocity with flow fluctuations occurring at frequencies in excess of 50,000 Hz. Such high-frequency response requires care in the use of the connecting leads to the sensor and the balancing of the reactive elements in the circuit.

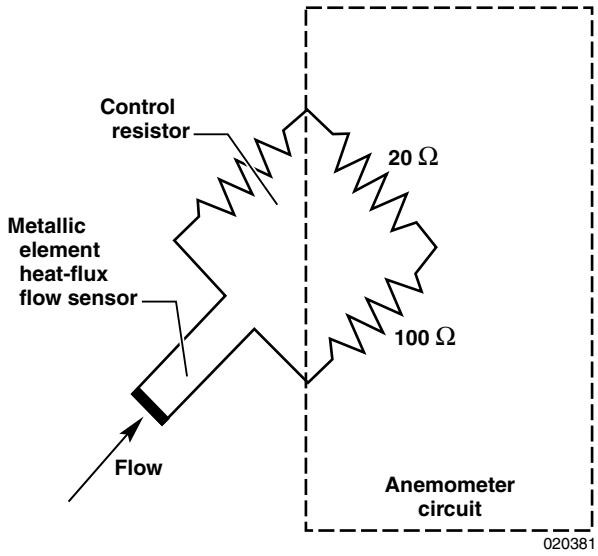

Figure 4.2.3-1. Four-leg hot-film and hot-wire anemometer electrical circuit.

Typically, a very high-gain amplifier is used to generate the applied bridge voltage from the unbalance signal created by the resistance change in the sensor. Amplifier gains in the order of 1,000 to 10,000 are common. This makes the hot-wire and hot-film anemometer electronic system extremely vulnerable to outside electronic noise. For in-flight applications, it is necessary to use good electronic shielding techniques for the cabling between the anemometer circuitry and the metallic sensors. Also, the electrical power to the anemometer circuit should be separate, if possible, from the aircraft system. Ideally, an isolated battery power source should be used. If the anemometers being used are any of the commercially available models that typically require alternating current 120 or 220 volt supply, then a clean sine-wave inverter should be installed to convert the direct current power from the battery. If in-house–constructed anemometer circuits such as those of Chiles [91, 92] are to be used, then care must be exercised in utilizing the direct current power supply of the aircraft. The problem here is the use of solid-state inverters or dc-dc converters, which use solid-state switching circuitry. When these devices are operating under high current load, large overshoots (voltage spikes) occur at the operating frequency of the device (commonly 400 Hz). Because of the high-frequency content, these spikes find their way into the anemometer signal. It is not uncommon to encounter a signal in the anemometer output composed of high harmonics of a 400-Hz frequency power system that is commonly used on military or commercial aircraft. If the test aircraft has such a power system, then care should be used to isolate the anemometer circuits from this source of anemometer output signal contamination.

4.2.3.1 Hot-film anemometry

The hot-film technique is an excellent method to determine the extent of laminar flow on an aircraft wing or similar surface using constant temperature anemometry for subsonic, transonic, and supersonic flight. The hot-films can be single, commercially available sensors laid out in a pattern on the surface to detect transition or they can be laid out on a thin polyamide sheet [93] if the surface does not have compound curvature. The sensitive element can be either platinum or nickel. Examples of the sensors are shown in figure 4.2.3-2a and b. The constant temperature anemometer measures the fluid velocity by sensing changes in heat transfer from the electrically heated film. The heated sensor is held at a constant temperature ratio to the ambient temperature using an electronic control circuit. Increasing the heating current flow to the sensor compensates for the cooling effect resulting from the fluid flowing past the sensor. The magnitude of the current increase required to keep the temperature constant is directly related to heat transfer. For laminar flow, there is little mixing in the boundary layer and the heat transfer is relatively low. For transitional flow, the mixing is very high in the boundary layer, and consequently, the heat transfer is very high. The mixing in the turbulent layer is less than in the transitional boundary layer but greater than in the laminar boundary layer. Sometimes it is difficult to tell whether a single hot-film sensor is in a laminar or a fully turbulent boundary layer, judging just by the signal magnitude. A reference hot-film sensor is needed for comparison in an area that is known to have a laminar boundary layer.

Anemometers used for hot-films in flight must compensate for the varying local temperatures as altitude and Mach number changes, to avoid overheating and burning out the hot-film. This can be done manually when there are crew persons to monitor and adjust the overheat ratio as necessary. This is, however, best accomplished using a temperature-compensated anemometer system similar to that described by Chiles [91, 92]. The system developed by Chiles requires no adjustment of the anemometer during or between flights of greatly differing airspeed or altitude profiles. The steady-state output of the anemometer is of sufficient quality to provide a real-time indication of boundary layer flow transition. This feature eliminates the need to analyze the high-frequency data for the entire test point or flight to determine the boundary layer state (laminar, transitional, or turbulent). This system exhibits very low noise, allowing the examination of the high-frequency data at those times of interest. A hot-film sensor with its temperature compensation element is shown in figure 4.2.3-3. If the sensors are being formed on a polyamide sheet, then the temperature-compensating element can be included also on the sheet. This is done by increasing the length of the temperature-compensating element film in relation to the length of the flow-sensor film, in proportion to the bridge ratio, so that the resistance of the compensating element is that required by the bridge. The sensor array shown in figure 4.2.3-2a, is in fact of this type with temperature-compensating elements adjacent to their respective flow sensors. When the desired number of hot-film sensors exceeds the available anemometer

circuits, hot-film sensor multiplexing using MOSFET solid-state switching [94] can be employed. The trade-off is a small increase in the noise of the output signal, which often may be acceptable.

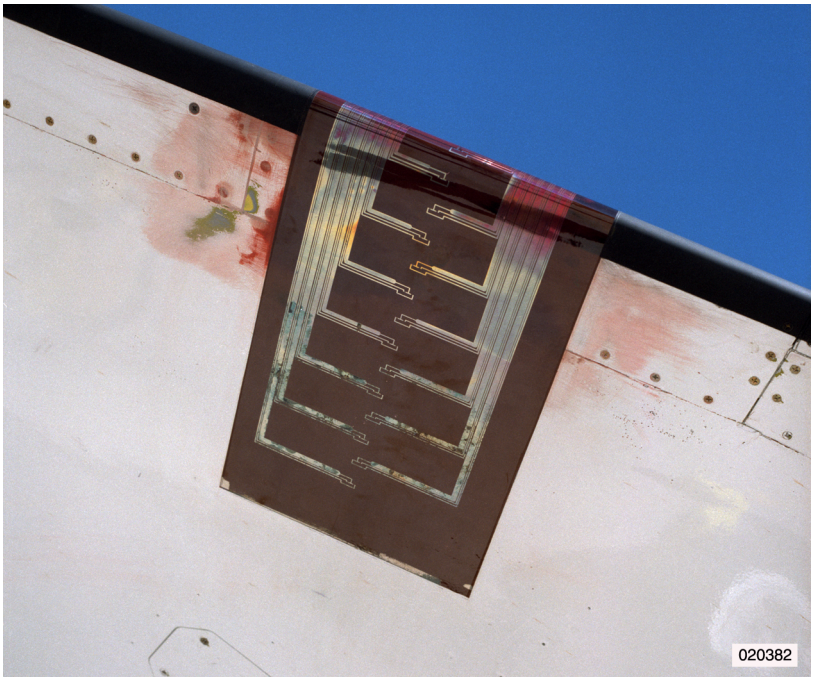

EC 96-43422-5

(a) Hot-film sensor array.

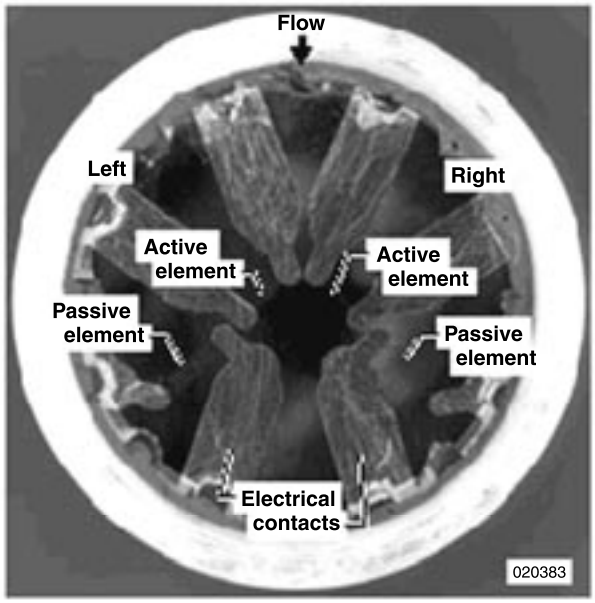

(b) High temperature dual hot-film sensor [62].

Figure 4.2.3.2. Sample hot-film installations.

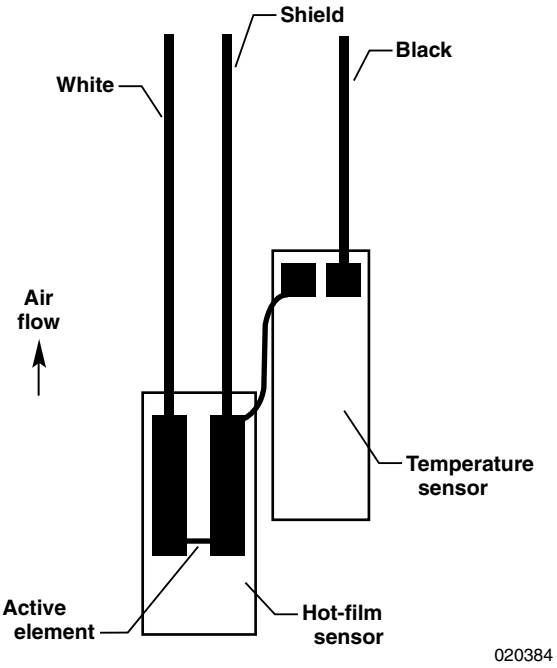

Figure 4.2.3-3. Hot-film with temperature compensation.

4.2.3.2 Interpretation of hot-film anemometer output signals

The primary use of hot-film sensors on an aircraft is to determine the local state of the boundary layer; laminar, transitional, or turbulent. In the case of a transitional boundary layer, proper interpretation of the anemometer output signal can provide a determination of the type of laminar instability leading to transition; i.e., Tollmien-Schlichting waves, crossflow instability, or attachment line contamination. It will be assumed here that there is a mechanism onboard the aircraft, or perhaps in the operation of the aircraft itself, which affects the extent of laminar flow at any given flight condition. This may be aircraft angle of attack, control surface deflection, or a controllable system for laminar flow control. The hot-film sensor array should be organized such that the anticipated transition front movement, as a result of applying this controlling mechanism, passes over one or more sensors. This procedure is often necessary because it may not be possible to determine a priori the state of laminar flow versus turbulent flow by examining the anemometer output signal. In theory, a hot-film anemometer signal for laminar flow would appear as a clean, noise-free quasi-dc trace, whereas for turbulent flow there would be a noticeable noise level in the signal because of the turbulent velocity fluctuations. All too often, however, electronic noise from sources on the test aircraft contaminates the anemometer output signal so that laminar flow appears similar to turbulent flow, although generally of lower amplitude. This situation can be made even more difficult if the signal recording, the signal display, or both are ac-coupled. In this case, the dc-level shift in the signal caused by the change in wall shearing stress is filtered from the output signal. The interpretation of the signal then depends on the time history of the intermittency behavior as the transition front passes over the hot-film sensor. The pattern of the intermittency behavior will be markedly different if the transition process is through TSI rather than if it is through CFI. For TSI, if the transition is from laminar to turbulent flow, the signal will show upward spikes initially, increasing in amplitude; this will be followed by a pattern of spikes, equally upward and downward; then finally by downward spikes, diminishing in amplitude until a constant amplitude noise level appears. An example of this is given in figure 4.2.3-4. An upward spike in the signal is produced by a “turbulent spot” in primarily laminar flow, and a downward spike in the signal is produced by a “laminar spot” in a primarily turbulent flow. A laminar spot, in reality, is a small region of laminar flow imbedded in the flow that has become time-wise majority turbulent. On the other hand, if transition is in the reverse direction, from turbulent to laminar, then the intermittency time history pattern just described will also be reversed. The most important aspect is to

remember that an upward spike in the signal means a turbulent spot in a laminar flow, and that a downward spike in the signal means a laminar spot in a turbulent flow. The procession of these signal spikes indicates which direction the Tollmien-Schlichting-based transition is proceeding; laminar to turbulent, or turbulent to laminar.

The transition process through crossflow instability appears completely different in the ac-coupled hot-film anemometer signal. Here the time history shows a pattern of groups or clumps of intermittency spikes interspaced with a low-level laminar signal. This is indicative of crossflow vortices moving laterally back and forth across the hot-film sensor. The vortices are in the process of transition and contain intermittency, while the regions between the vortices are still laminar. Figure 4.2.3-5 shows an example of this for a crossflow instability-driven transition front. When appropriate flow visualization is used, the crossflow transition front shows the distinctive saw-tooth pattern of laminar and turbulent regions. When one imagines the appearance of a hot-film signal as this laminar and turbulent pattern shifts laterally across a hot-film sensor, this shifting is, in fact, what is realized.

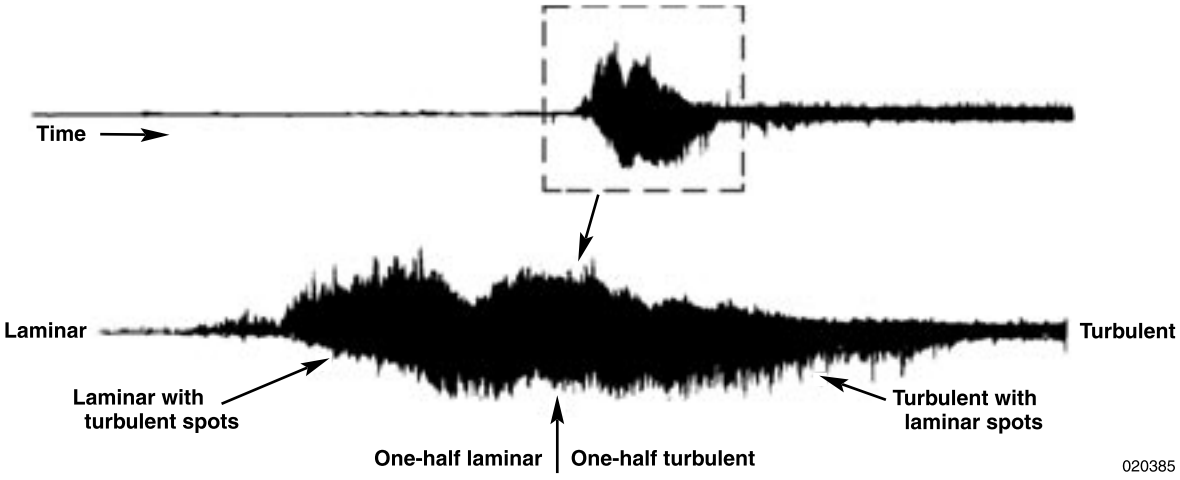

Figure 4.2.3-4. Boundary layer transition from laminar to turbulent for Tollmien-Schlichting instability as given by ac coupled hot-film sensor anemometer signal.

Figure 4.2.3-5. Boundary layer transition from laminar to turbulent for crossflow instability as given by ac-coupled surface hot-film sensor anemometer signals.

For the purpose of more detailed investigations on wave propagation in a wing boundary layer, it is often desirable to measure the absolute value of instability amplitudes expressed in dimensions of the flow rather than the pure output voltage from the anemometry system. As was explained above, the output signal of hot-film elements is connected with the rate of heat transfer from sensor into the flow. Hence, via Reynolds analogy, the output voltage $E = \bar{E} + e'$ may also be related to the instantaneous value of the wall shear stress $\tau_w = \bar{\tau}_w + \tau'_w$. Here, the line above (bar) denotes the mean value of the respective quantities, while the quotation mark stands for their time-dependent fluctuations. Considering only very small amplitudes being at least two orders of magnitude smaller than mean values, τ'_w may be identified from a Taylor series expansion as

$$\tau'_w = d\bar{\tau}_w / d\bar{E} \cdot e' \qquad (4.2.3\text{-}1)$$

A generalized King's law according to Bruun [95]

$$\bar{E}^2 = A \cdot \bar{\tau}_w^{1/n} + B \qquad (4.2.3\text{-}2)$$

can then be employed as the appropriate calibration relationship to obtain a characteristic curve $\bar{\tau}_w = f(\bar{E})$ and its derivative $d\bar{\tau}_w / d\bar{E}$. Of course, before applying equation (4.2.3-1), one has to find a suitable procedure to determine the mean wall shear stress at the hot-film position. In a flight test, this can be done on the basis of a wall pressure distribution measured simultaneously with the anemometer signal. Using a laminar boundary layer computer code, for example [96], one may then calculate $\bar{\tau}_w$ on any given location. Nevertheless, note that all data points for the calibration relationship must be taken at constant ambient conditions with respect to air temperature and density. Normally, this can be achieved by keeping the flight level constant throughout a test flight.

The feasibility of the approach described above has recently been verified in a flight experiment on the investigation of free-stream excited Tollmien-Schlichting waves [97]. Measurements were performed with a 64-element hot-film array attached to a laminar glove on a low-speed light aircraft, see figure 4.2.3-6. As a representative, the characteristic curve obtained for one of the hot-films is shown in figure 4.2.3-7. Based on such characteristic curves, time histories of signals from all hot-films were scaled. Figure 4.2.3-8, for example, shows τ'_w of nine sensor elements distributed with a spacing of 4 mm in spanwise direction at 37 percent chord. Disturbance amplitudes in this case are in the order of 0.6 mPa, while the mean wall shear stress in this case was 1.18 Pa.

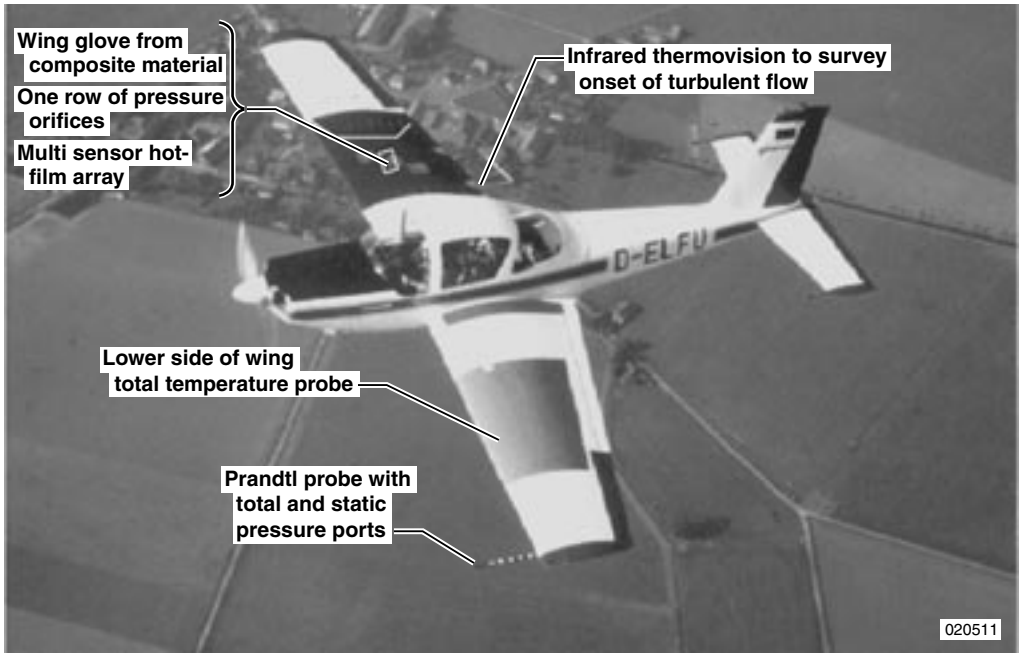

Figure 4.2.3-6. Test aircraft LFU 205 with 69-element hot-film array for investigation of T-S wave structures.

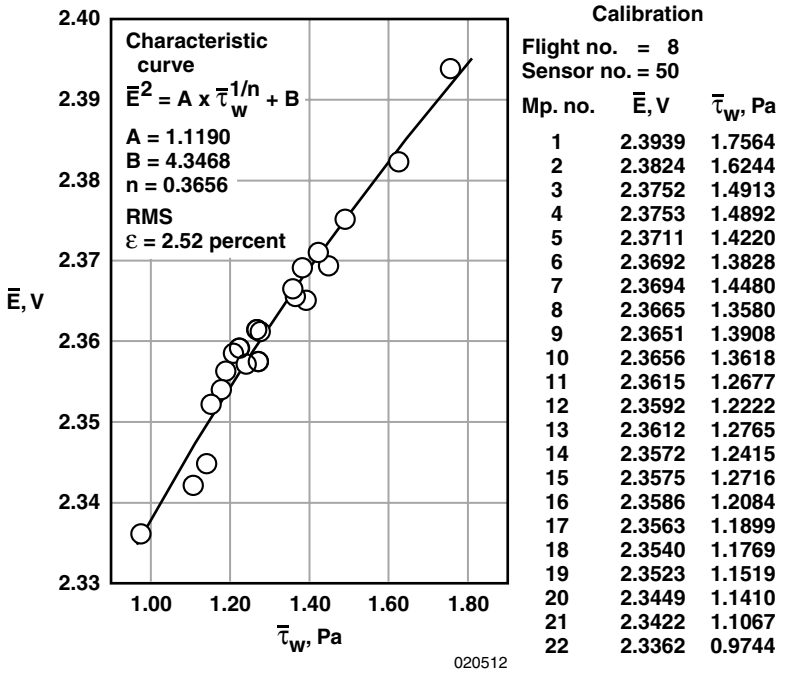

Figure 4.2.3-7. Calibration chart for a hot-film sensor.

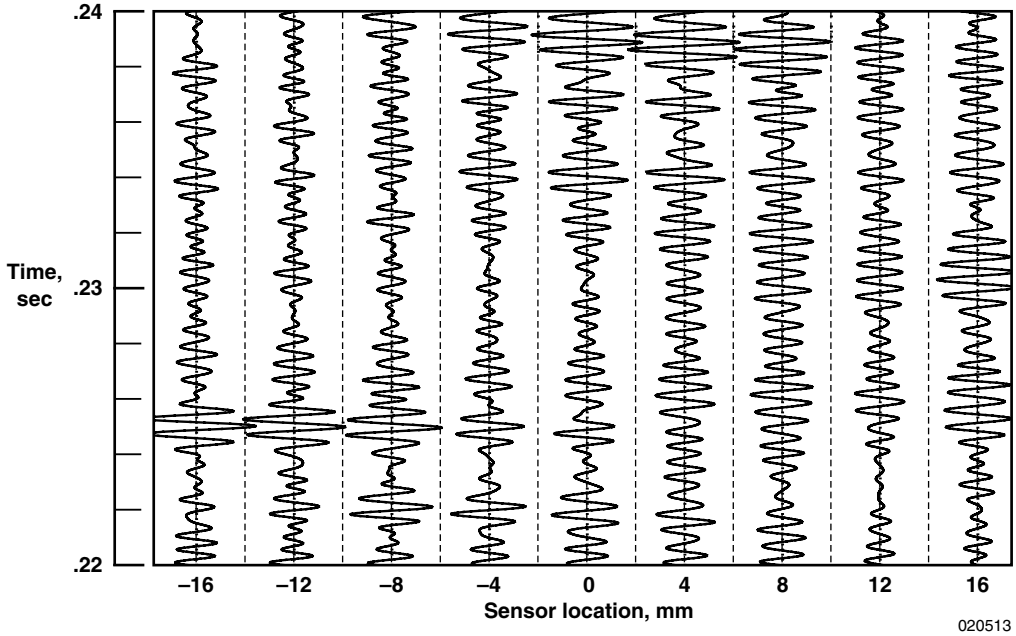

Figure 4.2.3-8. Scaled time histories of fluctuating part of hot-film signals.

4.2.3.3 Hot-wire anemometry

The initial development and first applications of the heat-flux sensor technique were for hot-wire sensors in the late 1940s. Hot-wire anemometry provided the first experimental confirmation of laminar boundary layer stability theory and was used extensively to investigate turbulent boundary layers. The diameters of the wires used vary, but typically are in the order of a few micrometers, say 2 to 5 μm or so. The length can be as small as 2 mm. Thus, the hot-wire sensor has an extremely small spatial resolution and is quite suitable for probing laminar or turbulent boundary layers with a thickness as small as 1 to 2 mm.

For many practical reasons, hot-wire anemometry tends to be used primarily in the laboratory environment, but has been used successfully in flight to measure laminar boundary layer velocity and instability disturbance profiles on a wing [98]. From a practical point of view, the use of hot-wire anemometry in flight, as compared to hot-film anemometry, is mainly limited to investigating questions regarding the structure of boundary layers; i.e., situations where the sensor is required to be positioned within the boundary layer at some distance away from the aircraft surface or perhaps traversing across the boundary layer from the surface to the external flow. Two practical concerns here are the fragility of the wire sensor, and a proper calibration that takes account of the varying physical properties of the air encountered in the flight regime of the investigation. Breakage of hot-wire sensors is almost always a result of human handling or other human activity near the sensor probe. When breakage occurs, then the sensor must be replaced and a new calibration performed. Proper planning for this can reduce the breakage problem to within reasonable practical limits. If the sensor probes are mounted externally on the test aircraft, then suitable protection covers should be utilized whenever the aircraft is on the ground.

Most often a hot-wire sensor is used to measure the flow velocity at the position of the probe. A calibration relationship between the flow velocity and the bridge voltage of the anemometer circuit must be established. The physical parameters that effect the heat transfer from the hot-wire sensor to the flow are the temperatures of the wire and of the flow, the density of the flowing fluid, and the velocity of the flow. In a laboratory, the respective temperatures and flow density are most often controllable, and are held constant for any particular test. The calibration function then has only the flow velocity as the independent variable. This form of the calibration function, which is known as King's Law [99] is

$$E^2 = (A + BU^{1/2})(t_w - t_a) \qquad (4.2.3\text{-}3)$$

Where E is the anemometer output bridge voltage, U is the flow velocity, t_w and t_a are the temperatures of the hot-wire sensor and the flow (respectively), and A and B are calibration constants to be determined. In flight applications, the flow density and temperature are also independent variables and a more mathematically complex relationship is needed. One developed by Miley and Horstmann [98] which has proved successful, follows:

$$A + BE^2 = k_f(t_w - t_a)(\mathrm{Re}_f)^a(\sigma)^b \qquad (4.2.3\text{-}4)$$

The variables E, t_w and t_a are the same as in the King's Law relation (4.2.3-3); k and σ are respectively the thermal conductivity and the sea level density ratio of the air; Re is the Reynolds number of the flow based upon the sensor wire diameter; A, B, a, and b are calibration constants to be determined. The subscript "f" denotes film conditions, that is, fluid conditions based upon the average of the sensor temperature t_w and the flow temperature t_a. The calibration constants A, B, a and b, are determined by using a non-linear least-squares solver on equation (4.2.3-4). It is necessary in this procedure to have a calibration data point for the no-flow condition, that is, flow velocity $U = 0$ $(\mathrm{Re}_f = 0)$. Otherwise, the nonlinear least-squares solver will drive the solution to $A = 0$, which will give a smaller sum-of-the-squares of the deviations, than for $A \neq 0$. Figure 4.2.3-9 shows a nonlinear least-squares curve fit to hot-wire calibration data from both flight and wind tunnel data for the same sensor. For demonstration purposes, in this particular case, the sea-level density ratio term $(\sigma)^b$ has been removed from equation (4.2.3-4). The effects of the density variation

between the flight data and the wind tunnel data are evident. Including the density ratio term σ, gives the result shown in figure 4.2.3-10. One sees here that data from a wide range of flow temperatures and flow densities collapse nicely to a single calibration curve. Some representative in-flight hot-wire data from reference [98] are shown in figure 4.2.3-11. Note the magnitude of the dimension for the boundary layer thickness. This provides some insight to the spatial resolution capability of a hot-wire probe.

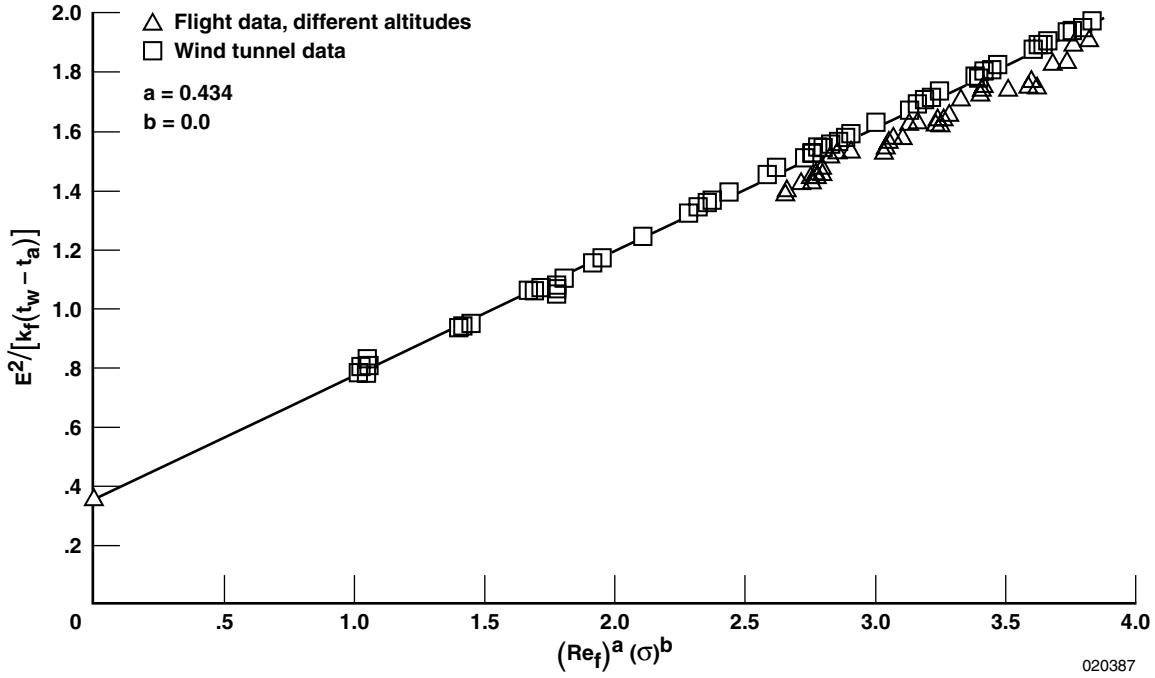

Figure 4.2.3-9. Hot-wire calibration results with the density ratio term inactive ($\sigma = 1$).

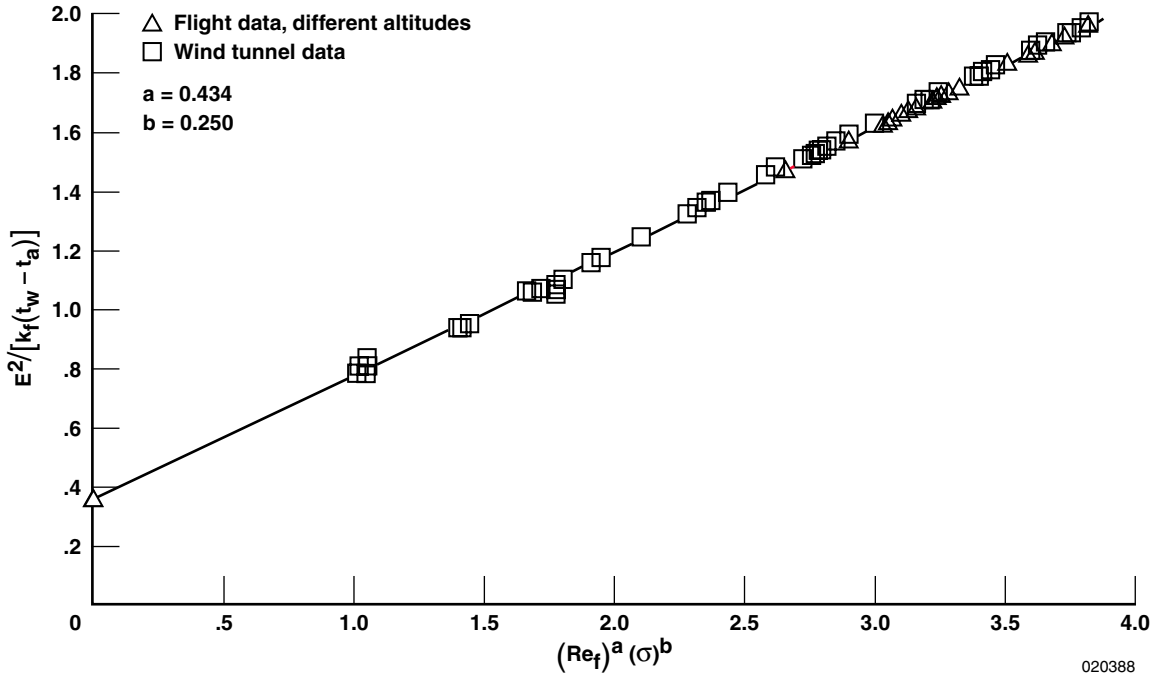

Figure 4.2.3-10. Hot-wire calibration results with the density ratio term active.

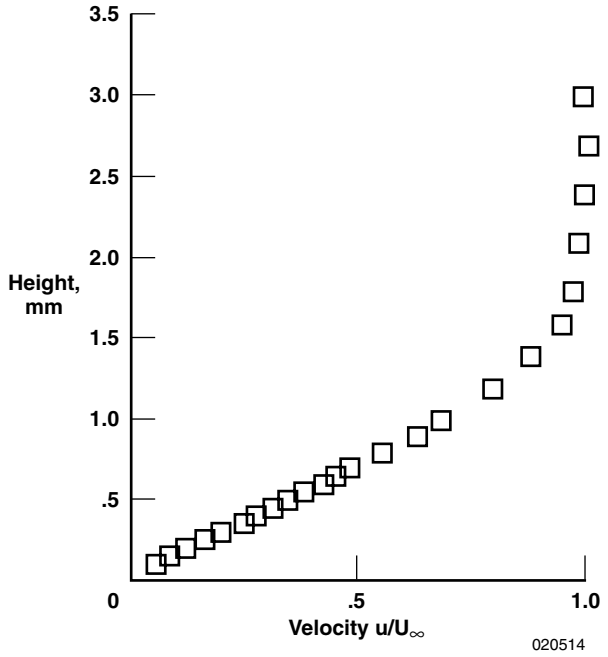

Figure 4.2.3-11. Measurement of laminar boundary layer velocity profile by hot-wire sensor, inflight, on wing of LFU 205 aircraft.

4.2.4 RAISED-PITOT TECHNIQUE

A simple technique to determine the state of a boundary layer on a surface is to use the raised-pitot technique [29, 100]. This technique indicates whether the boundary layer is in a laminar state or turbulent state, and was used in some of the earliest laminar flow flight tests [1, 4, 13, 14]. The technique can also approximate the location of boundary layer transition, using a simple calibration.

The raised-pitot technique relies on a small pitot tube (in this case 1.57-mm (0.062-in.) diameter) that is located at a height above the surface slightly greater than the thickness of the laminar boundary layer. This pitot tube is compared to a reference pitot placed far outside the boundary layer as shown in figure 4.2.4-1. For a laminar boundary layer, the thin boundary layer is beneath the raised pitot and the pressure measured is nearly the same as for the reference pitot. For a turbulent boundary layer, the raised pitot is immersed in the thicker boundary layer and a differential pressure is noted between the pitot and the reference probe.

The technique is calibrated by placing boundary layer transition strips spaced in front of the pitots. The calibration results are shown in figure 4.2.4-2 for the JetStar Leading Edge Flight Test experiment [25]. The calibrations are presented as a function of pressure ratio and cord location. The calibrations were unique for the upper and lower surface and for each test article. For a ratio of the differential pressure divided by the free-stream dynamic pressure less than 0.09, the flow was considered laminar. This curve, used for all flight conditions for this program, should be considered approximate at best. Functions such as altitude, Mach number, angle of attack, and span station should be considered when flight conditions are considerably different than the flight conditions for the calibration.

An example of data from a spanwise row of raised pitots behind a laminar flow control panel is shown in figure 4.2.4-3. The differential pressures between the reference probes and the raised pitots is plotted as a function of span. In this example, as the altitude increased from 10.4 km (34,000 ft) to 11.6 km (38,000 ft), more of the flow over the span of the wing became laminar. This figure from reference [25] shows the effect of Reynolds number (altitude) on the attachment line boundary layer.

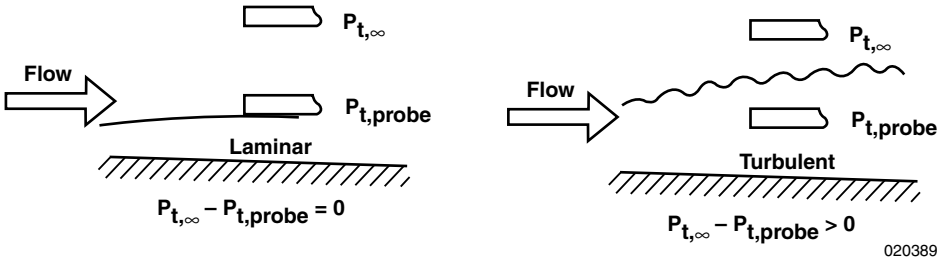

Figure 4.2.4-1. Raised-pitot technique schematic for laminar and turbulent boundary layers.

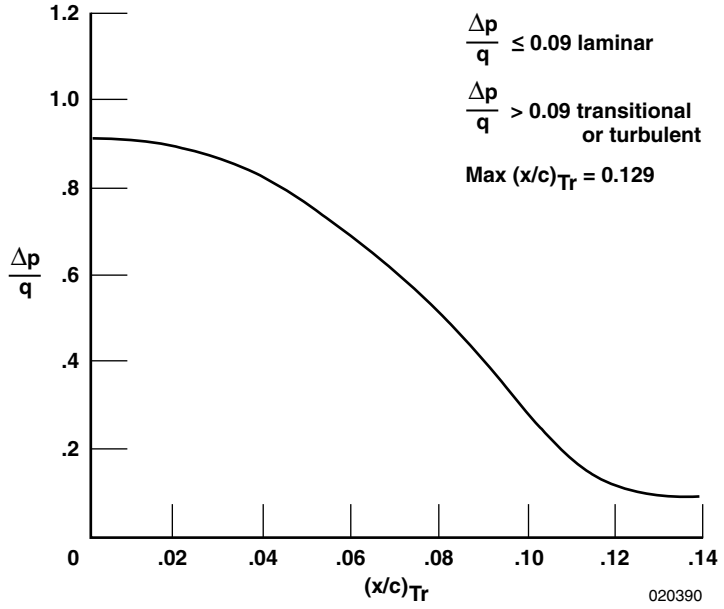

Figure 4.2.4-2. Raised-pitot calibration for JetStar LFC Leading Edge Flight Test article trailing edge with transition position, $M = 0.75$, $H = 11,582$ m (38,000 ft).

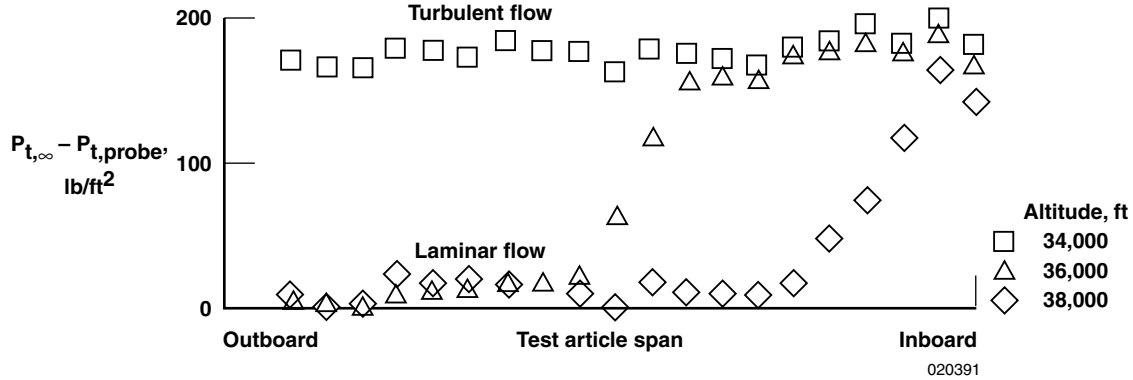

Figure 4.2.4-3. Results for the JetStar LFC showing effect of altitude on spanwise contamination using raised-pitot technique, $M = 0.75$.

4.2.5 TRAVERSING SURFACE PITOT

Small traversing surface pitots have been used in flight to measure the location of boundary layer transition. The first instance of this was by B. Melvill Jones at Cambridge University and was reported in 1937 at the 1st Wright Brothers Lecture [2]. Jones moved four pitots and one static probe along the wing of an airplane. One pitot rested on the surface of the wing while the others were distributed through the boundary layer. In figure 4.2.5-1, the laminar boundary layer velocity profile just before transition (1) is sketched with the turbulent boundary layer velocity profile just after transition (2). The horizontal lines in the diagram of fig. 4.2.5-1(a) represent the probe heights of the three probes in the boundary layer (lines A, B, and C), and the one probe outside the boundary layer (line D). In the diagram of figure 4.2.5-1(b), the pitot pressure is shown as a function of distance through the transition zone. While this method was very effective in locating boundary layer transition, Jones seemed to prefer the raised pitot techniques (see previous section) for estimating the location of transition to "within a couple of inches" (5 cm) for its simplicity.

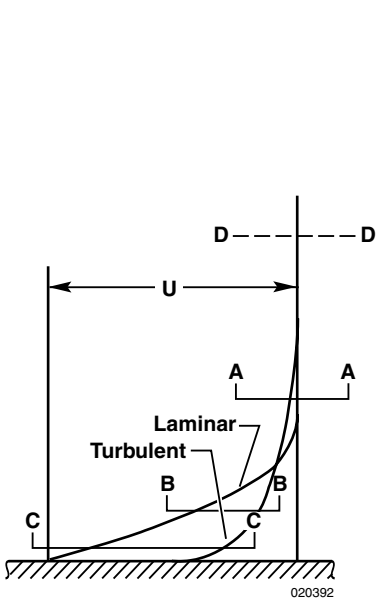

(a) Laminar, turbulent boundary layer profiles and probe A, B, C and D height locations.

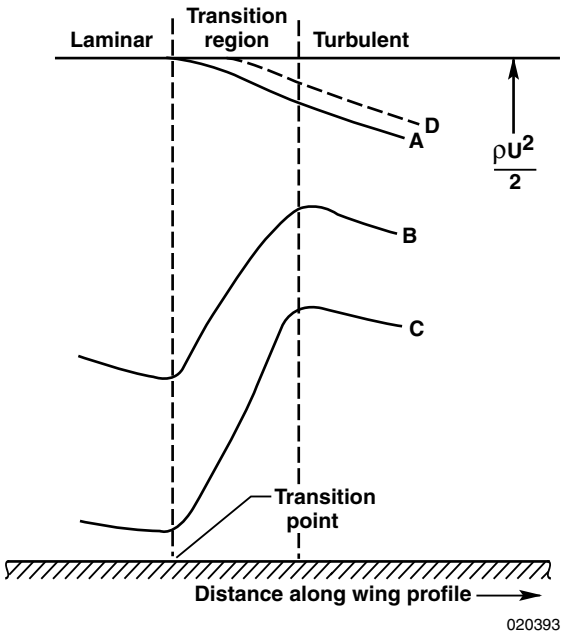

(b) Pressure profiles for probes A, B, C and D traversed through a laminar boundary layer, a transitional, and a turbulent boundary layer on a wing section.

Figure 4.2.5-1. Diagrams used for explaining the method used for location of the region of transition to turbulent flow, from Jones reference [2].

For the F-15 10-deg cone experiment [101, 102], a single, small traversing surface pitot was used to locate boundary layer transition on a highly polished cone that was tested in both wind tunnel and flight, fig. 4.2.5-2. The pitot was a chamfered 0.051 cm O.D. (0.020 in.) hypodermic needle flattened to 0.030 cm O.D. (0.012 in.), with a semiconductor strain-gage differential pressure transducer close-coupled in the probe, fig. 4.2.5-3. The pitot tip was held against the cone with spring pressure. Data was used from the probe only while it was slowly moving forward.

The probe was traversed along the cone surface using an electric motor and rack-and-pinion mechanism. While this mechanism previously had been used successfully in many wind tunnels, a structural analysis, a proof loads test, vibration tests, and environmental tests were required, since it would be mounted on an aircraft forward of the cockpit, figure 4.2.5-4. The environmental tests included operating the system in a chamber at the expected flight altitude and temperatures.

A typical example of the data is shown in figure 4.2.5-5. The absolute value of the pitot probe pressure was normalized with the free-stream total pressure and shown as a function of cone length. The onset of transition, x_{tr}, was defined as the minimum value of the pressure ratio, while the end of transition, x_{Tr}, was defined as the maximum value of the pressure ratio. The boundary layer, initially laminar, would grow in height; the surface pitot would sense lower pressures, following the pressure trace from front to rear. As boundary layer transition occurred, a mixing would occur in the boundary layer causing a sharp rise in the surface pitot pressure. When the boundary became fully turbulent, the boundary layer would grow in height and the total pressure on the surface would decrease while moving aft. Damania [103] showed similar results using fixed Preston tubes placed along the chord of a laminar flow control wing on a powered glider.

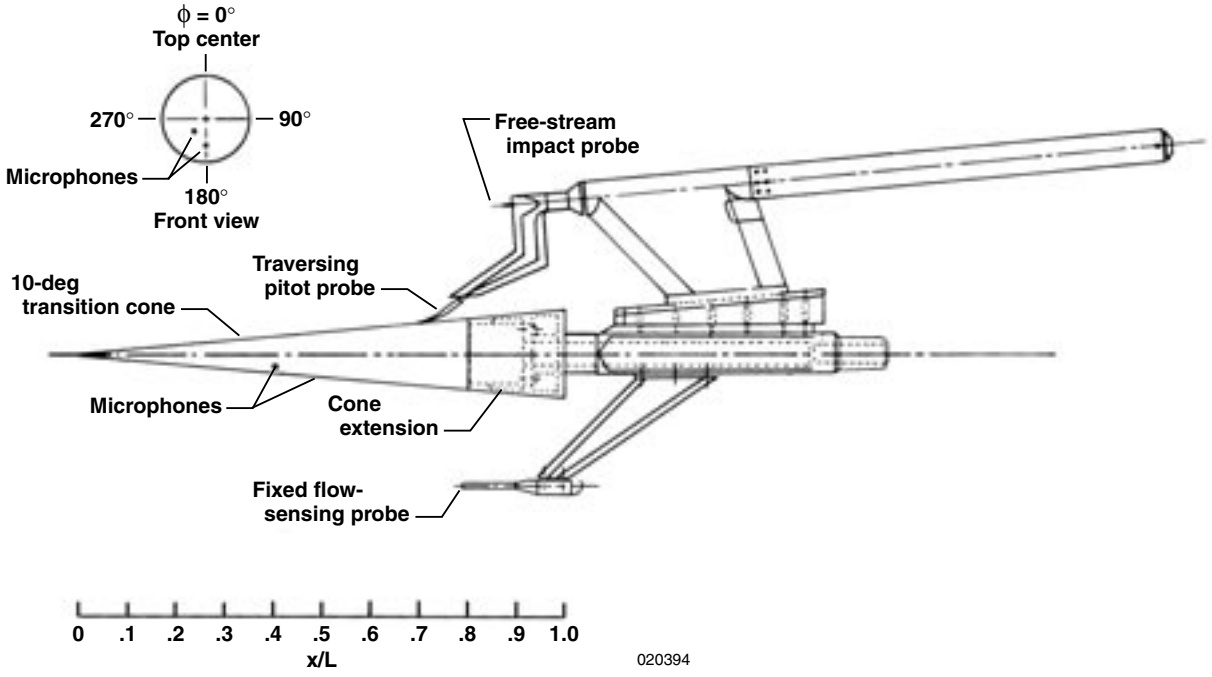

Figure 4.2.5-2. Ten-degree transition cone and instrumentation.

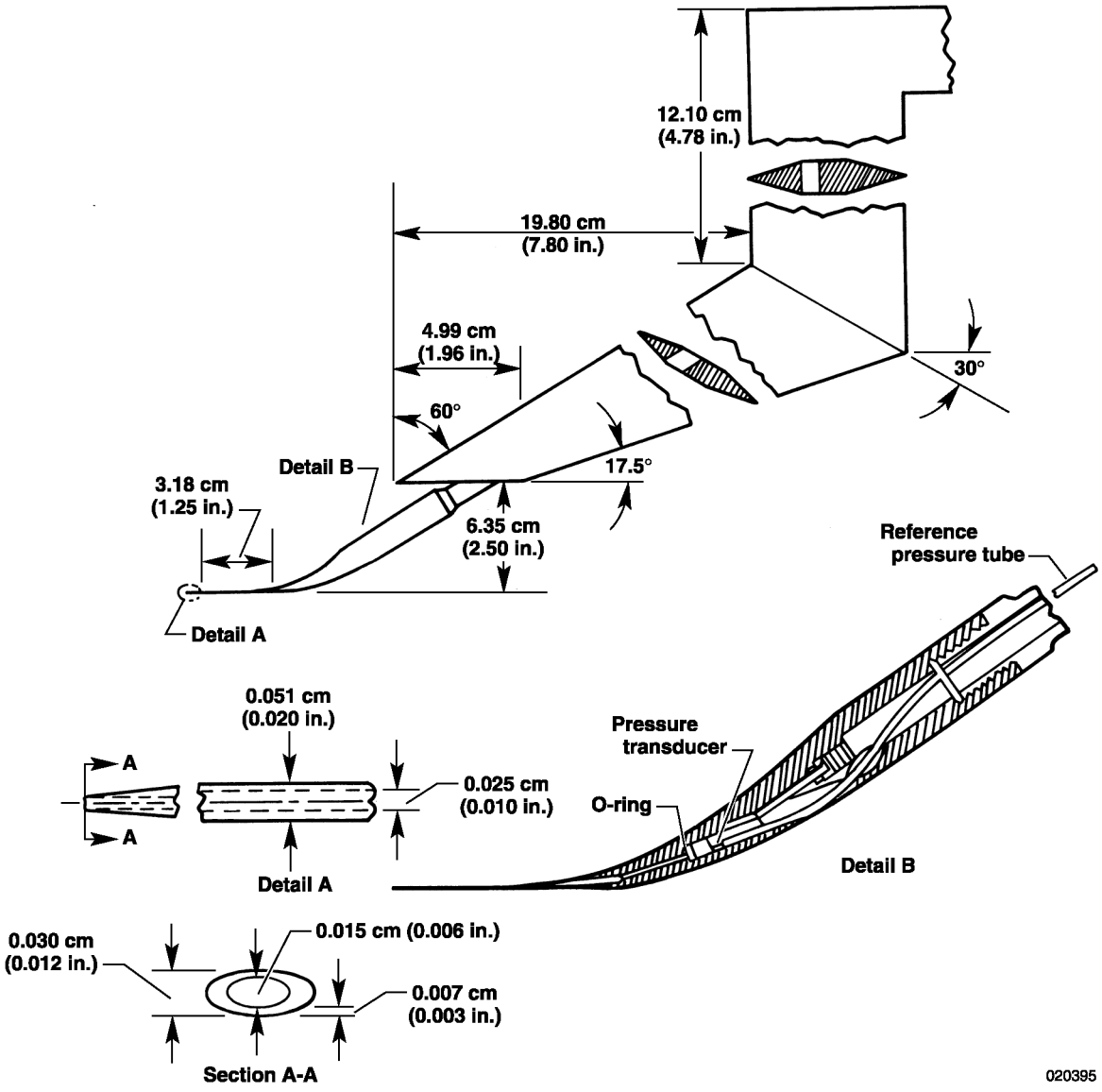

Figure 4.2.5-3. Pitot pressure probe. Dimensions are in centimeters (inches).

ECN 9859

Figure 4.2.5-4. Transition cone mounted in front of test bed aircraft.

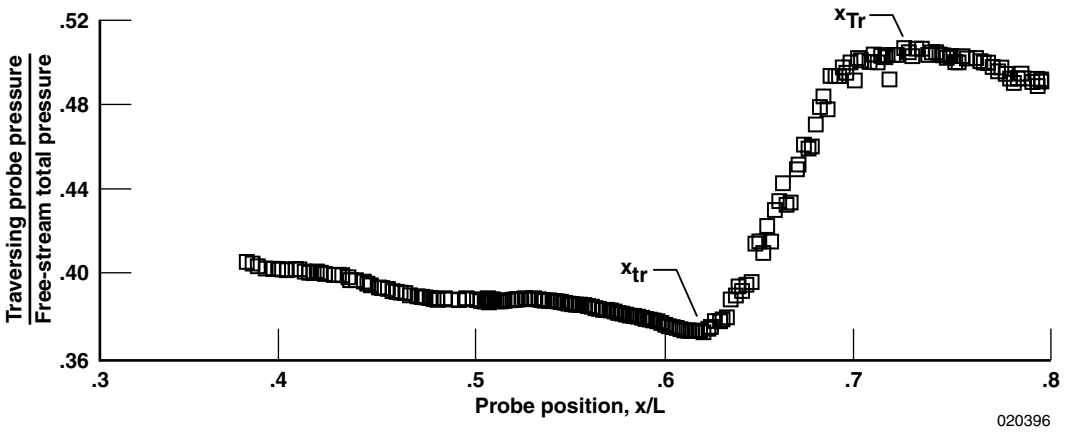

Figure 4.2.5-5. Typical pitot probe pressures as a function of probe position, $M = 1.44$.

4.2.6 EMITTED FLUID TECHNIQUE

The emitted fluid technique was developed primarily for flow visualization of surface streamlines and areas of separated flow and has been used successfully at Douglas Aircraft [104], and at NASA Dryden Flight Research Center [105, 106]. However, it has been used to give indications of boundary layer transition in flight. This method consists of emitting a small quantity of propylene glycol monomethyl ether (PGME) containing toluene-based dye from small-diameter surface tubes or orifices on the aircraft skin while the aircraft is at stabilized flight conditions. The flight conditions are held constant for 1 to 2 min. while the fluid evaporates and the dye sets or dries.

A plumbing schematic of the system used on the F-18 High Alpha Research Vehicle (HARV) is shown in figure 4.2.6-1. The PGME-dye reservoir shown is a hydraulic accumulator with an internal piston commonly used in aircraft hydraulic systems. Block valves, figure 4.2.6.2, were used to turn the flow to each orifice on and off. Each block valve permitted 32 fluid lines to be turned on or off at a time. Six block valves were required for the 192 orifices used. Each outgoing line was connected to a single orifice with nylon tubing. At each 1.17-mm (0.046-in.)-diameter surface orifice, an inline 0.51-mm (0.020-in.)-diameter restrictor was used, both to help limit the fluid flow while the system was operating and to retain the fluid in the line after the system was shut off.

The dye patterns of the surface streamlines and separated flow regions are documented by photographing the surfaces on the ground after each flight. Only one such data point can be obtained per flight and preferably, should be obtained at the end of a flight to prevent “contaminating” the dye pattern.

The emitted fluid technique was used to identify streamlines on the forebody and wing leading-edge extensions on an F-18 during flight testing at high angles-of-attack [107]. In addition to identifying the separation and attachment lines, the technique highlighted the laminar separation bubble as shown in figure 4.2.6-3. At high angles of attack, the fluid puddles at the laminar separation bubble, causing a kink in the streamlines. Note that where screw heads cause premature transition, the puddling and the kink in the steamlines are not present, confirming that the puddling was caused by the laminar separation bubble.

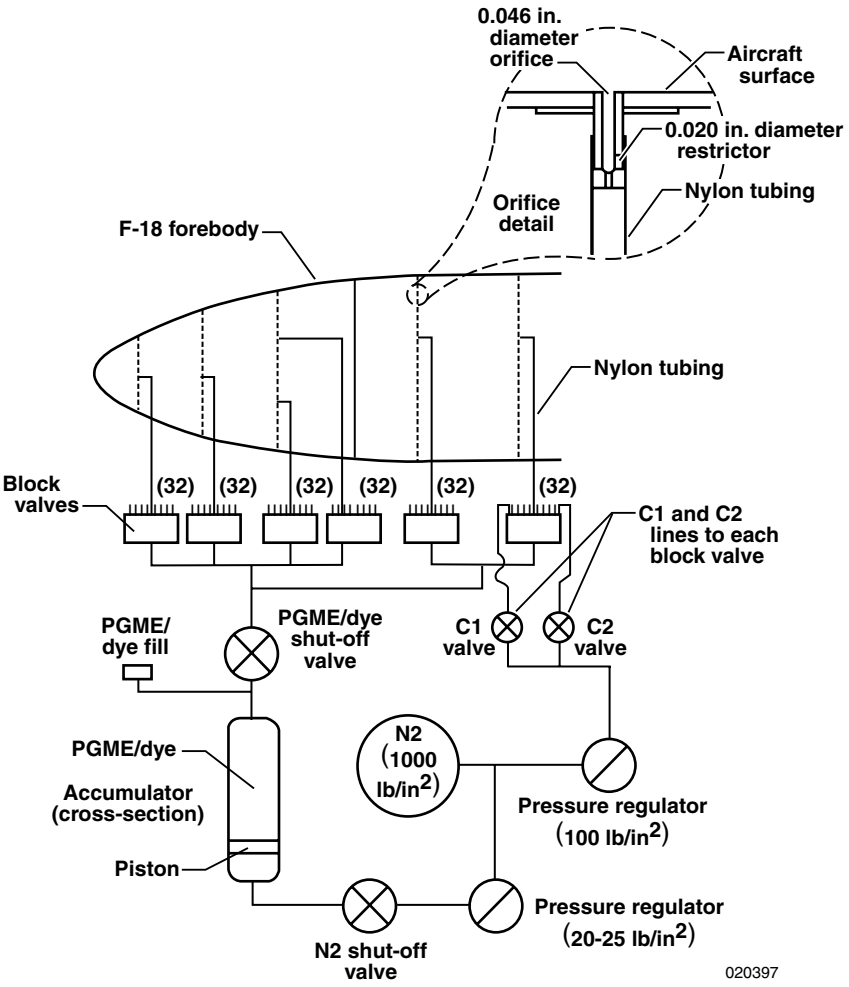

Figure 4.2.6-1. Schematic of F-18 surface flow visualization system.

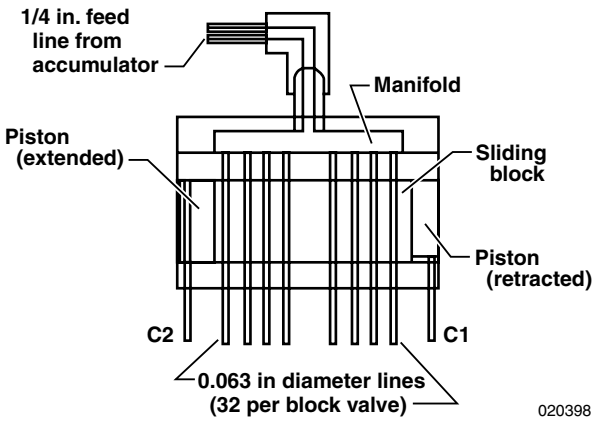

(a) Cross-sectional view.

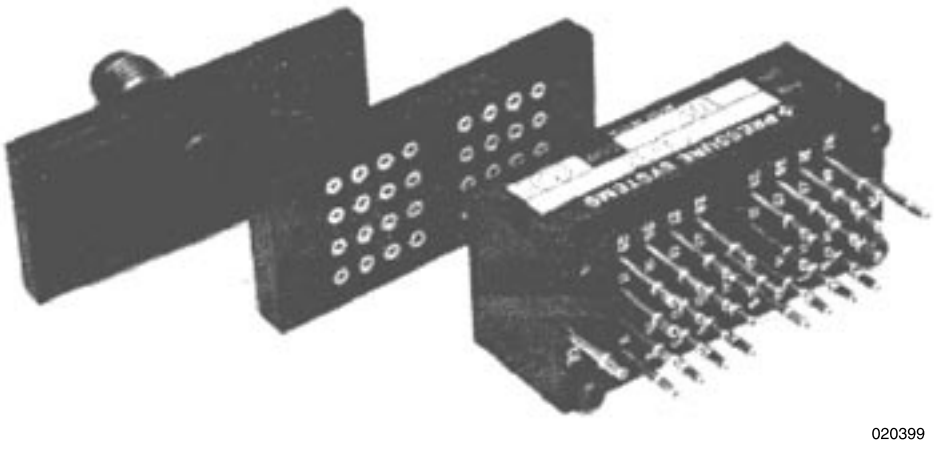

(b) Isometric view of assembly.

Figure 4.2.6-2. Modified block valves for surface flow visualization system.

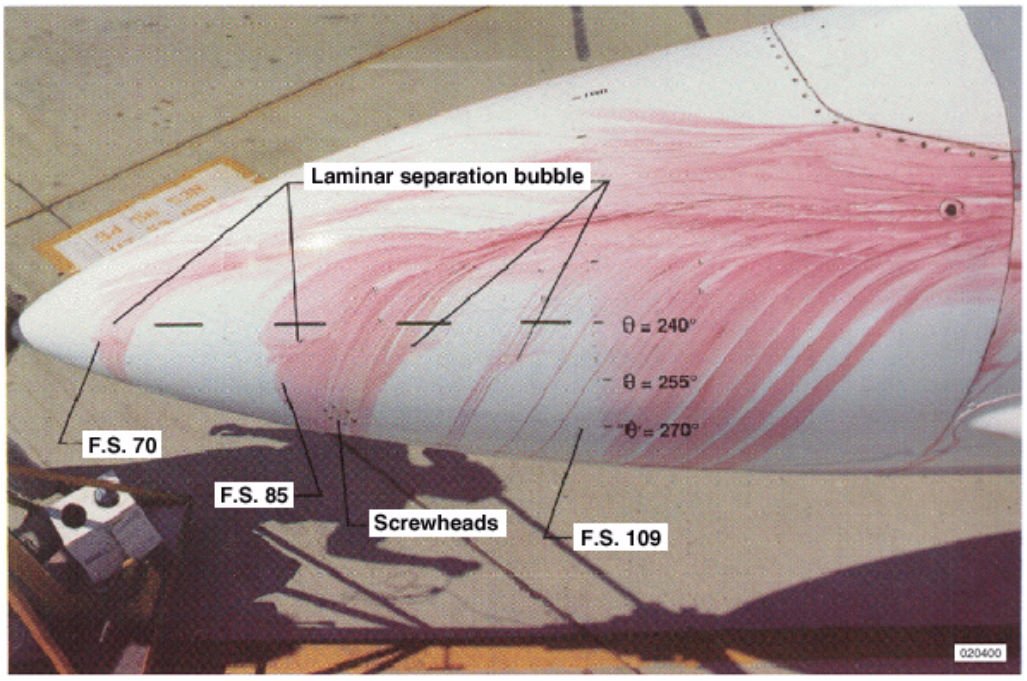

EC 88-0184-014

Figure 4.2.6-3. Laminar separation bubble identified on F-18 radome using emitted fluid technique, $\alpha = 47°$.

4.2.7 LIQUID CRYSTAL TECHNIQUE

Liquid crystals have been used to visually identify the location of boundary layer transition. The first application of this technique was on a model in the wind tunnel by Klein [108–110] while the first application in-flight was by Holmes and his associates at NASA Langley Research Center [111–113]. Liquid crystals can be formulated to be either temperature sensitive or predominantly shear sensitive. The shear sensitive (temperature insensitive) are usually preferred for flight tests because of the large variation in temperature with altitude.

Liquid crystals are in a state intermediate between that of a crystalline solid and an isotropic liquid. They are one of a unique substance (generally organic in nature) which do not pass directly from a crystalline solid to a liquid and vice versa. They possess the mechanical properties of liquids (fluidity and surface tension) and the optical properties of crystalline solids (anisotropy to light, birefringence). They also have unique properties not found in either solids or liquids. In particular, they can cause incident white light to be scattered selectively. The helical structures within a film of liquid crystals tend to align themselves so that the coating will scatter specific wavelengths of light in particular directions, similar to the scattering of a solid crystalline material. The scattering direction of a given wavelength, or color, is determined by the pitch of the helix, which is affected by temperature, shear stress, electromagnetic fields, and other environmental factors.[113,114]

The application of liquid crystals requires that the surface be cleaned of all dirt, grease, fingerprints, etc. [115]. The surface should also be colored flat black for best results, though adequate results have been obtained with a dark red or blue background [113]. A uniform coating is applied either with a spray gun or brush. Solvents such as acetone can be used to thin the liquid crystals. After the solvents have dried, the liquid crystals are ready for use.

The shear sensitive liquid crystals are unsealed and deteriorate with time, so should be removed and cleaned each day. They can be cleaned with acetone or a warm soapy water wash.

Figure 4.2.7-1 and 4.2.7-2 show examples of the use of liquid crystals to indicate boundary layer transition in flight. Figure 4.2.7-1 shows the location of boundary layer transition on the winglet of a Lear 28/29 [111] indicated by the change in color of the liquid crystals from blue to yellow. This was one of the first uses of liquid crystal in flight and used temperature-sensitive liquid crystals. For best results, temperature-sensitive liquid crystals should be used on an adiabatic surface, i.e., one that is insulated or has a low coefficient of thermal conductivity.

In figure 4.2.7-2, boundary layer transition is shown on a fiberglass glove on an F-14 on a section that had been painted black for good contrast [34]. For the F-14A tests, the shear sensitive liquid crystal (called "pressure-sensitive" by the manufacturer) was applied to laminar flow wing gloves on an F-14A aircraft approximately one hour prior to takeoff. Boundary layer transition is noted by the abrupt change in color in the liquid crystal coating. The colors themselves are not important because they change with viewing angle as well as ambient temperature.

Figure 4.2.7-2 (a) represents a case where transition occurred forward on the test section, probably because of cross-flow disturbances generated by leading edge sweep and is indicated by the sawtooth pattern at approximately 5- to 10-percent chord. Figure 4.2.7-2 (b) represents a case where transition occurred about midchord, as a result of the laminar boundary layer encountering an adverse pressure gradient and is indicated by a uniform line at about 30-percent chord. One other observation in figure 4.2.7-2(b) is the presence of a "transition wedge" near the outboard edge of the test section, probably because of an insect impact or dust stuck in the oily liquid crystal mixture.

A comparison of the boundary layer transition location was made with hot-film sensors on the same glove, with and without liquid crystals applied for altitudes below and above 25,000 ft (7,620 m) as shown in figure 4.2.7.3. The data without liquid crystals were obviously not flown on the same flight as the data with liquid crystals. The location of transition is plotted as a function of angle of attack. At low altitudes, all of the transition data obtained with liquid crystals on the glove surface fall below the transition obtained without the liquid crystals on the glove. At high altitudes, the comparison is much better and there is only a 5 percent variation in the transition location [38].

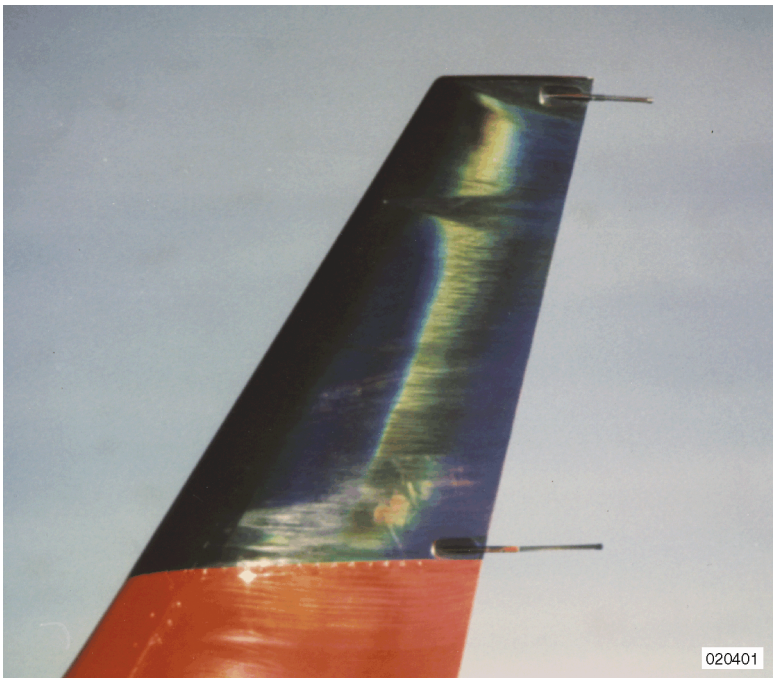

NASA Langley Research Center Photo L-86-1401

Figure 4.2.7-1. Transition visualization using liquid crystals on the Lear 28/29 airplane winglet.
Pressure altitude 48,000 ft., M = 0.8, leading edge sweep = 31°

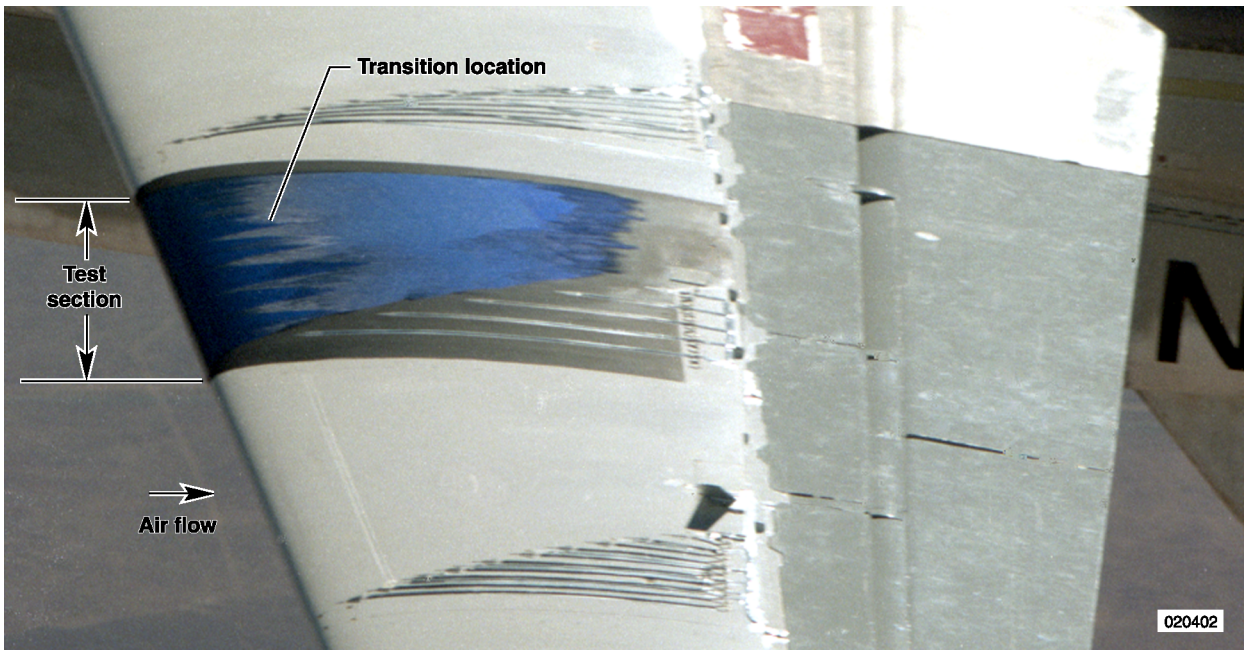

EC 86-33600-018

(a) Sawtooth transition front.

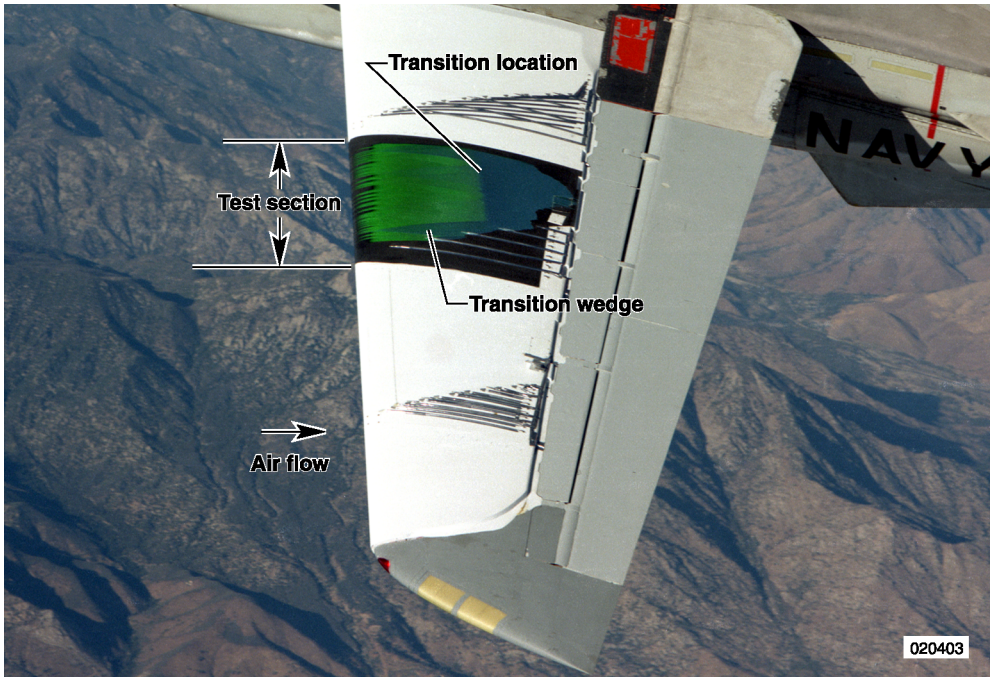

EC 86-33600-016

(b) Uniform transition front.

Figure 4.2.7-2. Examples of shear sensitive liquid crystals on F-14A glove section.

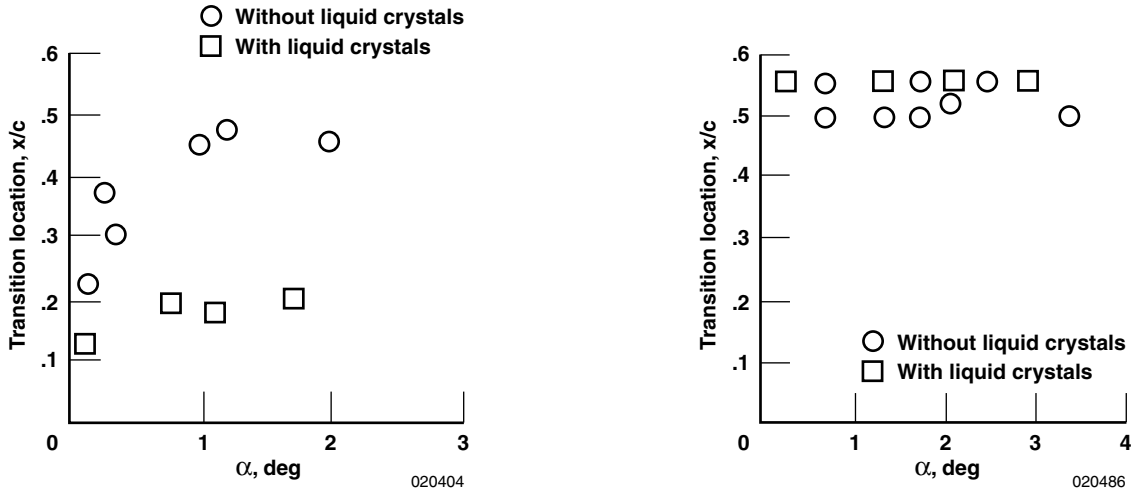

(a) Below 25,000 ft (7,620 m).

(b) Above 25,000 ft (7,620 m).

Figure 4.2.7-3. Comparison of boundary layer transition with and without liquid crystals.

The advantages of liquid crystals in-flight are that they give a global view of boundary layer transition, they are easy to apply, and only require a camera for documentation. They are highly responsive [116] and several data points can be obtained on a flight before the liquid crystals are scrubbed away. The disadvantages are that, first, with liquid crystals applied insects and dust tend to adhere to the surface in greater amounts causing localized turbulent regions seen as wedges in the liquid crystal coating as shown in figure 4.2.7.2. Secondly, the uneven application of the liquid crystals can cause color changes in the liquid crystal pattern, interfering with the interpretation of the pattern. Therefore, care must be taken to ensure a uniform coating during application. Lastly, at low altitudes, i.e., below 25,000 ft (7,620 m), or increased unit Reynolds number, the liquid crystals can affect the transition location [38]. This effect can be reduced if the coating is applied on a flat paint surface in a uniformly thin manner such that the scrubbing or movement of the coating is minimized.

4.2.8 SUBLIMATING CHEMICALS TECHNIQUE

Clifford J. Obara, NASA Langley Research Center, Hampton, VA USA

The chemical sublimation method for indicating boundary layer transition was developed in the mid 1940s at the Royal Aircraft Establishment [117, 118]. Originally devised for low-speed wind tunnel testing, the method was extended to aircraft in flight with the introduction of more durable coating materials [119]. The sublimation method for indicating boundary layer transition has the advantages of simplicity, speed, low cost in operation, and capacity to provide a very detailed graphic record of the transition from laminar to turbulent over the test surface. In addition, the technique can indicate regions of laminar flow separation. The method has been proven capable at speeds up to Mach 2, at temperatures down to –55 °C and at altitudes up to 55,000 ft [9, 10]. Several chemical solids have been found to be suitable diffusible coating films. These chemicals have high melting points, no adverse effects on surface finishes, and low vapor pressures for acceptable sublimation times of from five to sixty minutes. The method is a versatile technique in investigating boundary layer phenomena in both flight and wind tunnel testing.

The procedure of the sublimation method involves coating the surface to be observed with a very thin film of volatile chemical solid. During exposure to the freestream airflow, areas develop in which the chemical film sublimates more rapidly because of greater local shear stress or skin friction within the boundary layer such as that found in turbulent flow. The regions near stagnation on the surface will also see high shear

stresses and hence greater rates of sublimation. The stress-induced heating produces the different rates of sublimation.

There are several criteria necessary for the coatings to remain solid, opaque, and durable at the temperatures at which transition indications are obtained and examined. The chemicals must have a high melting point, be resistant to moisture, have no adverse effects on surface finishes, have low vapor pressures for aerodynamic use, and be solvent in a fast evaporating carrier. These considerations restrict the possible compounds of solids with melting points above 50 °C, low or medium molecular weights, and containing much hydrogen. The types of solid compounds suitable are hydrocarbons, esters, alcohols, ethers, ketones, acylamines and azohydrocarbons [117]. Another consideration for selecting an appropriate chemical is safety from health hazards associated with the use of such compounds. Four useful compounds which meet these requirements and provide a practical range of operating characteristics (sublimation rates) are naphthalene, biphenyl, acenaphthene, and fluorene.

The solvents used must be of low toxicity, low corrosiveness, and be highly volatile. Water and the low-volatility alcohols have insufficient vaporizing characteristics to be used as solvents. Some of the esters, which are low in toxicity are corrosive to metals in long-term use. The solvents found to be most suitable are acetone and light petroleum fractions. Recent restrictions on the use of many candidate solvents because of ozone contamination, have reduced the choices for a suitable solvent. The commercially available genesolv has worked well, leaving a thin, non-crystalline, white film of diffusible chemical solid. Acetone is another viable candidate solvent if used in a well-ventilated area (because of its flammability). The requirement for a highly volatile solvent is a result of the process by which the sublimating chemicals are applied to the surface. The chemical is applied to the test surface by compressed-air spraying with a technique called “dry-spraying.” The solution is applied to the surface in such a manner that the solvent is almost completely evaporated before the solution has time to wet the surface, leaving the sublimating chemical coating on the surface. Proper spray technique will produce a powdery matt appearance of the chemical coating; when the spray goes on too wet, the coating appears crystalline. After spraying, the chemical coating can be brushed with a soft bristle brush, wiped with cheesecloth, or rubbed with a gloved hand to loosen large chemical particles which can adhere to the coating and cause turbulent wedges.

In order to provide quality photographic reproduction of the developed chemical pattern, it is recommended that the test surface be painted a dark, contrasting color such as flat black. For times when the surface cannot be painted, food coloring added to the solution prior to spraying has worked well to enhance the contrast. Keep in mind however that some dyes may leave a slight discoloring of the test surface. An intentional boundary layer trip placed near the leading edge is useful for indicating the rate of transition pattern development in the chemical coating. Applied in the manner described, the thin layer has had no first-order effects on the measured transition location.[21]

Sublimating chemicals have been used extensively in flight and wind tunnel applications to document the location of boundary layer transition on wings, fuselages, propellers, and empennages.[21] From this experience, it has been possible to determine the boundary layer transition mechanism or mode by analysis of the chemical patterns which develop.[120] Typical patterns for the four most common modes of transition are shown in figure 4.2.8-1. The developed pattern is shown as white in the laminar region. Tollmien-Schlichting instability transition is characterized by a ragged transition line as shown in the top pattern. A crisp, straight transition front indicates the presence of laminar separation. When there are streamwise striations in the chemical coating followed by a very jagged or sawtooth transition line, crossflow or Görtler instability can be the transition mechanism. The fourth common transition pattern is formed by three-dimensional roughness elements. A typical shape would consist of a thin trail behind the element followed quickly by a turbulent wedge.

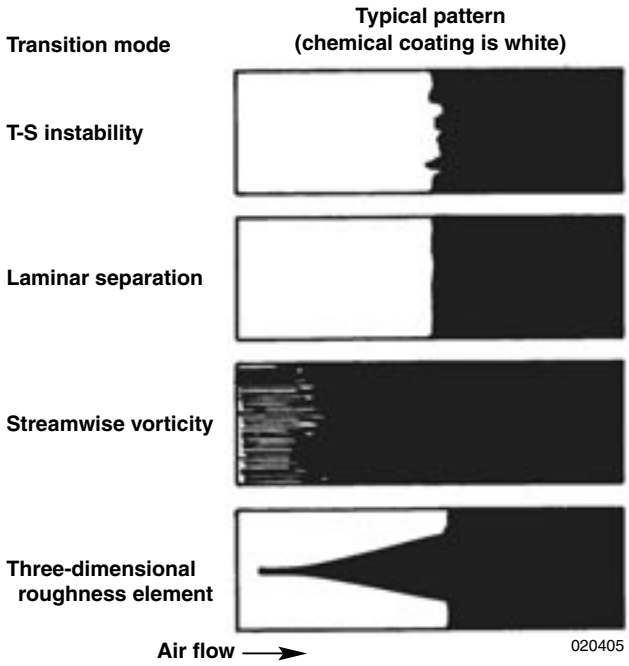

Figure 4.2.8-1. Transition mode characteristics in sublimating chemical patterns.

Figure 4.2.8-2 shows the transition pattern on the winglet of a business jet aircraft. This test was conducted at a Mach number of 0.5 and a unit Reynolds number of 2.1×10^6 ft^{-1}, using acenaphthene. On the upper span of the winglet, the transition front at around 65 percent chord is very smooth and straight, characteristic of laminar separation. Around midspan a roughness particle prematurely tripped the boundary layer. A third mode of transition appears in the lower-span region. Between 5 and 10 percent chord, there is a manufacturing joint with an aft-facing step and several screw slots. The screw slots were not smoothed over and, consequently, in the one region, they caused premature transition. In the lowest region of visible chemicals, the aft-facing step was the cause of premature transition. This particular test was somewhat unique in that the flightpath included a rapid ascent to the test condition, around 20 minutes of on-condition time to establish the chemical pattern, and a rapid descent to landing. The off-condition portions of the flight did not alter the transition location and final photographs were actually taken on the ground.

An example of crossflow vorticity transition is shown in figure 4.2.8-3. This test was conducted on another business jet with a wing sweep of 27 deg at a unit Reynolds number of 2.4×10^6 ft^{-1}. The photo shows the lower surface of the wing near the root. Prior to causing boundary layer transition, the vortices were spaced at 8 to 10 per inch.

A comparison of the sublimating chemical and liquid crystal flow visualization techniques is shown in figure 4.2.8-4. The test was conducted in the NASA Langley Research Center 14x22 Foot Wind Tunnel on a business jet fuselage forebody [112]. The results show good agreement between the two techniques. The small region of jaggedness in the transition front on the side of the forebody was caused by disturbances from a three-dimensional roughness near the nose. The two methods produced the same surface patterns in response to the roughness, illustrating similar sensitivity to transition phenomena.

Application of the sublimating chemical technique for measuring boundary layer transition can be useful in the design or computational fluid dynamic validation of a wind tunnel model or flight vehicle. The technique can identify the transition location as well as the transition mode such as boundary layer instabilities, laminar separation, or transition because of roughness over a range of test conditions from low-speed to supersonic. The largest limitation to the method is that only one test point can be obtained per application.

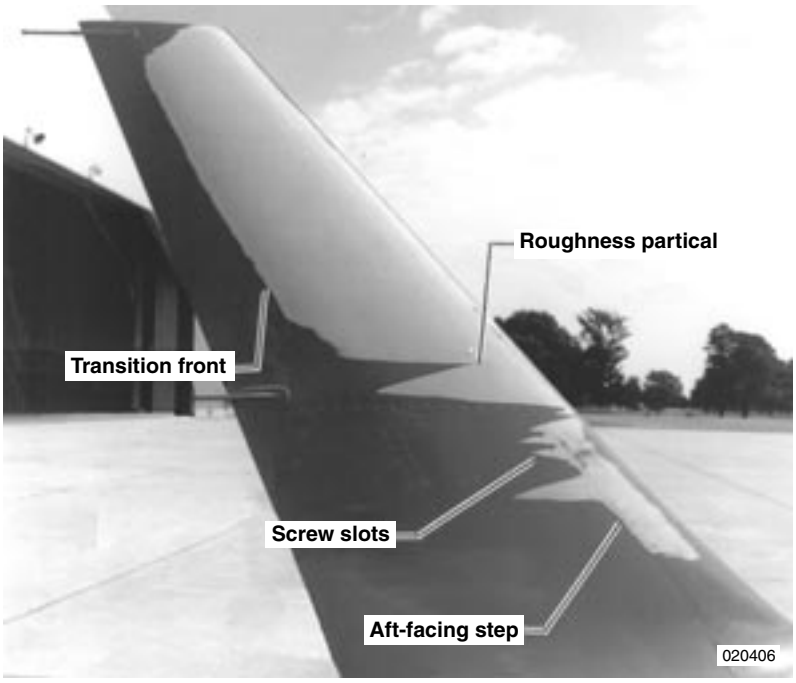

Figure 4.2.8-2. Boundary layer transition on a winglet surface indicated by sublimating chemicals, $Re = 2.1 \times 10^6 \text{ft}^{-1}$, M = 0.50 .

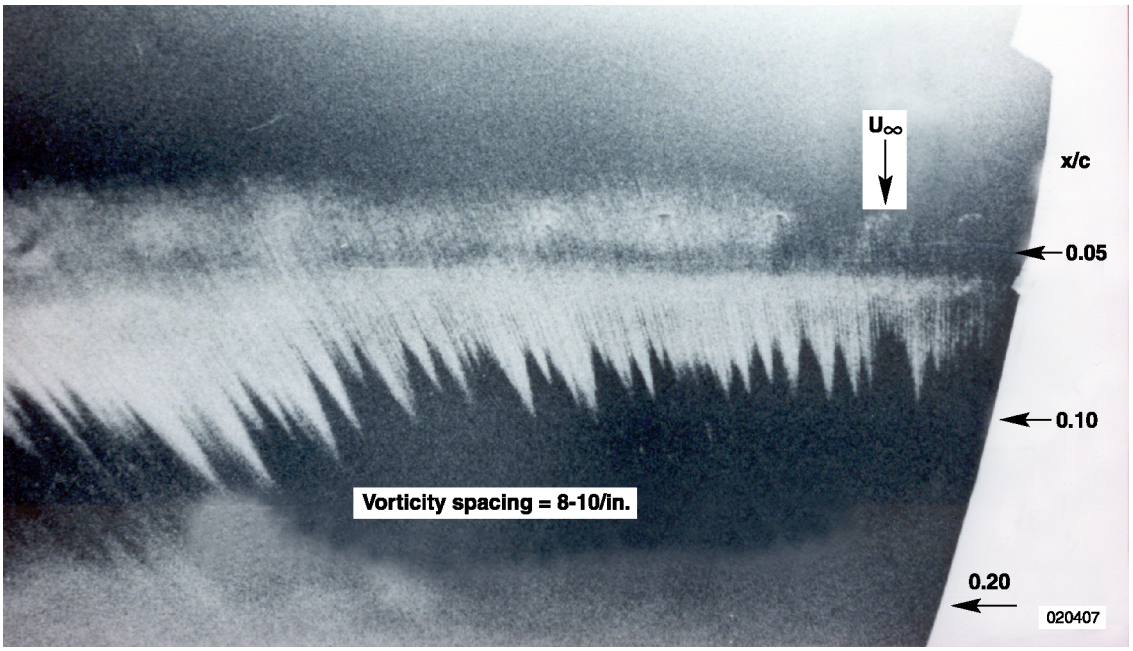

Figure 4.2.8-3. Crossflow vortices indicated by sublimating chemicals, wing sweep = 27°, $Re = 2.4 \times 10^6 \text{ft}^{-1}$.

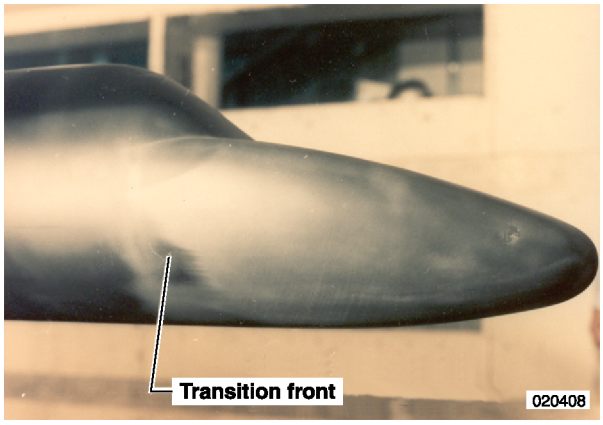

(a) Sublimating chemicals.

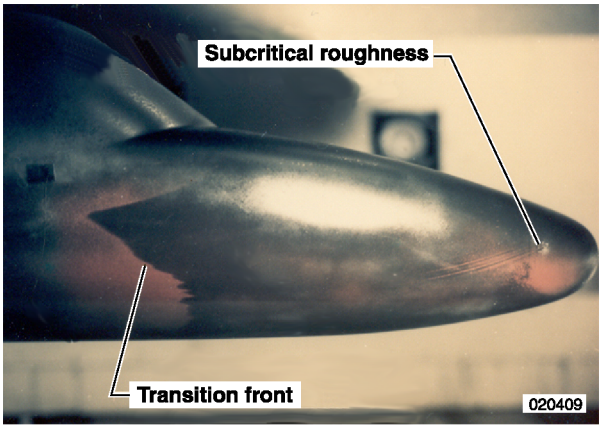

(b) Liquid crystals.

Figure 4.2.8-4. Comparison of boundary layer transition visualization methods.

4.2.9 Oil flow painting technique

The oil-flow painting technique is used to get qualitative information about the local surface shear stress of the boundary layer. On horizontal surfaces, such as wings and elevators, the technique can reveal regions of strong gradients of shear stress and regions of no shear stress as indicated by an unchanged initial painting pattern. On vertical surfaces, such as fins, gravity forces and shear stress forces result in an inclination of the oil-flow lines which is sensitive to the local shear stress. The oil painting technique can identify laminar and turbulent separation lines, determine the location of laminar-to-turbulent boundary layer transition, show turbulent reattachment lines, and the location of termination shocks from local regions of supersonic flow. Thus, boundary layer flow separation and the laminar-to-turbulent transition process can be investigated in detail using the oil painting technique.

The paint mixture generally is a combination of oil and pigments. The pigment color should be in a sharp contrast to the color of the surface to be investigated. Powdered black graphite or red or yellow paint pigments are frequently used. The paint mixture should consist of one-quarter to one-third pigment to three-quarters to two-thirds oil by volume. The portions have to be mixed very carefully to avoid lumps that could induce transition.

The type of oil and its viscosity must be determined in flight. The selection depends on the flight speed and on the temperature at the test flight altitude. The higher the flight speed, the higher viscosity requirement for the oil. At high test altitudes, the decreasing temperature needs to be considered. At low speeds and low altitudes it might be necessary to reduce the viscosity of the oil by means of kerosene. For investigations on sailplanes, DLR has good experience with a mixture of paraffin oil, kerosene, and red paint pigments in equal portions by volume.

The aircraft test surfaces must be cleaned of dirt and other substances that could affect the oil patterns, see [121]. The whole surface structure should be as uniform as possible in order to avoid oil-flow behavior governed by surface discontinuities instead of boundary layer flow. Correlation of the oil-flow characteristics with geometric measures, and tick marks of constant chord ratios should be applied on the surface.

The paint mixture can simply be applied on the test surface with a paint brush. Usually the whole test surface will be painted. It must be taken into account that the paint mixture itself could have an influence on the boundary layer development. A simple technique to determine if there is any interference from the paint mixture is shown in figure 4.2.9-1. The oblique upstream pattern of the paint mixture area results in boundary layer flows with distinct upstream extents of paint mixture surface. If in this case e.g. the transition location or the extent of the laminar separation bubble is similar in span direction, it can be stated that the paint mixture has no effect on the flow.

The oil-flow patterns developed on the test surfaces are usually documented by photographs taken, either from a chase aircraft, from an on-board camera, or after flight on the ground. In the latter case, only one flight condition can be investigated in a flight. The flight test condition must be trimmed immediately after take off and kept nearly constant until touchdown. In case of in-flight photographs, different conditions can be flown and documented. The test time is limited by the loss of oil, to between 10 to 30 minutes. To ensure a correct interpretation of the photographs, it is very helpful to record the whole development of the flow patterns with a video camera.

NASA has used this technology over a broad band of speeds, flight levels, and types of aircraft. Curry, Meyer and O'Connor reported in [122] oil-flow painting tests on fighter aircraft, a drone, and a glider. A survey of each aircraft used and of the oils and pigments employed are listed in table 4.2.9. The test flight envelope for a particular aircraft at which photographs were taken is shown in figure 4.2.9-2.

Table 4.2.9. Summary of Flight Experiments.

Aircraft	Flight-test period	Number of flights	Oil solutions tested	Pigment
F-111 TACT/NLF	August 1980	4	Chevron 80W-90	Graphite
AD-1	May-June		AMS/Oil Synthetic Gear Lube (EP)	
			AMS/Oil Para-Synthetic Engine Oil	
		5	Chevron 80W-90	FeO_2
			Mobil 1	
			Mixture*	
F-14	January 1983	3	AMS/Oil Synthetic Gear Lube (EP)	FeO_2
DAST	February 1983	3	AMS/Oil Synthetic Gear Lube (EP)	TiO_2
F-104/FTF	March 1983	1	AMS/Oil Synthetic Gear Lube (EP) Mixture*	FeO_2
PIK-20E	April 1983		AMS/Oil Synthetic Gear Lube (EP) Mobil 1	
		4	Mixture*	FeO_2
			Pennzoil (10-40W)	
T-38	May 1983		Exxon Synesstic 32	
		2	Mixture*	FeO_2
			AMS/Oil Synthetic Gear Lube (EP)	
			Mobil 1	

*Mixture of AMS/Oil Para-Synthetic Engine Oil and Mobil (1:1)

The first oil-flow flights in the investigation [122] were conducted with the F-111 TACT/NLF aircraft. For this study Chevron 80W-90 gear oil was mixed with powdered black graphite in a ratio of four parts oil to one part graphite by volume. Flight observations of the oil mixture indicated that at altitudes above 7.6 km (25,000 ft) the mixture no longer responded to the flow field of the wing glove. In reference [122] it is stated that this observation was likely the result of the low temperatures at high altitude causing an increase in the viscosity of the oil mixture. As a consequence, the oil-flow study was conducted at an altitude of 7.6 km (25,000 ft). It was found that between take-off and the time at which the first test condition was established, most of the oil near the wing glove leading edge was moved aft by the airflow. Sufficient oil remained on the wing glove leading edge, however, for boundary layer transition identification during the first 30 min of flight, while the shock wave location was observable during one hour of flight.

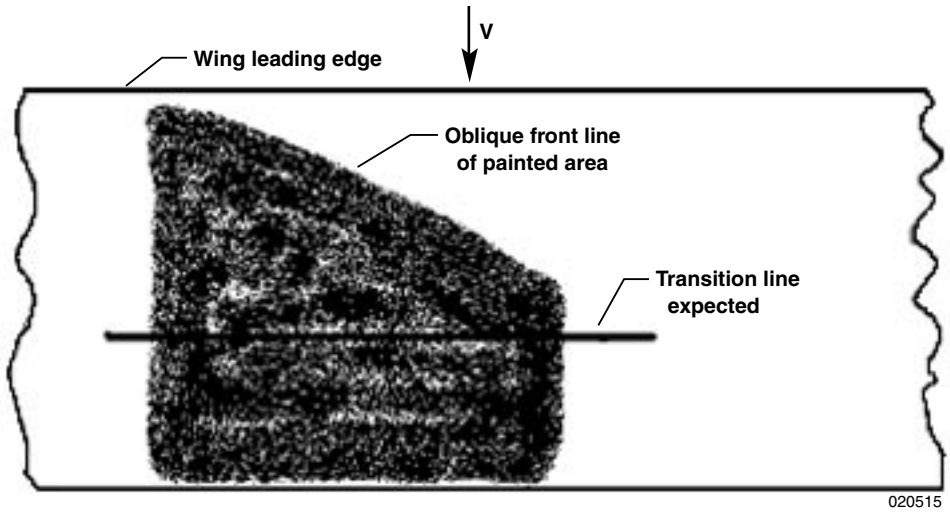

Figure 4.2.9-1. Oblique upstream border of painted area to investigate a possible influence of the paint on the transition process.

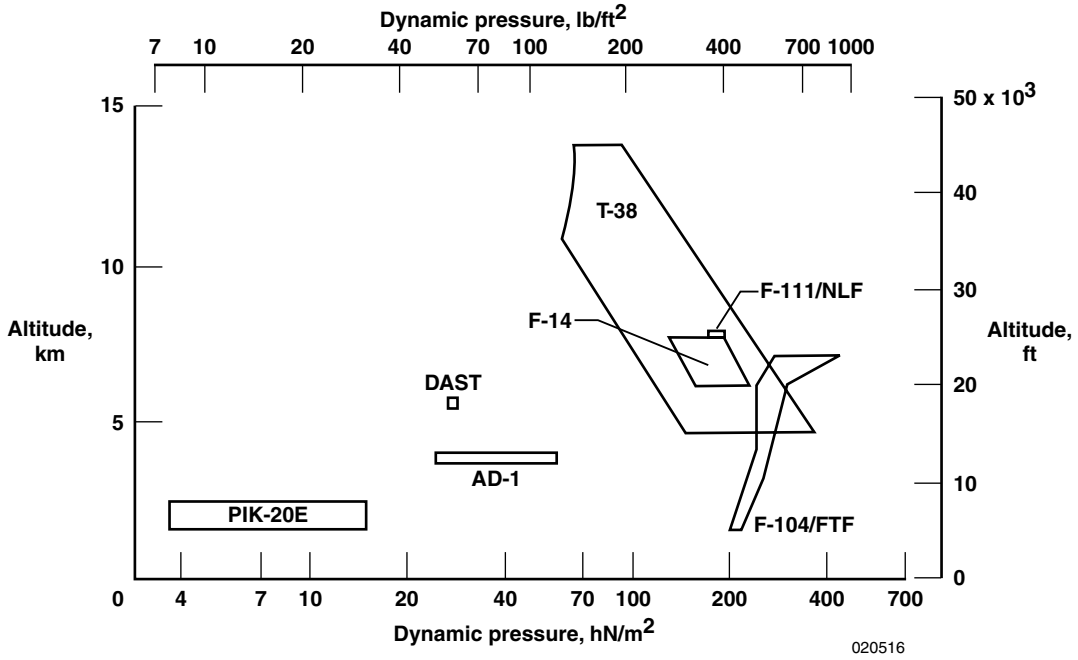

Figure 4.2.9-2. Flight conditions at which oil-flow patterns were photographed. [121]

In the next set of flight tests, which were conducted on the AD-1 aircraft, a different darkening agent, putty black (FeO2), was used in an attempt to provide more contrast between the oil and the wing surface. As part of these flight tests, a mixture of equal parts of Mobil 1 and AMS/Oil Para-Synthetic was compared with Mobil 1. The mixture of Mobil 1 and AMS/Oil responded well to the flow conditions and remained on the wing. This mixture was therefore employed on subsequent flights. In order to investigate the repeatability of the oil-flow patterns, on two flights the order of the flight test points was reversed. It was found that the test point order had no observable effect on the oil flow patterns. A variation of the mixture ratio of oil and putty black in the range from 10 parts oil to 1 part putty black to 20 parts oil to 1 part putty black showed little sensitivity of the oil flow patterns to the mixture ratio. However, a ratio of 15 part oil to 1 part putty black was necessary for good visualization. A photograph from the AD-1 oil flow experiments is shown in figure 4.2.9-3. Highlighted in the figure is the front of natural transition on the port wing and flow separation on the port aileron.

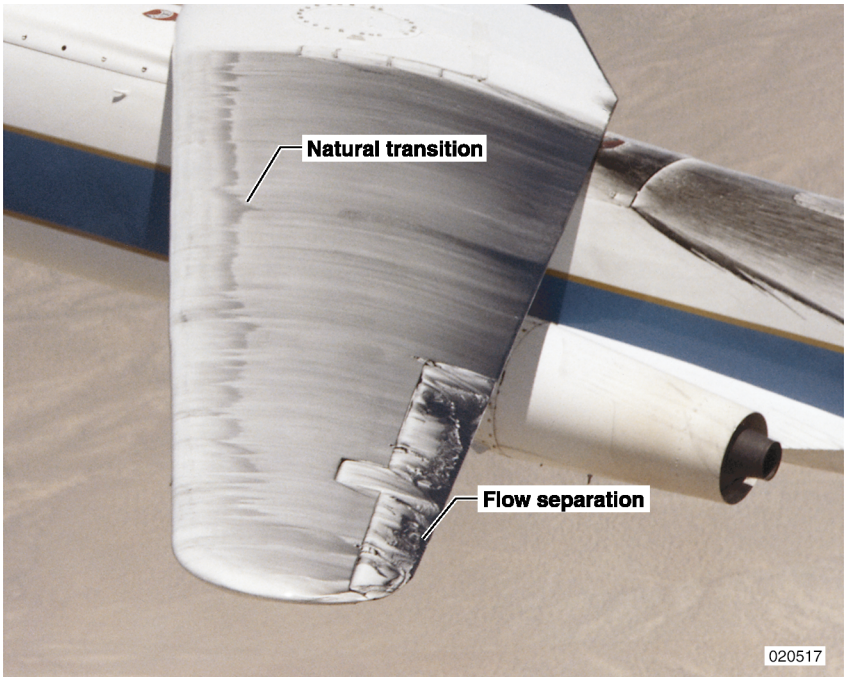

Figure 4.2.9-3. AD-1 oil-flow experiment: Indicated airspeed 45.3 m/sec (87.9 knots), 30° wing sweep. [122]

Low-speed oil-flow visualization flights were undertaken with the PIK-20E motor-glider. Four oil solutions were tested, comprising Mobil 1, Pennzoil 10-40W, AMS/Oil gear lube and a mixture of AMS/Oil Para-Synthetic Engine Oil and Mobil 1 (figure 4.2.9-4). The mixture (mixture ratio 1:1) was found to be the most responsive to the aerodynamic flow field and was successfully used to determine the location of the boundary layer transition front as a function of airspeed. In figure 4.2.9-5(a) the location of the natural boundary layer transition is indicated. Reference marks at intervals of 10 percent and 20 percent of chord length were painted on the wing. On the outboard section of the oil flow test area, a boundary layer trip strip was applied at the 40 percent chord location. The contrast in oil color across the trip strip is seen to be the same as the contrast that occurs at natural transition. At about the midspan of the oil-flow test area, a transition wedge is noted, originating presumably from a surface blemish. Aft of the natural flow transition front, a sharply defined spanwise line can be distinguished. The authors of reference 122 assumed load-depending local waviness or discontinuity as the source of this line. Another interpretation of the image is more likely. It is well known that the PIK-20E airfoil has transition on the upper surface through a laminar separation bubble. Consequently the first line (marked as “Natural transition”) is the laminar separation line and the second line (marked as “Location of interior structure”) indicates the turbulent reattachment. In contrast to this assumption the turbulent reattachment line also exists behind the transition wedge. But this second line also could be a remaining pattern from another test point. The image is a good example to show that a video sequence of the pattern development would help to find a correct interpretation. Figure 4.2.9-5(a) depicts the oil-flow pattern at 60 knots indicated airspeed. At the higher airspeed of 95 knots (figure 4.2.9-5(b)) the laminar separation is shifted slightly downstream and nearly coincides with the turbulent reattachment.

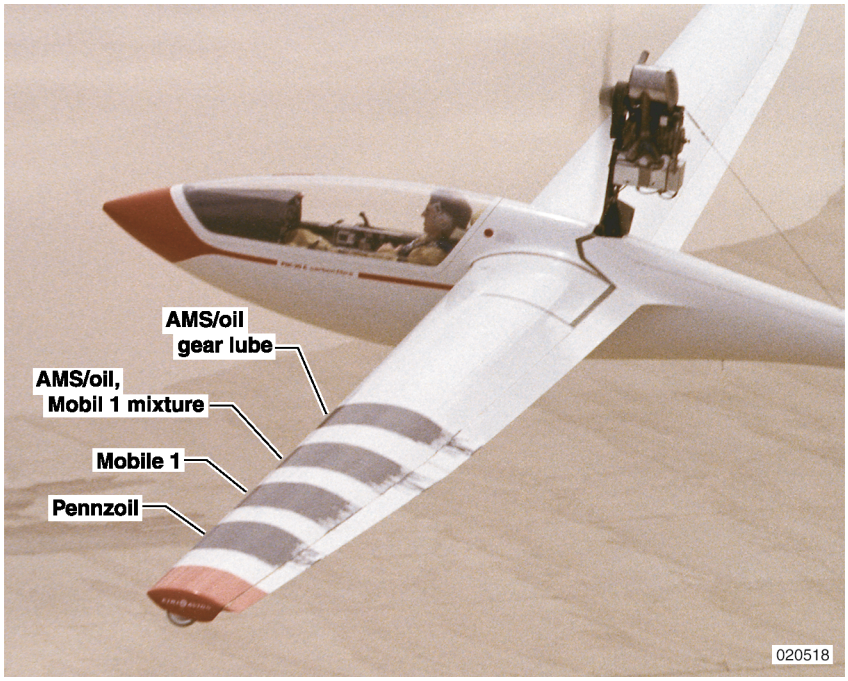

Figure 4.2.9-4. PIK-20E motorized sailplane with oil-flow test samples.

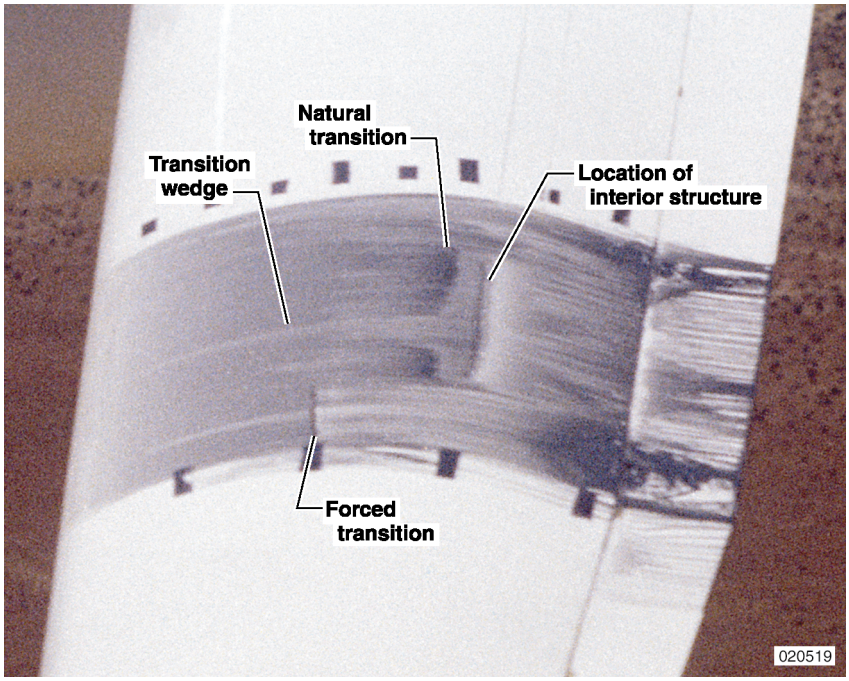

(a) Indicated airspeed 31 m/s (60 knots).

Figure 4.2.9-5. PIK-20E oil-flows.

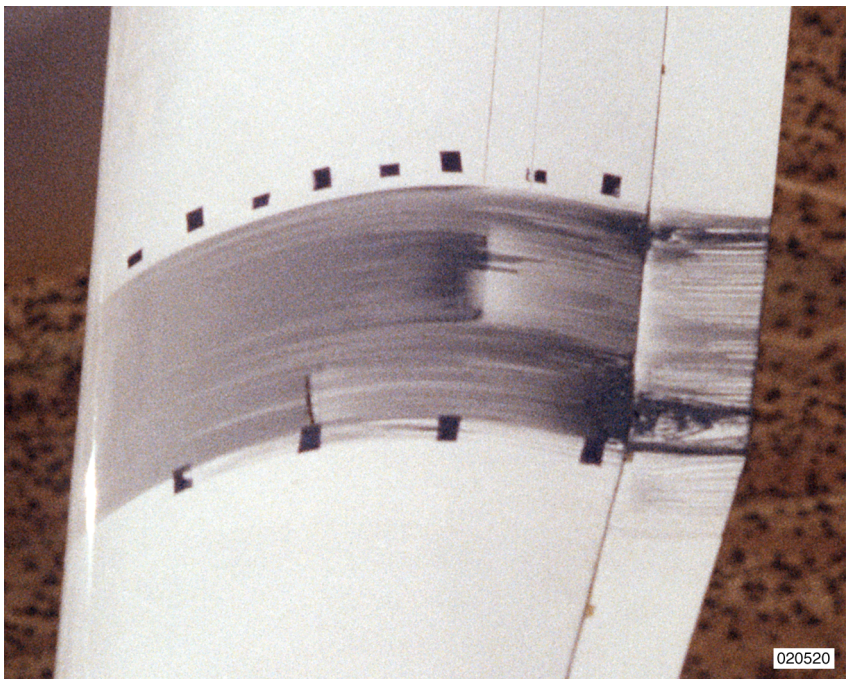

(b) Indicated airspeed 49 m/s (95 knots).

Figure 4.2.9-5. Concluded.

Summarizing, Curry, Meyer, and O'Connor recommend onboard photography as the preferred solution compared with employing a chase aircraft. Concerning the variety of oils tested, a mixture of AMS/Oil Para-Synthetic and Mobil 1 was the most successful solution found. The two oils were mixed in a 1:1 ratio and a pigment was added to provide a contrast with the aircraft surface. When applied to white or aluminium surfaces, ferric oxide (FeO_2), which is commercially available as putty black, was used as a black pigment. One part FeO_2 was mixed with 10 to 15 parts of the oil mixture. A white pigment, titanium dioxide (TiO_2), was employed to improve the contrast with dark surfaces. The titanium dioxide was mixed with oil in about 1:1 ratio. It is important to avoid clumps of undissolved pigment in the oil solution since this can cause premature boundary layer transition. This problem can be overcome by first mixing a small amount of oil solution with the pigment to form a smooth thick paste and then adding the remaining oil solution.

The synthetic oils used in reference 122 were preferred because their viscosity tends to be more constant with respect to temperature variation. For high performance airplanes and conventional oils, in particular, an oil that was responsive at the cold temperatures of high altitude, would be too easily blown off the surface at low altitudes in warm temperatures during take-off and climb. Therefore the goal is to have a somewhat constant viscosity through a wide temperature range.

4.3 Acoustics measurements

4.3.1 Introduction

The stability of laminar boundary layers can be influenced by acoustic noise. In particular, when the frequency of acoustic noise coincides with the frequency range of critical Tollmien-Schlichting (T-S) waves. The wave amplitude growth process may be accelerated, shifting the transition point upstream. The physics of this receptivity problem is not yet fully understood. For flight tests the noise of a propeller or of the fan of a turbofan engine could be strong enough to force the transition process. Thus, the measurement of the noise

and therewith the knowledge of the frequency spectrum of an engine could be helpful in interpreting flow observations.

On the other hand, noise measurements could be used to determine the pressure fluctuations of the Tollmien-Schlichting waves and thus the frequency spectrum of the amplified waves. The noise measurements further allow one to distinguish between T-S waves and those intermittently appearing T-S waves and turbulent spots indicating the transition area. For both cases the measurement techniques are described, and measured examples shown.

The measurements of engine noise reported here were performed during flight tests with the DLR VFW614/ATTAS flight test aircraft (figures 4.2.2-1 to 4.2.2-3) investigating an NLF nacelle [66]. The flight test vehicle and the nacelle are described in reference 69.

4.3.2 ACOUSTIC NOISE MEASUREMENTS ON A NACELLE

In the following, the results obtained with a Kulite transducer microphone installed on the VFW614/ATTAS NLF nacelle are presented. The location of the microphone employed is shown in figure 4.3-1. It was a miniature piezoresistive pressure transducer microphone MIC-062 produced by Kulite. The specified operating temperature range of –55 °C to 120 °C avoided the need for a microphone heater. The microphone was mounted with its protective screen flush with the external surface of the fan cowl. Kulite microphones can tolerate more than one atmosphere pressure differential across their diaphragms, so that the pressure reference tube can be left open inside the nacelle fan cowl. As signal conditioning circuitry for the Kulite transducer microphone, a compact unit, consisting mainly of a voltage regulator and two AD524A instrumentation amplifier chips, was used. This Oxford University development was mounted on the intake barrel of the engine. The Kulite transducer was excited with 15V dc and the output was amplified by the two AD524 amplifiers. Each amplifier had a gain of 10. The first amplifier was ac-coupled to the second. The bandwidth of the Kulite transducer microphone reached up to 100kHz, which exceeded the capabilities of the Oxford University data acquisition system.

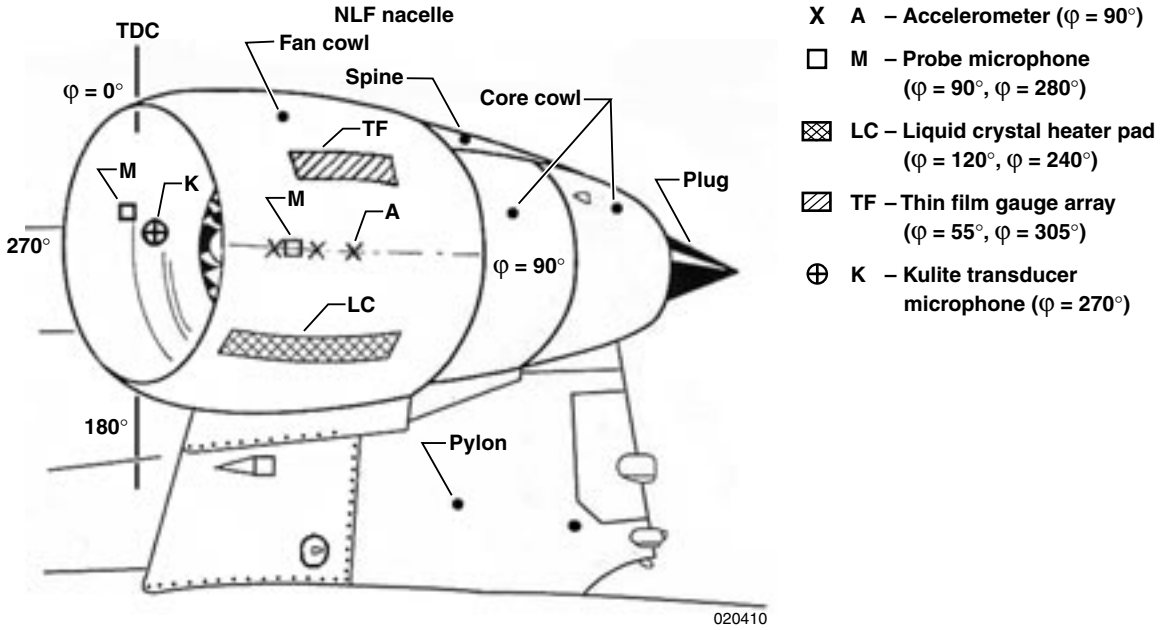

Figure 4.3-1. Survey of the location of measurement equipment on the NLF nacelle fan cowl on the VFW614/ATTAS.

In figure 4.3-2 the power-spectra from the Kulite transducer microphone are shown for comparison for three different operating conditions of the VFW614/ATTAS. Depicted are the results for the cruise condition, descent with the port engine shut down, and windmilling, as well as a condition with the aircraft stationary on the ground with the port engine running at a speed corresponding to that at cruise condition. The figure illustrates the effect of the engine on the noise environment. There is no evidence of discrete frequency components in the trace when the engine was shut down in flight and windmilling. Comparison between the two conditions with the engine running show that the random flow noise found in flight, masks the higher harmonics of the fan blade passing frequency which are observed when the aircraft is stationary on the ground. Thus, the trace for the engine ground run not only shows the spikes for frequencies lower than 10 kHz, but also shows, in ascending order of frequency, spikes of the rotor blade passing frequency of the intermediate pressure compressor at about 10.4 kHz, and the 2nd harmonic (12.9 kHz) as well as the 3rd harmonic (17.2 kHz) of the fan blade passing frequency. Note that the rotor blade passing frequency of the first stage of the high-pressure compressor coincides with the 2nd harmonic of the fan blade passing frequency. The sources for the spike at 14.8 kHz, between those of the 2nd and 3rd harmonic of the fan blade passing frequency, and at 27.1 kHz, could not be identified.

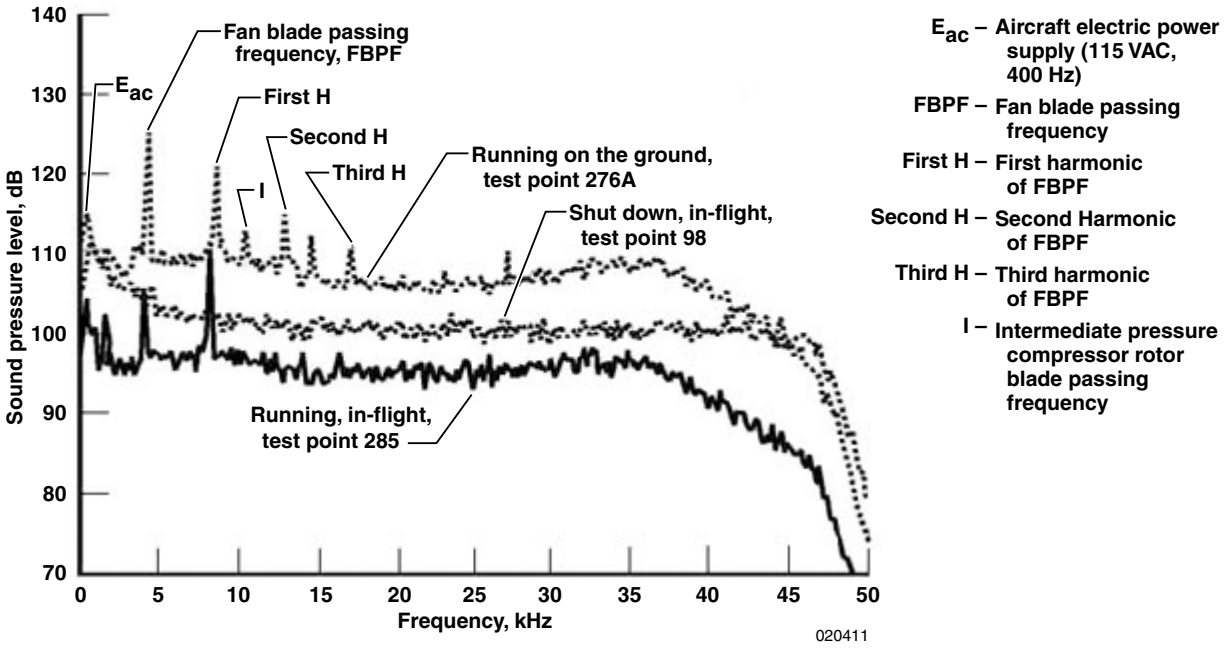

Figure 4.3-2. Sound pressure levels measured by the Kulite transducer microphone on the ATTAS NLF nacelle fan cowl at cruise, port engine shut down, descent, and ground running.

The higher noise level observed during the engine ground run appears to be a result of the effect of the ground as a reflective surface. In addition the absence of an external flow for the convection of acoustic disturbances away from the aircraft may be responsible. The higher level of random noise seen in flight with the engine shut down and windmilling appears to be caused by flow noise resulting from spillage from the engine intake whilst the engine is windmilling. For this flight condition the boundary layer on the external surface of the NLF nacelle fan cowl is fully turbulent a short distance downstream of the highlight. In contrast, for the cruise condition at the location of the pickup point of the Kulite transducer microphone the boundary layer is still laminar, with flow transition occurring in close proximity but downstream of the pickup point. The different transition locations associated with both of the above flight conditions are induced by the different engine mass flows which govern the nacelle pressure distribution and dominate any influence of noise which may possibly exist. Flight tests with a laminar flow glove on the VFW614/ATTAS in the neighborhood of the engine inlet [40] (mentioned in Section 4.2.1) showed no influence at the above discussed conditions on the transition location.

4.3.3 TRANSITION DETECTION BY ACOUSTIC NOISE MEASUREMENTS

Boundary layer transition can be detected using flush-mounted microphones or high-response pressure transducers on a wing or similar surface in flight. On the F-15 10-deg Cone flight experiment [101, 102], Tollmien-Schlichting instabilities were observed in the laminar and transitional boundary layer power-spectral densities at both subsonic and supersonic Mach numbers. Shown in figure 4.3-3 are smoothed PSDs at the same nominal Mach number from several flights. The dominant feature in these cone boundary layer spectra is the peak, which decreases in frequency and increases in power as Re_x increases. Finally, at the location near the end of transition, the peak disappears into the smooth, broadband spectrum characteristic of a turbulent boundary layer.

On sailplanes or general aviation aircraft, boundary layer transition can be detected with a very simple technique using surface-mounted pitot probes connected with small diameter tubing to either a stethoscope or acoustic ear plug for listening.[123, 21] For powered aircraft, ear noise protection is needed over the acoustic ear piece to attenuate the background noise of the engine, propeller, and airstream. If the flow is laminar, at most a gentle rustle or usually nothing can be heard. If the flow is transitioning to turbulent, a lot of little whistles, consisting either of some odd tones or one predominant tone, are typical. The boundary disturbances are beginning to get irregular or they are beginning to build up, and as they pass the end of the tube they make these little noises. In the case of a full transition to turbulent, a very loud roar can be heard.

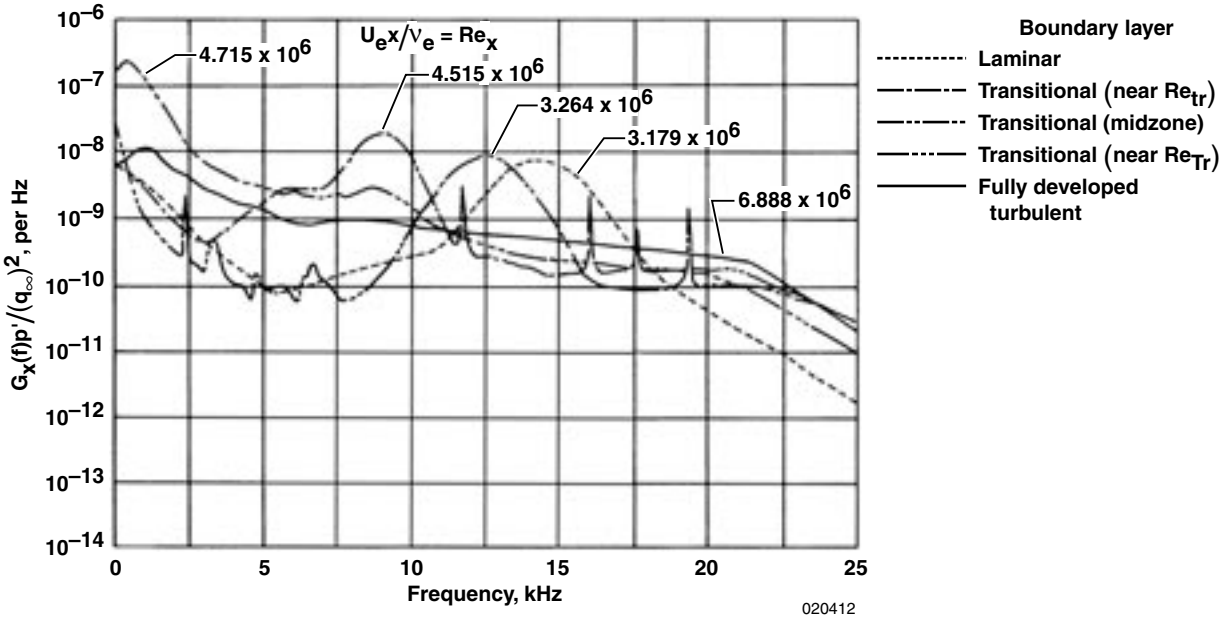

Figure 4.3-3. F-15 10° cone power spectral density distribution, M~0.8 (spectra are smoothed).

4.4 Vibration measurements

4.4.1 Introduction

Vibration of aerodynamic surfaces can affect the laminar flow over such surfaces. It is thus of importance to possess a knowledge of the vibrational environment when performing in-flight investigations concerned with the application of laminar flow technology. One especially significant source of vibration can be that stemming from the power plant in operation.

The instrumentation used and typical results obtained, with reference to the vibrational environment to which engine nacelles are subjected, will be addressed regarding flight tests conducted within the framework of a European collaborative program using the DLR VFW614/ATTAS flight test aircraft. The flight test vehicle and the nacelles flight tested within that program have already been addressed in Section 4.2.2. and Section 4.3.1, respectively.

4.4.2 Nacelle instrumentation for vibration measurements

For assessment of the vibration environment experienced by the boundary layer flow over the fan cowls of the investigated flight test nacelles, single- and three-axis Vibro-Meter CE 506M401 accelerometers were mounted on the inner surface of the fan cowls in a row at radial $\varphi = 90°$, as illustrated in figure 4.3-1. The sensitivity of the accelerometers is 10 mV/g. The specified frequency response of these accelerometers is 7 Hz to 20 Hz ±5 percent with a mounted resonant frequency of 65 kHz nominal and an operating dynamic range of ± 212 *g*. This covers the range of 10 Hz to 20 kHz at a maximum of 100 *g*, which was specified to be the range of interest as regards a possible excitation of Tollmien-Schlichting waves by the vibration of the fan cowl structure.

The output of the accelerometer channels was low-pass filtered using an EXAR XR-1004 general purpose low-pass filter with Bessel characteristic. The roll-off outside the passband provided by this fourth-order-switched capacitor filter type is 24 dB/octave. The corner frequency of the filter response was tuned using an external frequency generator. This tuning provided the adjustment of the corner frequency of the accelerometer filter channels from dc to 20 kHz in parallel by a range switch and a 10-turn precision potentiometer. The corner frequency for the accelerometer measurements could be shown on a digital display.

4.4.3 Results and analysis of vibration measurements

A typical example of data from acceleration measurements evaluated by the University of Oxford [124] is shown in figure 4.4-1 for the NLF nacelle with the aircraft flying at maximum cruise. With the port engine corrected low-pressure rotating assembly speed N_{1C} being $N_{1C} = 95.0$ percent of maximum, the fan blade passing frequency is 5.70 kHz. With reference to figure 4.4-1, two observations can be made. Firstly, the overall level of vibration as recorded appears to be very low and, secondly, there seems to be no evidence of a pronounced vibration spike at the fan blade passing frequency (i.e. at 5.70 kHz). The sources for the spikes other than that at the fan blade passing frequency could not be identified. These observations are in contrast to the results recorded with the engine running on a rigid test bed on the ground. Following [125], single-axle accelerometers on the internal surface of the fan cowl skin at the circumferential positions $\varphi = 0°$, 90°, and 270° respectively, show peak accelerations reaching a maximum value of 38.0 g at 6000 Hz. This frequency is very close to the fan blade passing frequency of 6004.2 Hz when the engine is operated at $N_{1C} = 100$ percent. Furthermore, also for the low-frequency band of 0-500 Hz the peak accelerations observed exceeded those recorded for the maximum cruise flight condition by an order of magnitude. For comparison, figure 4.4-2 shows the power spectrum of a hot-film signal during an engine ground run. The fan blade passing frequency, as well as the first and second harmonic, can clearly be identified; whilst the third to fifth harmonic of the fan blade passing frequency can only be detected from the knowledge of the associated frequencies.

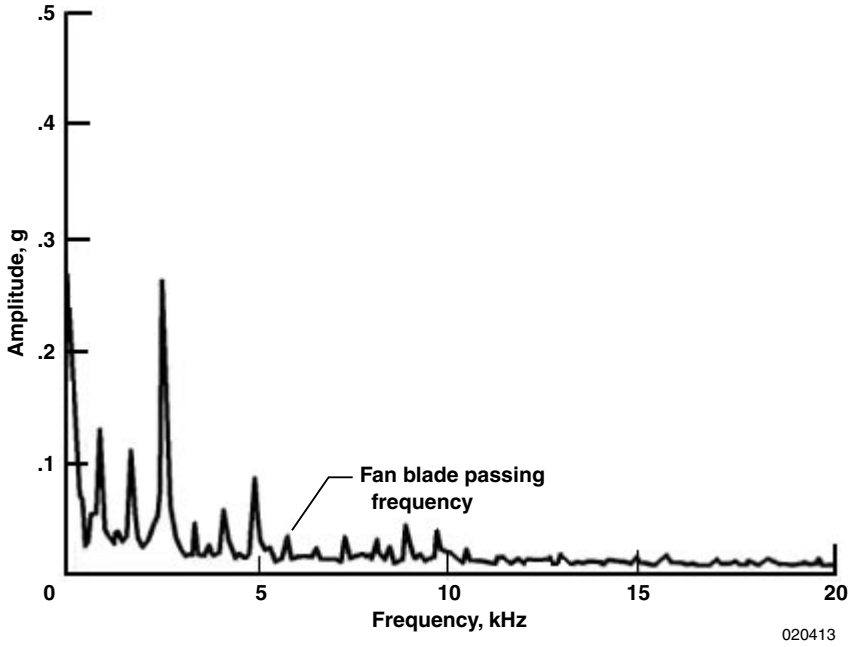

Figure 4.4-1. Vibration amplitudes as function of frequency measured by the accelerometers on the ATTAS NLF nacelle fan cowl at maximum cruise condition.

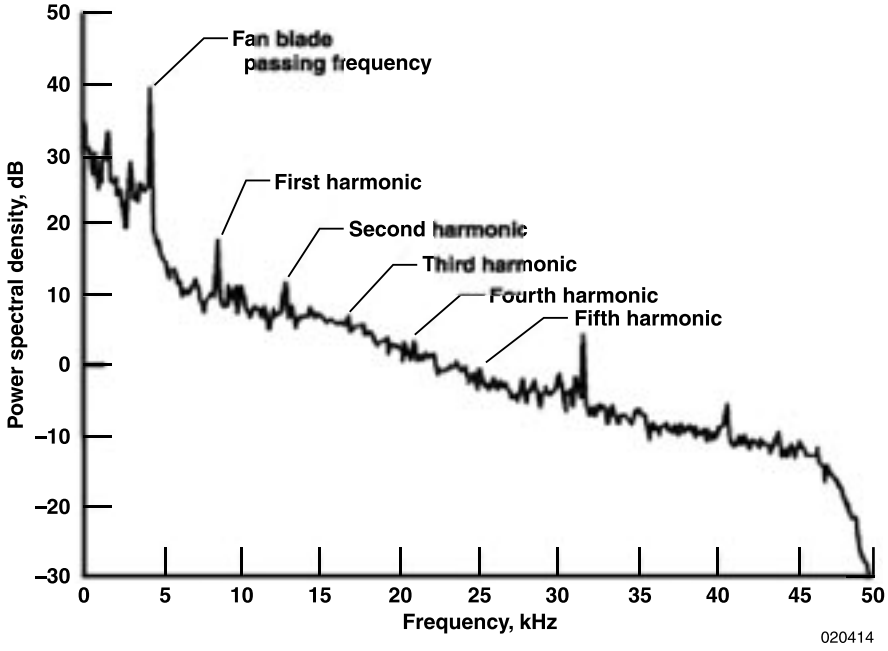

Figure 4.4-2. Power spectrum of a hot-film signal for the NLF nacelle fan cowl during ground run with 69.9 percent of maximum fan speed.

4.4.4 CONCLUSIONS

An investigation of the vibration to which conventional and laminar flow engine nacelle fan cowls are subjected has been conducted within the framework of a European collaborative program employing the DLR VFW614/ATTAS flight test vehicle. Accelerometers mounted on the inner surface of the fan cowl skin show that the overall level of vibration to which the fan cowls were subjected in flight was found to be very low and there was no evidence of a pronounced vibration spike at the fan blade passing frequency. This stands in contrast to observations made for the engine running on a rigid test bed on the ground.

4.5 Atmospheric turbulence measurements

4.5.1 INTRODUCTION

In the application of laminar flow technology to aircraft design, the objective is to maintain laminar boundary layer flow over large areas of the air-washed external surfaces of the airframe such as wing, empennage and engine nacelles. Owing to the sensitivity of laminar boundary layer flow over aerodynamically smooth surfaces to the effects of disturbance like noise, vibration, and insect contamination, as well as the atmospheric conditions; all these aspects of receptivity problems must be taken into account in the aerodynamic design.

As regards atmospheric conditions, one important element of weather phenomena is atmospheric turbulence. A knowledge of this is not only of significance because it is a property of the natural environment in which aircraft operate, but it is also important for progress in numerical simulation when developing CFD codes, as well as for experimental simulation in wind tunnels. Wind tunnel designers strive to achieve in particular, in the development of advanced wind tunnels specifically designed for aerodynamic investigations related to laminar flow technology, a flow quality in wind tunnels for which the turbulence level approaches that which is found in the undisturbed atmosphere.

4.5.2 REQUIREMENTS FOR IN-FLIGHT MEASUREMENTS

Like the flight test measurement techniques for laminar flow in general, the determination of atmospheric turbulence cannot be divorced from the measurement technique used for quantifying this meteorological phenomenon. Thus for the interpretation of results of the in-flight investigations of atmospheric turbulence, it is important to note that atmospheric turbulence is a weather phenomenon, depending entirely on weather conditions prevailing at a certain geographic location at a particular altitude and a certain time of the day. As such, the atmospheric turbulence intensity, assuming it is determined employing an aircraft equipped with an appropriate calibrated sensor mounted on a probe, must be independent of the aircraft used. The aircraft is merely a vehicle for carrying the sensor probe, the sensors usually employed being of the hot-wire or hot-film type. This implies that the probe sensor is installed on the particular aircraft at such a location where the airframe does not cause any significant disturbance of the flow field surrounding the sensor probe compared with the free-stream conditions. A further requirement is that the sensor should not be subjected to vibrations transmitted from the airframe to the sensor probe, as the sensor is not able to differentiate between signals associated with velocity fluctuations of the free-stream and those stemming from mechanical vibrations. In practice this is a requirement that is difficult to fulfill when the aircraft engine or engines are operating.

4.5.3 SURVEY OF IN-FLIGHT INVESTIGATIONS

This overview of the in-flight investigations of atmospheric turbulence covers the spectrum of low to high altitudes and is based essentially on reference [126] which contains further details. The sources are in most cases investigations related to studies of laminar flow technology.

In-flight measurements of the atmospheric turbulence intensity were performed within the framework of a European collaborative program to flight test a natural laminar flow (NLF) nacelle [66, 68]. The flight trials with the NLF nacelle were conducted using the DLR flight test aircraft VFW614/ATTAS. The free-stream turbulence intensity measurements were performed by Oxford University at an altitude range of

$H \approx$ 17600 ft to 21400 ft (5364 m to 6523 m) for flight Mach numbers $Ma_\infty = 0.45$ to $Ma_\infty = 0.57$ ($U_\infty \approx$ 140 m/sec to 177 m/sec).

Previous to the VFW614/ATTAS flight trials the DLR had undertaken some laminar flow investigations using an NLF wing glove on a LFU 205. This flight test aircraft was subsequently employed for the measurement of the free-stream turbulence intensity in the lower atmosphere covering a speed range of U_∞ = 70 kts to 130 kts (U_∞ = 36.0 m/s – 66.9 m/sec). Three categories of turbulence intensity were investigated: (1) still air, (2) weak, uniform turbulence and (3) strong, abrupt turbulence [127].

A collaborative research program of several German universities has concentrated on the investigation of the laminar-turbulent flow transition on an unswept aircraft wing [128]. The program included measurements of the atmospheric turbulence intensity which were performed by the Technical University of Berlin employing the research aircraft G 109B operated by the Technical University of Darmstadt. The aircraft operating speed was U_∞ = 40 m/s (77.8 kts). As part of the joint research program the turbulence intensity on the centerline of the low-speed wind tunnel at the LSTM Erlangen was also investigated. The wind tunnel measurements were performed during flat plate experiments upstream of the plate leading edge at U_∞ = 20 m/sec.

In a collaborative program of DLR and NLR two different laser anemometers, a differential laser Doppler anemometer (LDA) of NLR and a laser-two-focus (L2F) anemometer of DLR, were installed in the Cessna Citation II research aircraft from NLR to demonstrate their capabilities for in-flight flow investigations [129]. The aircraft was operated under various atmospheric conditions, e.g. close to temperature inversion layers, in clouds, and in polluted air of industrial regions, to investigate whether it is possible to make measurements in the atmosphere without artificially seeding the air. In the course of the investigations altitudes up to H = 10000 m (32808 ft) were covered with the speed range extending from U_∞ = 100 kts to 240 kts (U_∞ = 51.4 m/sec – 123.6 m/sec).

In a comprehensive national research program on laminar flow, involving industry and research organizations, a close co-operation of Dassault Aviation with ONERA/CERT planned to demonstrate the feasibility of the laminar flow concept by flight trials and to validate and improve aerodynamic design tools [130]. For the research program a Dassault Falcon 50 was used as a laminar flow flight demonstrator. Turbulence and pressure fluctuation measurements were undertaken covering altitudes from H = 36000 ft (10973 m) to 45000 ft (13716 m) for flight Mach numbers ranging from Ma_∞ = 0.75 to 0.85.

In a NASA research program extending over a number of years, measurements of atmospheric turbulence have been obtained from airplane flights through cumulus clouds and thunderstorms. The key objective was the study of flight conditions and solutions to air traffic control problems caused by these meteorological conditions [131]. Within this program, an F-86 jet airplane was used to measure turbulence in cumulus clouds at altitudes of approximately 15000 ft. Other measurements with jet airplanes were performed in severe turbulence in thunderstorms up to altitudes of 40000 ft. The latter measurements were undertaken during flight operations of the Weather Bureau National Severe Storms Project with aircraft instrumented by NASA and operated by the Air Force. A T-33 airplane was used and an F-106 airplane was flown at high subsonic and low supersonic speeds through storms.

4.5.4 RESULTS OF IN-FLIGHT MEASUREMENTS

In presenting results of atmospheric turbulence measurements, the root-mean-square (RMS) values of the turbulent velocity fluctuations are normalized with the flight velocity, defining the turbulent intensity.

For the hot-wire measurements performed with the VFW614/ATTAS it was found that for the majority of the test points the RMS values of the velocity fluctuations u' were constant. This implies that the turbulent intensity Tu(u') must decrease as the true airspeed U_∞ is increased. This trend must also be true for the flight Mach number Ma_∞ at a particular altitude H, provided the free-stream static temperature T_∞ remains constant. Figure 4.5-1 depicts the turbulence intensity $Tu(u')$ as function of Ma_∞ for a number of test points. For the altitude $H \approx$ 21000 ft it is found that $Tu(u')$ does indeed decrease as Ma_∞ is raised. The test points TP409

and TP424 marked in the figure correspond to a lower altitude $H \approx 17700$ ft where the RMS values of the velocity fluctuations u' were probably slightly larger than at $H \approx 21000$ ft.

Measurements undertaken with the Falcon 50 using a conical hot-film probe are shown in figure 4.5-2 in the form as plotted in reference [130]. There, as a measure of the turbulence fluctuations, the ratio $\overline{(\rho u)}'/\overline{(\rho U_\infty)}$ percent is presented as a function of the flight Mach number Ma_∞ with the altitude H as a parameter. In fact the dependent variable defines the normalized mass flow fluctuations in the streamwise direction. These results were obtained from two flights and indicate that there is no significant effect from flight Mach number and altitude for the flight conditions investigated.

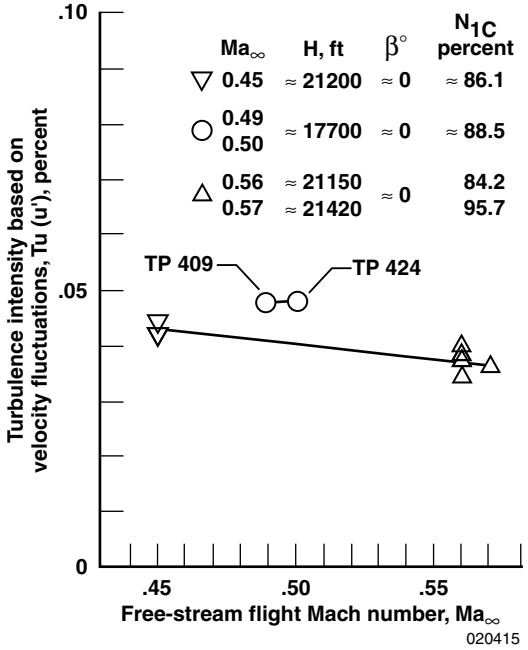

Figure 4.5-1. Atmospheric turbulence intensity $Tu(u')$ as a function of the flight Mach number Ma_∞ measured by a hot-wire probe on the VFW614/ATTAS aircraft.

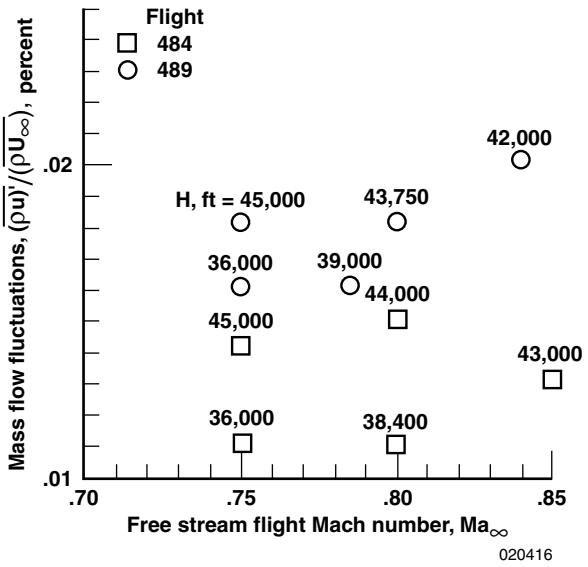

Figure 4.5-2. Atmospheric turbulence expressed in terms of specific mass flow fluctuations $(\rho u)'$ as a function of the flight Mach number Ma_∞ measured by a conical hot film probe on the Falcon 50.

4.5.5 COMPARISON OF TURBULENCE INTENSITY MEASURED IN FLIGHT AND IN WIND TUNNELS

A survey of some results of turbulence intensity measurements in flight and in the test section of wind tunnels is shown in figure 4.5-3. In this figure the turbulence intensity $Tu(u')$ is plotted as a function of the free-stream velocity U_∞. The in-flight results correspond to the turbulence category of still air and were obtained from investigations with the LFU 205, the G109B and the VFW614/ATTAS. It is found that the atmosphere turbulence intensity $Tu(u')$ is below 0.05 percent.

Note that the results for both the LFU 205 and G109B relate to the case where the engine is switched off, while for the VFW614/ATTAS both engines are operating. Also for the VFW614/ATTAS, in the presentation of the turbulence intensity no allowance is made for turbulence intensities encountered at different altitudes, as was done in figure 4.5-1.

For turbulence intensity tested in low-speed wind tunnels, figure 4.5-3 shows, in addition to the results of the LSTM [128] and KKK [132], measurements performed in the test section of the DNW Emmeloord [133]. For the latter, the trend in the variation of $Tu(u')$ with the free-stream velocity is very similar to that of the KKK at the same free-stream static temperature of T_∞ = 295 K. In the free-stream velocity domain of $U_\infty \approx 50$ m/sec both the KKK and DNW exhibit turbulence intensities which are not only comparable with those of the LWK (a laminar flow wind tunnel of the University of Stuttgart) [134], but also with those of flight.

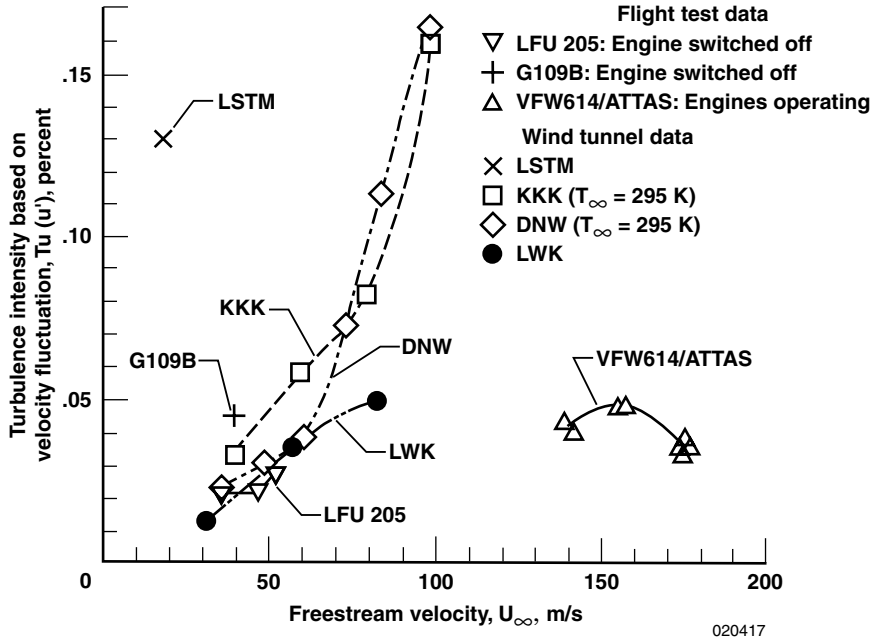

Figure 4.5-3. Comparison of the turbulence intensity $Tu(u')$ from flight test data with wind tunnel measurements.

4.5.6 CONCLUSIONS

Hot-wire in-flight measurements of atmospheric turbulence intensity, which have been performed within the framework of a European collaborative program to flight test a natural laminar flow nacelle using the DLR flight test vehicle VFW614/ATTAS, have yielded the following results:

Under atmospheric conditions defined by the category of still air in an altitude range of $17600 \text{ ft} < H < 21400 \text{ ft}$ and for flight Mach numbers $0.45 < \text{M}a_\infty < 0.57$, which included aircraft operation at maximum cruise, the turbulence intensity was found to lie within the limits $0.034 \text{ percent} < Tu(u') < 0.048 \text{ percent}$.

At a very high-power setting $(N_{1C} = 103 \text{ percent})$, which is close to the maximum allowable, there was evidence of the effect of engine speed resulting in possible airframe vibration being transmitted to the hot-wire probe and causing the measured turbulence intensity to rise to $Tu(u') = 0.0725 \text{ percent}$.

Results of in-flight investigations of the turbulence intensity from other sources in Europe drawn upon for the purpose of comparison and which are likewise associated with the atmospheric condition of still air have also shown $Tu(u')$ to be less than 0.05 percent.

A comparison of the results of the in-flight turbulence intensity measurements with corresponding measurements performed in the test section of some wind tunnels leads to the conclusion that in these wind tunnels the values of freestream turbulence intensity as low as $Tu(u') = 0.05 \text{ percent}$ are only attainable in the low-speed regime $(U_\infty = 50 \text{ m/sec})$.

In general the measurements with hot-wire and hot-film probes for atmospheric conditions of still air reveal the limitations of the instrumentation resulting from the low signal-to-noise ratio experienced under these atmospheric conditions. In particular, the VFW614/ATTAS measurements indicate that the actual level of the turbulence intensity may be lower than the present range of $0.034 \text{ percent} < Tu(u') < 0.048 \text{ percent}$, if interference effects from unknown sources influencing the measurements can be eliminated.

In-flight investigations of the still air turbulence using an X-wire mounted on a G109B motor glider have yielded the following result for this category of atmospheric turbulence at a true airspeed of $U_\infty = 40 \text{ m/sec}$ the components of turbulence intensity were found to be $Tu(u') = 0.045 \text{ percent}$ and $Tu(v') = 0.038 \text{ percent}$, indicating the approximately isotropic character of the atmospheric turbulence. For these measurements, the engine was switched off and the propeller stationary.

Hot-wire measurements performed using an LFU 205 light aircraft have shown that underneath cumulus clouds with the engine switched off and the propeller stationary at a true airspeed of $U_\infty = 40 \text{ m/sec}$ turbulence intensities of up to $Tu(u') = 1.0 \text{ percent}$ were encountered.

Laser anemometer measurements of the atmospheric turbulence intensity have been undertaken as part of an investigation to assess the capabilities of two different laser anemometers in flight employing a Cessna Citation II twin turbofan executive transport. One laser anemometer system was a laser-two-focus (L2F), while the other was a laser Doppler anemometer (LDA). For a representative indicated airspeed of $U_{\text{IAS}} = 92.7 \text{ m/sec}$ it was observed that underneath an inversion layer the turbulence intensity had a value of $Tu(u') = 1.0 \text{ percent}$ using the L2F anemometer and in cumulus clouds the LDA anemometer yielded $Tu(u') = 3.5 \text{ percent}$.

Conical hot-film probe measurements of Dassault Aviation and ONERA/CERT undertaken using the Falcon 50 have shown that for flight Mach numbers ranging from $Ma = 0.75$ to 0.85 and covering altitudes from $H = 36000$ ft (10973 m) to 45000 ft (13716 m) the normalized mass flow fluctuations $\overline{(\rho u)'}/\overline{(\rho U_w)}$ lie between 0.01 percent and 0.02 percent.

In a NASA research program and the Weather Bureau National Severe Storms Project of the United States, measurements of atmospheric turbulence have been obtained from airplane flights through cumulus clouds and thunderstorms. Aircraft employed ranged from T-33 and F-86 to the F-106. It was observed that the internal structure of thunderstorms may be irregular and strongly cellular, but this structure can also exhibit relatively weak components of true gust velocity with no cellular development. Power-spectra were found to have the same shape for different weather conditions ranging from clear air and cumulus cloud to thunderstorms. Associated typical root-mean-square gust velocities σ, a measure of turbulence intensity, are 3.48 ft/s (1.05 m/s) for clear air, 6.14 ft/s (1.87 m/s) for cumulus clouds and 13.77 ft/s (4.20 m/s) for thunderstorms.

4.6 Atmospheric particulate instrumentation

R.E. Davis, NASA Langley Research Center, Hampton, VA USA

4.6.1 Background

Experience with the U.S. Air Force (USAF) Laminar Flow Control (LFC)-configured X-21A aircraft in the early 1960s [14, 135] showed that the extent of laminar flow (LF) was severely degraded while penetrating clouds, and was partially degraded while penetrating light cirrus “haze” conditions, even in conditions where the horizontal visibility was as much as 50 miles. Therefore, all subsequent LF airborne research programs have been conducted with the realization that LF loss in cloud and other particulate concentrations could occur. The aim in this section is to describe the particle-related instrumentation that has been used in several of these airborne research programs. Broadly, this instrumentation consists of two types—that which merely indicates the presence of particles, and that which measures the *particle spectrum* (number concentration and size). The principle of operation of these instruments, details on their construction, and their application to eight LF aircraft research programs from 1960 through 1996 conducted by the U. S. Air Force, the NASA Langley Research Center (LaRC), the NASA Dryden Flight Research Center (DFRC), and industry are described in this section.

4.6.2 Particulate instrumentation

Three types of cloud particle environment instrumentation have been flown in support of airborne LF investigations to date, as follows:

- particle replicator
- charge-patch
- laser particle spectrometer (Knollenberg probe)

Experience in flying this instrumentation on LF-related and other aircraft programs spans the years 1960-1996. Eight different research aircraft are summarized in Table 4.6 below.

Table 4.6. History of Cloud Particle Instrumentation of LF Research Aircraft

Aircraft	Years	Program	Replicator	Charge Patch	Knollenberg probe	References
X-21A	1960-1965	LFC	X	X		14, 135
F-106B	1982	Storm Hazards		X		140
JetStar	1983-1987	LEFT		X	X	143
F-14	1986-1987	VSTFE		X		36
B-757	1990-1991	HLFC		X	X	147
A300B2	1992	HLFC Nacelle		X		148
F-16XL	1996	Supersonic LFC		X		N/A
Learjet	1982-92	NLF/Field Mill		X		149, 150

*Detail on the representative particle instrumentation and results is given later in the "Operational Experience" section. Other examples can be found in the table references.

4.6.2.1 X-21A particle instrument suite

The X-21A program was the first to fly cloud particle instrumentation for LF research diagnostics. This instrumentation consisted of a replicator [135] for capturing samples of the cloud particles in a gel on a moving piece of film, and a system for monitoring the electric charge on the aircraft. The X-21A particle instrumentation suite was pioneering, in that all particle instrumentation used on every subsequent LF program to date has made use of the same measurement principles used on the X-21A- i.e. either a measurement of the ambient particle spectrum (particle size and concentration), or a measurement of the charge state of the aircraft. The charge state was shown to be related to the ambient particle environment. The improvements in particle-measurement capability in the years since the X-21A program include the development of particle spectrometers for making real-time particle spectra measurements, and the ability to increase the sensitivity of measurements that gauge the charge state of the aircraft.

4.6.2.2 Particle replicator

The replicator works [135] by exposing a 16mm continuous Mylar film loop to impingement by cloud particles contained in the ambient airflow. The film loop is continually re-coated with a quick-drying Formvar thermoplastic resin. The cloud particles (cloud droplets and ice crystals) impact the coated film. The film loop is then heated to evaporate the solvents in the resin, and the result is a mold (replica) of the impacted particles. The Mylar film is then fed into an optical magnification system, so that the particle replicas can be viewed during flight. Data reduction on the ground consists of counting, sizing, and photographing the particle collections of interest to derive the ambient particle spectrum. Thus, the replicator was not a real-time instrument, and could only provide snapshots of the particle environment (particle size and concentration). However, the replicator readings were very useful in validating Hall's theory for the X-21A. The only LF application of the replicator to date occurred on the X-21A program. It has been supplanted in the subsequent LF investigations by the laser particle spectrometer, discussed later.

4.6.2.3 Charge-patch

As an aircraft encounters atmospheric particles—whether aerosols, volcanic dust, raindrops, or ice crystals—its airframe becomes charged instantaneously by a triboelectric (frictional charge transfer) effect generated by the impact of particles on the aircraft. A detailed description of the charging and discharging phenomena associated with aircraft is given in reference [136]. The particle impact-charge dependence is a very complex phenomenon, and has not yet been completely described analytically. Nevertheless, by electrically isolating part of the airframe as a "charge-patch," the level of charging current on the patch may be monitored. The current level is related to the ambient particle concentration which may, in turn, be related empirically to the amount of LF loss. Thus, the patch reading may be used as a simple empirical indicator of

the LF suitability/non-suitability of the dynamic ambient particle environment for an LF-configured aircraft. The LF application is an extension of the original purpose of charge patches, which were originally flown to conduct research on aircraft electrification. Such research has been carried out in the U.S. [137], the former Soviet Union [136], and France [138]. The research in reference [138] showed that the aircraft charge could be directly related to the ambient particle environment, if external electric fields from cloud charge centers were not present. Where such cloud charge centers are present, the aircraft charge state depends on both the externally applied field and the triboelectric charging. Interest in aircraft charging continues, mainly because the charging characteristics of aircraft with composite structures need to be understood [139]. LaRC refined the charge-patch concept for LFC aircraft application, mainly by increasing its sensitivity to tenuous cloud particle concentrations, and using improved fabrication methods [140].

The main advantage of the charge-patch for LF research is that it is a simple, inexpensive, easy-to-read instrument which provides an instantaneous indication that particles are present. However, it is an empirical device, and charge readings have to be related to degree of LF loss through calibrated measurements for each LF aircraft platform application, in order for the readings to be useful as an LF-loss diagnostic. Nevertheless, charge-patches have come to be regarded as a useful diagnostic tool, and have been used on all eight aircraft programs listed in Table 4.6. However, a patch provides no details on particle concentration spectra, and is thus not of use, e.g., for validating Hall's theory.

No details were available regarding the charge-measurement system flown on the X-21A, so a system patterned after the charge-patch technique [137] used by the Stanford Research Institute to investigate precipitation charging of aircraft was developed at LaRC, refined in laboratory bench testing, and fitted to the leading edge of the vertical stabilizer of the NASA F-106B Storm Hazards research airplane in a piggyback test of the charge-patch concept.

The LaRC charge-patch system consists of three major components: (1) an aluminum charge-patch electrically isolated from the rest of the airplane by fiberglass cloth and silicon rubber sealant, (2) a two-channel charge-rate amplifier, and (3) a surge arrestor. Figure 4.6-1 shows the charge patch mounted on the JetStar aircraft.

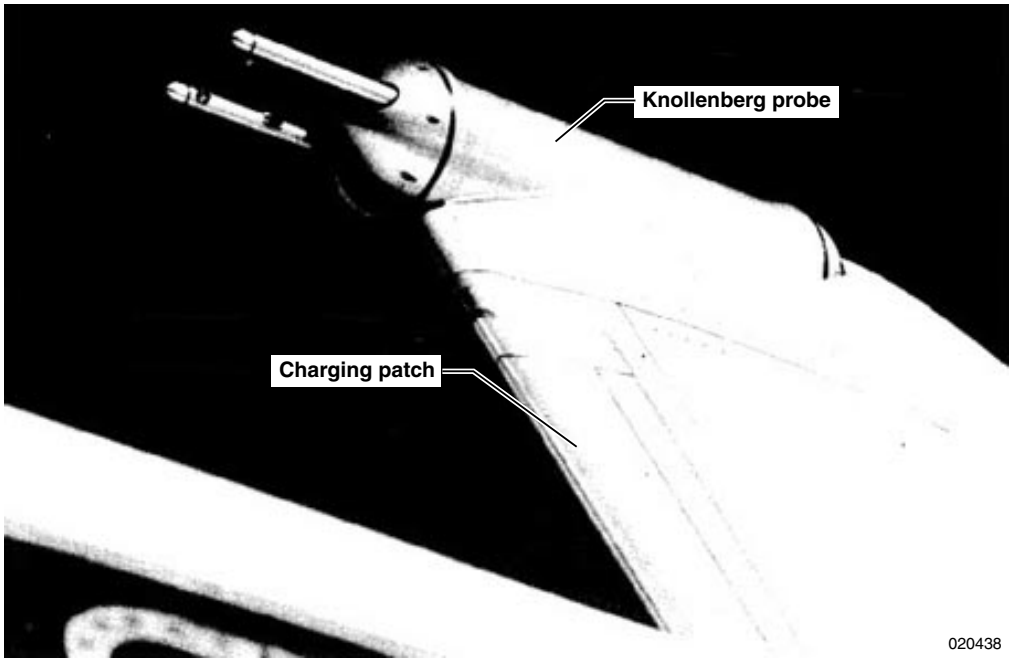

Figure 4.6-1. Cloud particle detection on JetStar pylon.

4.6.2.4 Charge-patch fabrication

The charge-patch developed for the F-106B was fabricated and affixed to the aircraft using a detailed empirically developed fabrication technique. This approach was found to be highly successful, so the patches used in the subsequent LF investigations were constructed in the same manner. Therefore, the fabrication techniques are described here in some detail.

The F-106B patch was constructed from a 15 cm (6 in,) x 92 cm (36 in) piece of 0.02 cm (0.016 in.) - thick #2024 aluminum, and bent to conform to the leading edge of the vertical stabilizer. The patch was electrically isolated from the fin by a 5-7 mil fiberglass cloth insulator impregnated with RTV # 560 silicon rubber insulating material.

The patch-insulator combination was bonded to the fin using a detailed vacuum-bonding technique lasting over 16 hours. (For details, please contact the author). Because of the shape of the vertical stabilizer, the net frontal area of the patch was approximately 456 cm^2 (0.5 ft^2). To eliminate a problem of leading edge erosion and the possibility of the patch tearing away from the aircraft in the intense rainfall environment within thunderstorms, a 6-in patch of #2024 aluminum was riveted to the lower edge of the fin to overlap the lowest 2 inches of the patch. This patch was insulated from the charge patch by fiberglass cloth and RTV #560.

The choice of the #2024 aluminum and RTV #560 materials combination was arrived at through early flight trials and empirical bench testing. Several material combinations were tried, then rejected, either because of some tendency to maintain a residual charge, or to having too long a current-discharge time constant. Among the materials rejected was stainless steel, originally chosen for its durability, but then rejected as a result of its interaction with another insulating agent which caused a residual charge to be maintained. It must be emphasized that the #2024 aluminum and RTV #560 combination was arrived at empirically, making use of materials that were readily available. A thorough theoretical materials science-based investigation to identify the best materials for the task was never performed, and is recommended before charge patches are developed for production LF aircraft. However, because of its success in the F-106B and JetStar programs, the #2024 aluminum and RTV #560 combination was adopted as the best interim combination for subsequent charge patch applications on the other LF aircraft investigations discussed in this report.

4.6.2.5 Charge-rate amplifier and surge arrestor

Figure 4.6-2 is a schematic of the charge-rate amplifier. In order to provide a wide input dynamic range and to allow for ranging to suit the flight environment, the amplifier was designed so that the input transimpedance (current-to-voltage) amplifier had two separate, gain-adjustable output channels. The input to the amplifier is protected by a surge arrestor and a bipolar zener diode network to prevent damage, either by direct lightning strikes or from other electrical discharges that could result from high potential differences between the patch and the aircraft. A similar zener diode network in the output circuitry limits the magnitude of the signals going to the aircraft pulse code modulation (PCM) data recording system. To prevent aliasing errors in the PCM system, active filters having a passband of 0 to 5 Hz were also included. In addition, to preclude radio frequency interference (RFI), all power input and signal connections were made through radio frequency interference filter connectors.

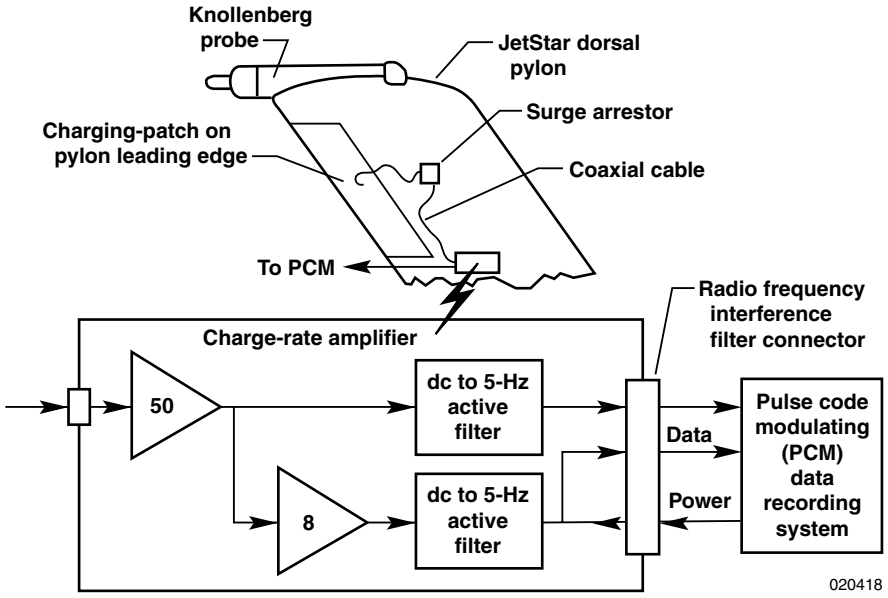

Figure 4.6-2. Charge-rate amplifier electronic schematic.

4.6.2.6 Signal magnitudes

The charge-patch was installed piggyback on the F-106B as a developmental experiment to verify patch function and gain data on optimal amplifier settings for the subsequent LEFT experiment on a Lockheed JetStar. For the first twelve F-106B missions flown at LaRC with the patch onboard, the amplifier gain was set to provide full-scale sensitivities of 25 μA (coarse-sensitivity channel) and ±1 μA (fine-sensitivity channel). The thunderstorm-penetration missions successfully demonstrated the feasibility of the device; charge currents exceeding 25 μA were obtained during flight in heavy rain and thunderclouds, but detection of thin cirrus clouds was less obvious. Therefore, to detect light cirrus, the sensitivity of both channels was increased to ±2 and ±0.25 μA, respectively. A dedicated cirrus-penetration mission was flown as mission 13. Results for this dedicated mission are shown in figure 4.6-3. Encounters with both regular and very thin cirrus are shown to be reliably detected. This mission demonstrated that the patch instrumentation and settings were ready for application to the JetStar in the LEFT experiment. The charge-patch remained on the F-106B aircraft for the rest of its operational career, and recorded data from a wide range of cloud and precipitation encounters in the vicinity of thunderstorms.

The patch fabrication procedures and amplifier gain settings developed for the F-106B were used as the pattern for all subsequent patch fabrications and LF flight experiments with other aircraft. The charge-rate amplifier and surge arrestor electronics box was identical in all the applications. In fact, the same amplifier boxes were used on a succession of the LF research aircraft, being transferred from one aircraft to another over several years time.

One caution must be noted. The charging patch did not return useful data during afterburning operations, presumably because of the large number of ions generated. (This problem was also observed with patch data on the F-16XL operations, discussed later).

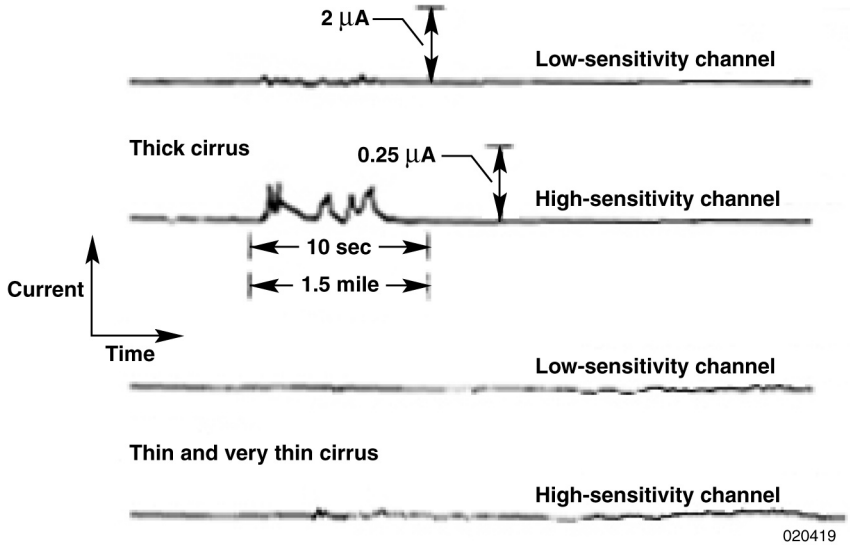

Figure 4.6.3. Reading from a "charge-patch" in thick and thin cirrus penetrations.

4.6.2.7 Laser particle spectrometer

Laser particle spectrometers (Knollenberg probes) were developed in the mid 1970s by Dr. R. Knollenberg of Particle Measuring Systems, Inc. (PMS) for airborne cloud investigations. These are regarded as a modern, real-time cloud-particle-measurement counterpart of the particle replicator discussed earlier. Motivation for applying these probes to LF studies was given by their successful application by the USAF in its Cirrus Particle Distribution Study during the late 1970s e.g., [141, 142]. This study used three types of Knollenberg probes to study a wide range of particle sizes. (The USAF need was to determine the cirrus cloud ice particle environment as an aid in predicting ICBM nose cone erosion in cirrus cloud penetrations.) Knollenberg probes have been used in two LF research programs to date—on a Lockheed JetStar in the LEFT program, and on a Boeing 757 in The Boeing/NASA/USAF/ HLFC program.

The principle of operation of the Knollenberg probe is shown in figure 4.6-4. In part a of the figure, a He-Ne laser provides an illumination source. A cloud particle in the ambient free-stream is shown traversing the laser beam in the object space of the probe. The shadow of the particle is imaged by the probe optical system on a linear photodiode array lying in the probe image plane. The particle shadow momentarily occults a number of the array elements, depending on the particle size. The probe electronics "follow" the particle shadow as it travels along the image plane. For the probe used on the JetStar (PMS, Inc. Model OAP [Optical Array Probe]-230X), the effective size resolution of the optical system was 20 mm, and the particles were sized into thirty 20-mm size bins between 20 and 600 mm. Because the array is one-dimensional, only the effective cross-sectional width of the particle is sampled. (Note that two-dimensional probe models do exist, but their expense was deemed prohibitive for the JetStar LEFT application). Part (b) of the figure shows the arrangement of the laser, optics, and photodiode array within the probe envelope. Part (c) of the figure shows the OAP-230X probe in its housing. The probe is 30 in. in length, and weighs about 45 lb. It requires 60 W of 115-V, 400 Hz power for its operation, and 70 W of 28-V dc power for its de-icing system.

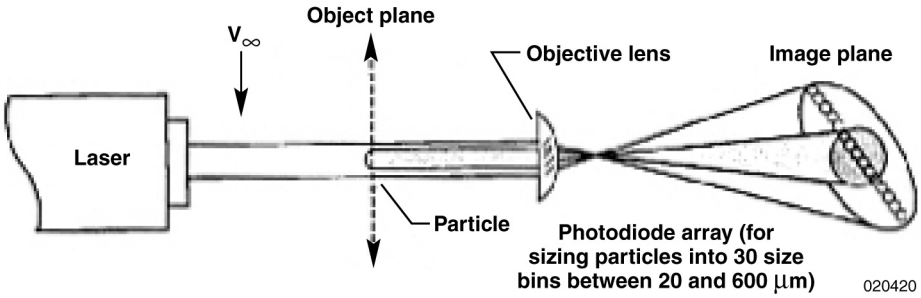

(a) Principle of operation.

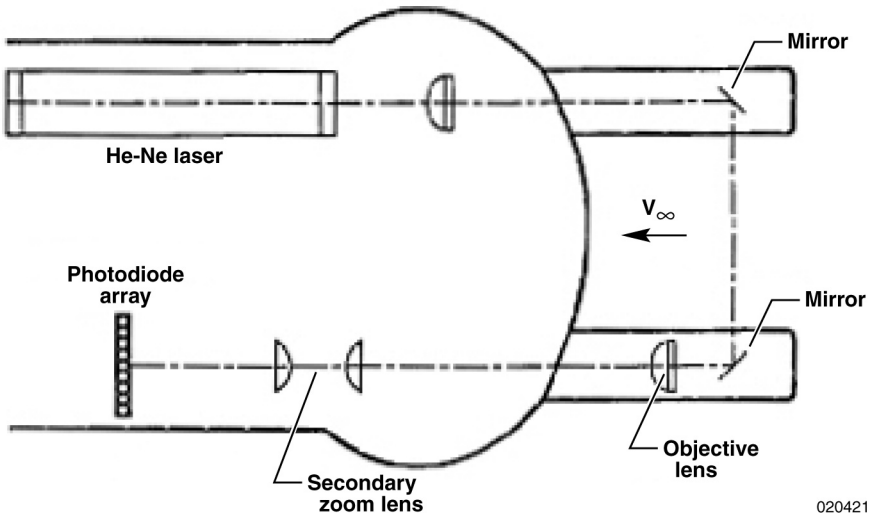

(b) Probe optical system.

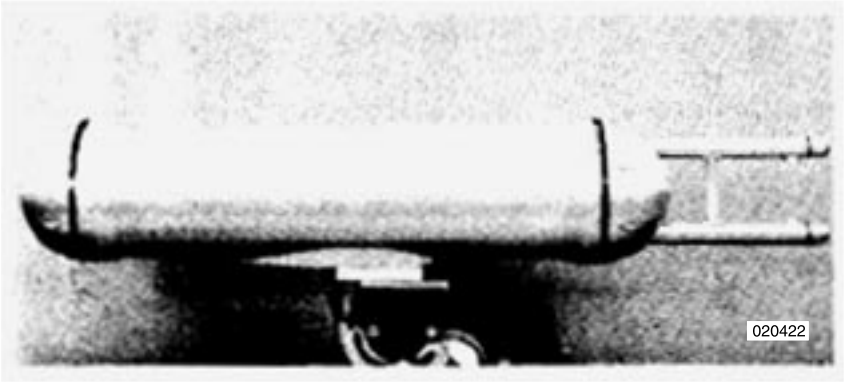

(c) Probe in housing.

Figure 4.6-4. Optical array spectrometer (Knollenberg probe).

The output of the probe is fed to an onboard data system. An accumulating memory is provided so that the number of particles encountered in each size channel during a specified time interval is recorded, along with various other system outputs such as time code, on magnetic tape. For correlation with the dynamic real-time LF readings and charge-patch measurements (if available), the difference in the accumulating count is calculated at 1-second intervals. These difference counts are then scaled to the ambient particle spectra, as shown in figure 4.6-5. The inferred spectra may then be correlated with the concurrent amount of LF present and used in trying to validate theories of LF loss, such as Hall's LF loss criterion. Equations used in the JetStar program for scaling the particle counts in each size channel are presented in Reference [143].

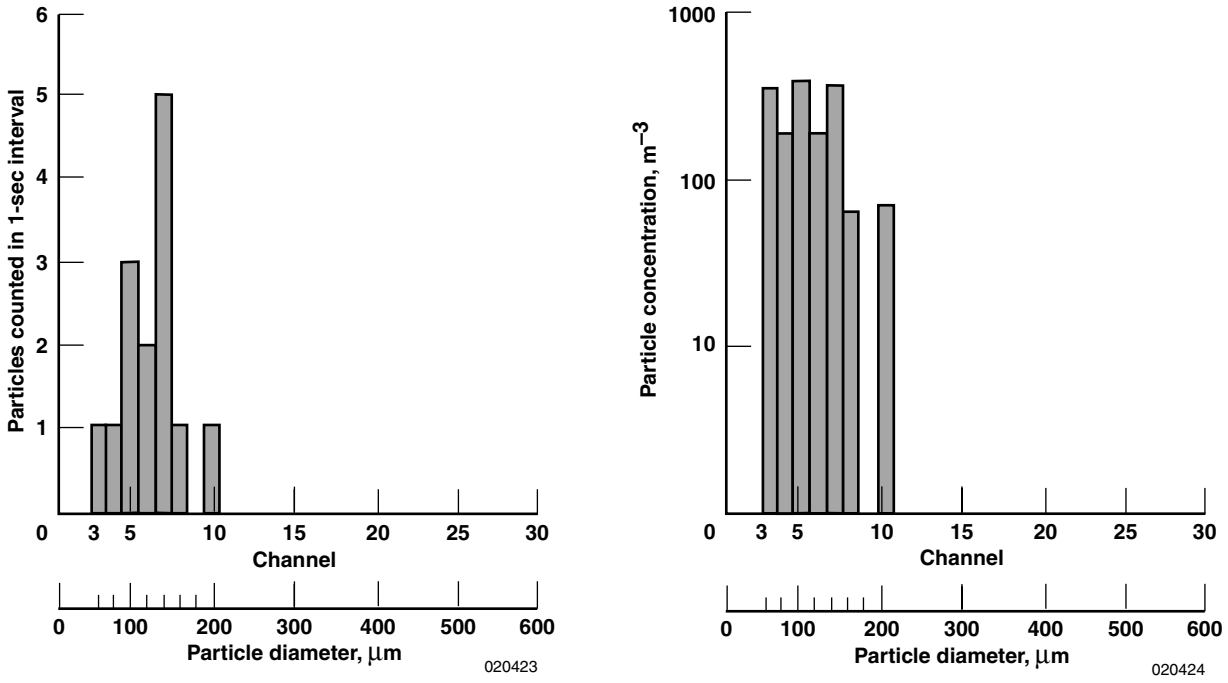

(a) Particle counts at 15:54:30.

(b) Particle concentration computed from 4.5-6(a).

Figure 4.6-5. Example of conversion of particle counts to concentration.

4.6.3 OPERATIONAL EXPERIENCE (REPRESENTATIVE)

Experience with the cloud-particle instrumentation on each of eight LF applications is described below briefly in chronological order.

4.6.3.1 X-21A LFC research aircraft (1960s)

Experience with the X-21A with its charging system and particle replicator has already been related above. Details of the replicator operation may be found in reference [135].

Laminar flow experiments languished for several years until the OPEC oil embargo of 1973, when fuel prices increased markedly. In response to the fuel crisis, NASA initiated efforts in 1976 to take a fresh look at LFC for drag reduction as one element in its Aircraft Energy Efficiency (ACEE) Program to develop new technology for fuel-efficient commercial transports [144]. It was realized that the most difficult problems in achieving LF on commercial transports were associated with the leading edge region. Therefore, NASA conceived the Leading-Edge Flight Test (LEFT) Program [145, 146]—a flight program to test the effectiveness of LFC systems developed with modern technology and evaluate their reliability and maintainability in simulated airline service use. The LFC technology was implemented in two leading-edge test articles mounted on a DFRF Lockheed JetStar aircraft [25].

LaRC became involved in the early 1980s in devising instrumentation to measure the cloud and haze particle environment for LF aircraft during the planning for the JetStar LEFT experiment. It was decided to build on the pioneering X-21A cloud instrumentation experience by flying a “charge-patch” to measure the state of charging of the aircraft, but also to take advantage of the availability of the recently developed Knollenberg probes described above. The Knollenberg probes would be flown in place of the particle replicator flown on the X-21A. This approach led to the promise of being able to correlate (for the first time) the degree of LF present with simultaneous real-time spectrometer measurements of the dynamic particle spectra, as well as with the real-time dynamic nature of the charging of the aircraft.

4.6.3.2 JetStar LEFT program (1982-1986)

To our knowledge, the joint LaRC/DFRC Leading-Edge Flight Test (LEFT) program has provided the most comprehensive evaluation of cloud-particle instrumentation in LF application to date. The basic goal of the LEFT program was to gain operational experience on the performance of laminar flow leading-edge test articles in simulated airline service. Cloud instrumentation on these flights comprised a charge patch and a Particle Measuring Systems Inc. Model OAP- 230X Laser Particle Spectrometer. Both instruments were mounted on a dorsal pylon on the DFRC JetStar (Fig. 4.6-1). (This pylon was originally mounted to conduct propfan tests. The charge patch was riveted to a spare leading edge panel of the pylon, rather than bonded to it as in all the other applications, so that the pylon could be restored quickly to its baseline configuration at the end of the LEFT program.) The LEFT flights simulated actual airline route experience. Most importantly, no efforts were made to avoid clouds on the simulated airline flights, so an appreciable amount time was spent within cloud particle concentrations. Significant cloud encounters were obtained on 41 of the 62 flights in the program. The extent of LF was determined by pitot probes. These cloud encounters provided much data for evaluating both cloud instruments. Reference [143] gives a full account of this evaluation. In summary, it was found that both instruments gave reliable indication of cloud encounter, and—most importantly—it was concluded that the charge-patch could probably be used as a reliable stand-alone instrument. The Laser Particle Spectrometer data was sufficient to perform a partial validation of the Hall Criteria for LF loss. (A full chord Hall Criteria validation was not possible because the laminar flow test articles in this program were designed to provide laminar flow back to only 13 percent chord). Figure 4.6-6 shows simultaneous patch, probe, and LF traces.

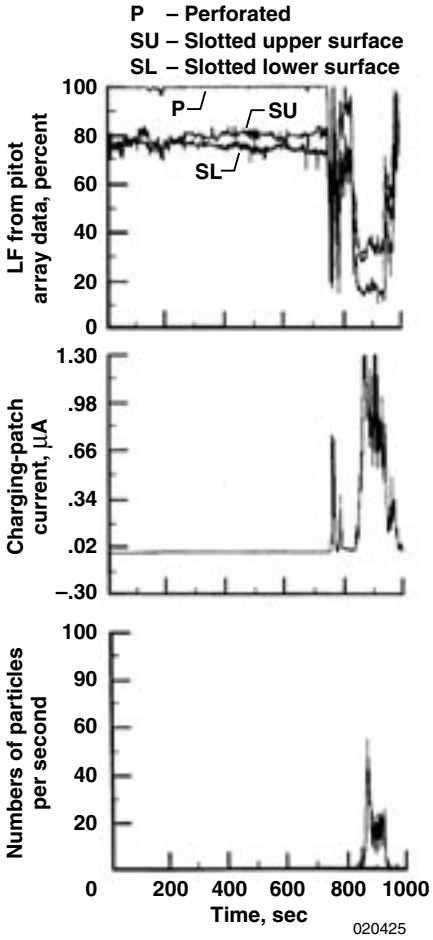

Figure 4.6-6. Example of concurrent traces of laminar flow percentage, charging patch current, and particle count, JetStar aircraft, $M = 0.75$, $h_p = 30000$ ft.

The high correlation among non-zero patch current, particle count, and LF traces is demonstrated. The LF P-trace is that for the perforated surface test article flown on the starboard wing glove, and the SU and SL traces are for the upper and lower surfaces of the slotted test article flown on the port wing glove. The concurrent traces show that LF loss on cloud entry is immediate, as is LF resumption on cloud exit. The charge patch current is also correlated with the number of particles encountered per second.

4.6.4 CONCLUSIONS

Flight experience indicates that cloud encounters indeed degrade the extent of LF. Experience shows that both laser spectrometers and charge patches are effective in detecting particle concentrations. The charge-patch shows considerable promise as an inexpensive, easy-to-read, rugged, stand-alone device for particle detection on non-afterburning platforms, but considerable attention to detail is required to calibrate the device for each application. In every LF flight program where clouds were penetrated, the charge-patch was found to function reliably. Especially useful results for correlation of patch reading with LF were obtained with the patches data in the JetStar LEFT, the F14-A VSTFE, and the LearJet NLF research programs. The charge-patch also detected thin cirrus in the Boeing 757 HLFC program, but minor unexplained anomalies were observed in the signal level. Additional theoretical and applied research is recommended, to fully characterize the charging phenomenon analytically and optimize the charge-patch concept for general diagnostic use on production LF-configured aircraft. Also, the patch has not yet worked on afterburning platforms.

For continued investigation into the mechanics of LF loss in particle concentrations, laser particle spectrometers for measuring the spectra (size and concentration) of the ambient particles will continue to be very useful.

5.0 Conducting Flight Tests

5.1 Flight test procedures (flight safety aspects)

5.1.1 Infrared thermographic requirements (transport type aircraft)

For the flight trials of the laminar flow nacelles flight tested on the DLR flight test vehicle VFW614/ATTAS this aircraft was operated subject to slight restrictions regarding the flight envelope compared with the basic VFW614. For the NLF and HLF nacelle flight-demonstrations, the maximum permissible flight Mach number was restricted to Ma_∞ = MMO = 0.62 because of the increased nacelle diameter compared with the standard production nacelle. For the latter the maximum operating Mach number is Ma_∞ = MMO = 0.65 [90].

Environmental phenomena associated with space and solar effects play an important role in the application of the infrared thermographic technique in flight testing, especially with reference to laminar flow nacelles [70]. First, there is the effect of space. Space as background is at a low temperature, which is definitely lower than the temperature on any aircraft surface and this leads to heat radiation from the aircraft surfaces exposed to space, resulting in a reduction of the temperature on those surfaces. Second, there exists the effect of the ground (surface of the earth). The surface temperature of the earth is, in general, higher than the temperature of most aircraft surfaces for typical cruise altitudes $H > 20{,}000$ ft and for subsonic flight Mach numbers, excluding the visible core nozzle exit and the plug of the engine. Thus, components of the aircraft exposed to heat radiation from the ground will experience a temperature rise. With reference to a fan cowl of an engine nacelle, both of the above environmental influences result in a division of the fan cowl into an upper half, which is subjected to heat radiation into space with an associated temperature reduction; and a lower half, which is receiving heat radiation from the ground, leading to a temperature rise. Third, superimposed on the influences of the space and the ground is the effect of heat radiation from the sun. This causes heating of the aircraft surfaces exposed to the rays of the sun. The intensity and the incidence of the heat radiation from the sun essentially depends on the aircraft heading, i.e. the orientation of the aircraft with regard to the sun, the time of day, and the presence of high clouds above the aircraft. Under these complex conditions it is mandatory to install surface heating on the areas to be observed. About 400 W/m^2 is sufficient to achieve a temperature of 5 °C above the flow temperature, which in general results in infrared images of good quality and in short observation times.

In order to get good-quality images without surface heating, it is useful to keep a moderate descent rate for observation of the wing upper surface and a moderate climb rate for observations of the wing lower surface.

A problem, which is not excluded by surface heating, is the reflection (of low clouds or the surface of the earth) from the wing lower side observation area into the camera. These reflections can be excluded by multiple sampling of the infrared image with averaging and simultaneous change of bank angle of the aircraft. Thus, the radiation from the wing surface remains constant whereas the reflections are changing and excluded by averaging. The same procedure would help in the case of high-altitude clouds and observations on the wing upper surface.

5.1.2 Insect contamination avoidance

As already mentioned in chapter 3.1 for flight test purposes it might be useful to avoid insect contamination “naturally”. This can be achieved by a very early takeoff using the low temperatures and the dew in the morning. Helpful also is a wind speed above 10 to 20 kt. One of the best actions is to transfer the test flights to a dry desert-like region, if possible.

However, a commercial aircraft with a laminar flow system, whether it is natural laminar flow, laminar flow control or hybrid laminar flow control, will probably need a contamination-avoidance system that is

reliable and robust to protect the wing leading edge from insect impacts, [151]. This is especially true for aircraft with moderately or highly swept wings, where a few insect remains in the wrong spot could seriously reduce the amount of laminar flow on the wing and noticeably increase the aircraft drag. Elsenaar and Hassnoot [152] report that during the summer months laminar flow would be completely lost as a result of leading edge contamination without some sort of protection. To flight test a contamination avoidance system, the aircraft must be exposed to a level of insect concentration during the tests that it might be exposed to during a commercial flight under severe conditions. It must also be tested under other environmental flight conditions required by the FAA or other regulating agencies for airworthiness certification to which commercial aircraft are exposed such as rain, snow, freezing rain, temperature extremes, high humidity, etc.

Initial tests of a contamination avoidance system

Before each flight, the test article should be thoroughly cleaned of any dirt or insect remains. The anti-contamination system should be operational during takeoff to an altitude of approximately 500 ft above ground level (AGL). The aircraft then can be flown to nearby agricultural fields, forest, or other vegetation where the insect population is high. Low passes at takeoff and landing speeds are flown over the vegetation with the contamination systems operational. The anti-contamination systems are used from 500 ft AGL on both approach to, and climb from, the vegetation. The pilot's windscreen can be used as a real-time indication of the number of insects being encountered during these low passes. The low passes at commercial aircraft takeoff and landing approach speeds provide a realistic simulation.

After completing the low passes, the test aircraft climbs to the laminar flow test altitude. At that altitude, the aircraft levels off and obtains boundary layer transition data. The aircraft then returns to its home base, and any insect remains are mapped and heights measured.

Environmental conditions have a large influence on the population density of insects on any given day and should be considered for flight testing. Coleman compiled data on insect population density collected in Louisiana, USA and in England during the 1930s and 1940s, with regard to air temperature, wind velocity, and altitude [153]. The importance of ambient temperature, surface winds, and altitude on the occurrence of insect contamination was also noted by flight tests on a Bellanca Skyrocket at Langley Research Center, Virginia [80]. In figure 5.1.2-1, relative insect population density is plotted as a function of ground temperature; it shows a sharp rise in insect population with temperature, peaking near 25 °C (77 °F) for both the data from Coleman as well as the data from reference [80]. The data from reference [80] do show lower relative population densities at other temperatures, however.

In figure 5.1.2-2, the relative population density is shown as a function of surface-wind velocity from references [153, 80]. The peak population density is at 4 to 8 mph (6-13 km/hr); above 20 mph (32 km/hr), the population density is significantly reduced. In figure 5.1.2-3, the insect population densities from references [153, 80] are shown as a function of altitude; these show a sharp decline as altitude increases, as would be expected.

The data suggests that for best results, flight testing of a contamination avoidance system for insect protection should be done for air temperature between 70 and 90 °F (21 and 32 °C), altitudes at 50 ft (15 m) or less and wind velocities less than 15 mph (24 km/hr). It also suggests that at low temperatures, ≈7 °C (45 °F) and below, wind velocities above ≈ 20 mph (32 km/hr) and altitude above ≈ 300 ft (100 m), a contamination avoidance system might not be necessary.

The anti-contamination system must also be shown to be rugged and reliable when exposed to more severe environmental conditions typical of a commercial airline. An example of this type of testing was performed by the NASA JetStar Leading Edge Flight Test (LEFT) aircraft.

After the initial functional and checkout flight tests, the aircraft made a series of 62 simulated airline service flights based from Atlanta, Georgia in July 1985, Pittsburgh, Pennsylvania in September 1985, and Cleveland, Ohio in January and February 1986, [28, 29]. The objectives of these flights were to obtain

operational data on LFC leading edge systems in the commercial airline environment. The ground rules were that the aircraft would be operated like a scheduled airline in that it would use the scheduled dispatch, queue up with other airlines, use the ATC system, and fly during peak traffic hours. The aircraft would also be left outdoors overnight, exposed to the elements, and operate with on/off LFC systems. During these flights, the aircraft was exposed to heat, cold, humidity, insects, rain, freezing rain, snow, ice, and light icing conditions. Conventional ground equipment was used for de-icing the aircraft of snow and ice, fig. 5.1.2-4.

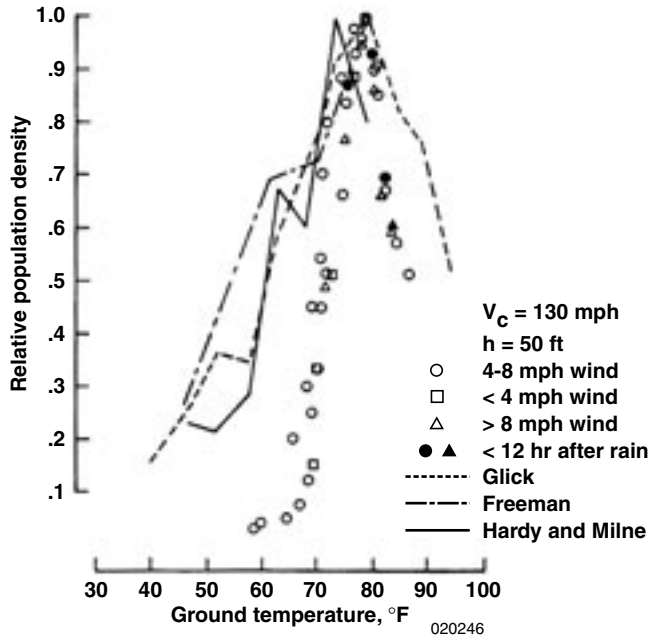

Figure 5.1.2-1. Relative insect population density compared with ground temperature.

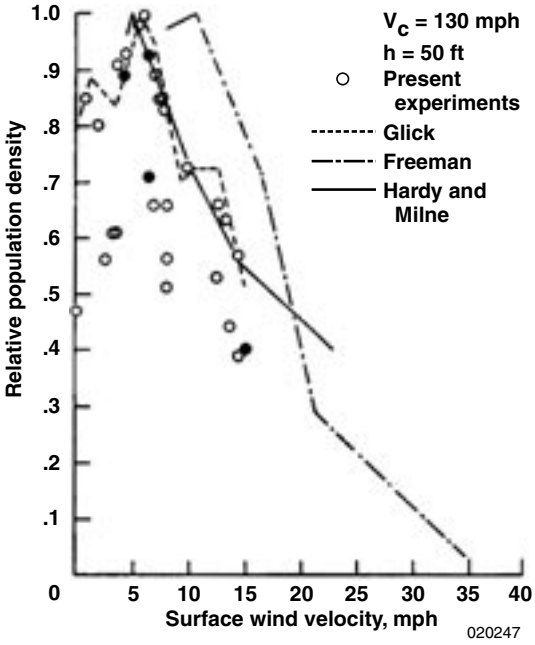

Figure 5.1.2-2. Relative insect population density compared with surface-wind velocity.

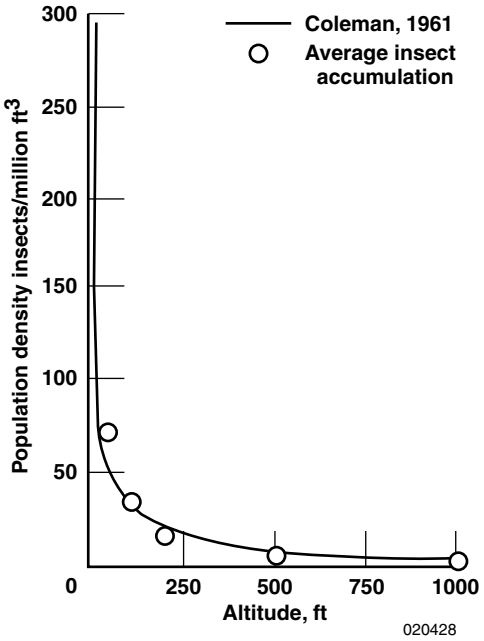

Figure 5.1.2-3. Insect population densities compared with altitude.

EC87 165-1

Figure 5.1.2-4. Photo of deicing JetStar LEFT aircraft after overnight freezing rain storm.

5.2 Anti-contamination systems

5.2.1 FLUID FILM PROTECTION

To achieve the full low-drag potential of a laminar wing, it is essential that the wing surface – especially the leading edge – be kept clean of insects. One method of avoiding insect contamination is to apply a fluid film on the leading edge surface by fluid transpiration. The fluid film reduces the adhesive forces by orders of magnitude. The insects stick much less to the surface and are moved downstream by means of the fluid layer and the shear stress of the flow. A special advantage of such a fluid transpiration anti-contamination system is the possibility of combining this system with a fluid transpiration anti-icing system which has already been certified for several commuter and general aviation aircraft [154]. Figure 5.2.1-1 shows a schematic cross-section of such a system. Two titanium skins form a closed chamber which is divided into two parts by a flexible membrane. The front skin, with the shape of the wing leading edge, has been made porous by laser drilled holes with a typical diameter of 60 microns and a spacing of 0.5–1.0 mm.

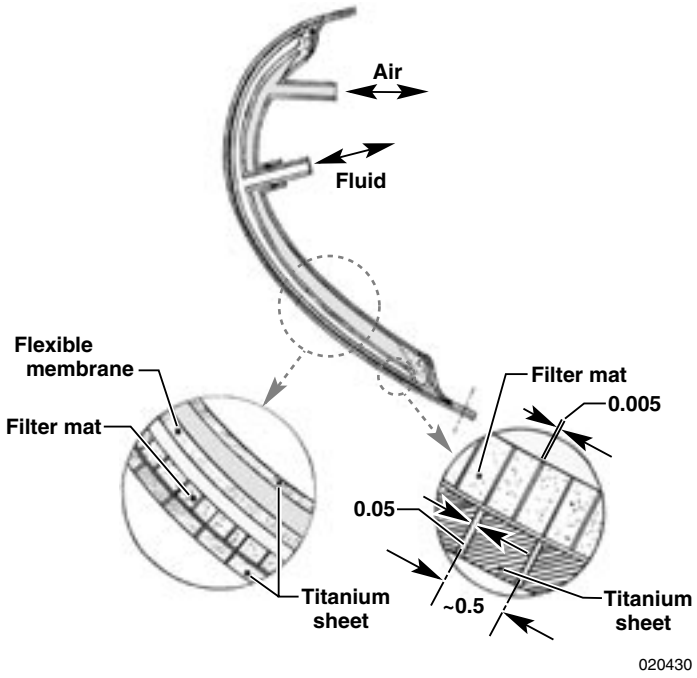

Figure 5.2.1-1. Schematic cross-section of an anti-contamination-de-icing system.

During the active phase of system operation, a mixture of glycol alcohol and water is forced into the front chamber and excreted through the porous surface, forming a closed film, which is then moved downstream by the flow shear stresses. During the passive phase of the system, the fluid flow is stopped and the rear chamber is pressurized with compressed air, moving the membrane to the front and thus forcing out the rest of the fluid and sealing the porous titanium skin.

For flight testing of such a system on the Dornier Do 228 DLR test aircraft, an anti-contamination panel with a spanwise extent of one meter was installed in the outboard part of a NLF glove. The central part of the glove was taken as reference, see [49].

Figure 5.2.1-2 shows a typical upper-side infrared image of an anti-contamination flight test. On the outboard part of the glove, protected by the anti-contamination system, the boundary layer remains laminar except for a single turbulent wedge. The reference zone in the central part of the image is, on the other hand, characterized by many turbulent wedges. Downstream of 10 percent of chord only some small laminar regions are left. This amount of contamination was achieved during six take offs and landings. The effectiveness of the contamination system can be defined by comparing the number of wedges in the anti-contamination zone with those in the reference zone. Typically, in the anti-contamination zone only 10 percent of the insects are observed as compared with the reference zone of comparable size. Summarizing, the tests show that a fluid transpiration anti-contamination system can successfully be used to reduce the insect contamination considerably.

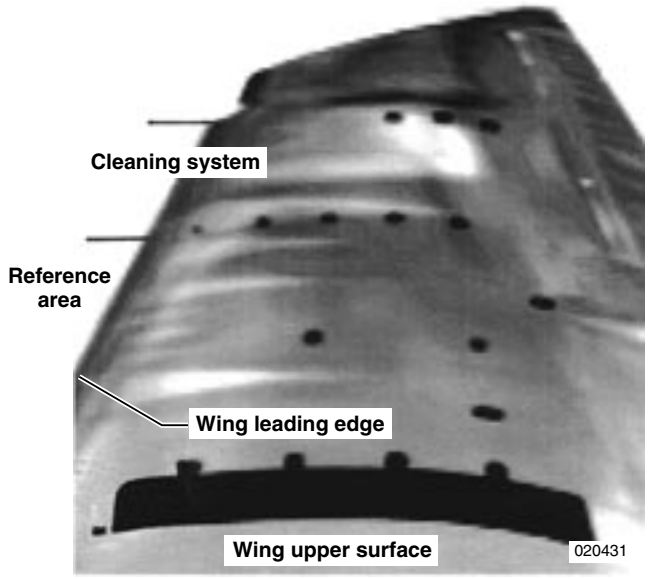

Figure 5.2.1-2. Infrared image of the efficiency of a fluid transpiration anti-contamination system installed on the DLR Do228.

5.2.2 SHIELD PROTECTION

Another method of protecting a laminar flow leading edge from insects and other forms of contamination is to use a Krueger flap-type retractable shield, fig. 5.2.2-1. The shield could also be used as a high-lift device and for anti-icing during takeoff and landing and then retracted after it was no longer needed. One such shield was used successfully on a modified JetStar aircraft during simulated LFC airline service for 26 flights based out of Pittsburgh, PA in September and 23 flights based out of Cleveland, Ohio during February [28, 29]. During these flights, cleaning of the test article between flights was not performed. The shield proved to be very effective. Only five insect hits were observed on the LFC surface; those occurred on an inboard region that was not protected by the flap because of the geometry of the flap and the swept wing.

A disadvantage of using a Krueger flap device, such as the one used on the JetStar, is the loss of laminar flow on the lower surface of the wing. However, maintenance on the aircraft would be much easier. Access to fuel tanks, fuel pumps, and other hardware in the wing should be improved as compared to an aircraft with a fully-laminar-flow lower wing surface.

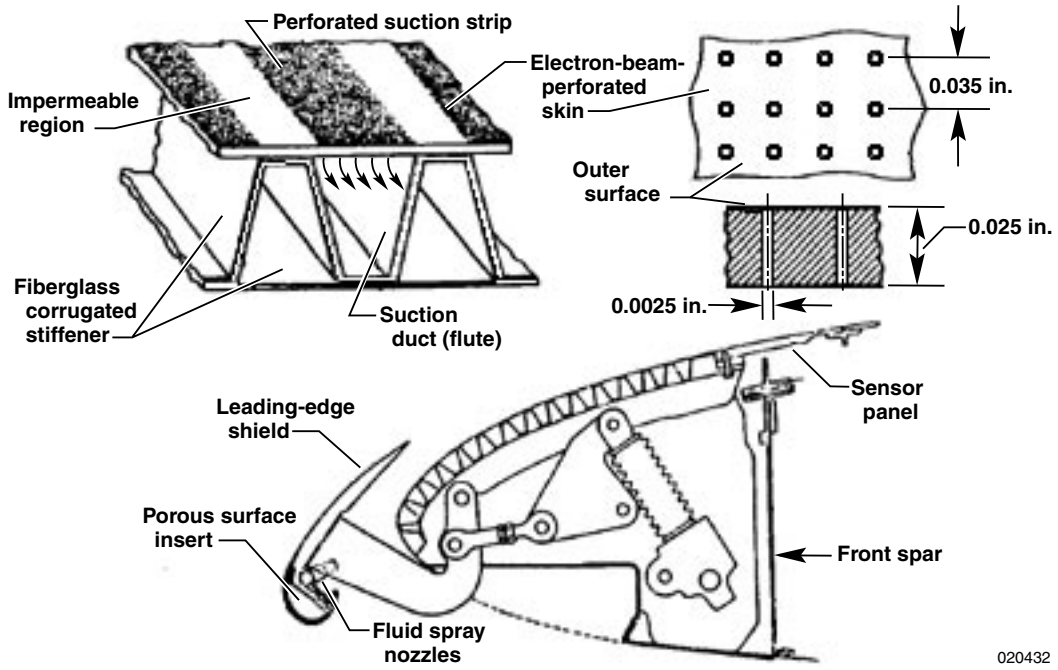

Figure 5.2.2-1. Cross-section of leading edge shield.

5.2.3 MECHANICAL DEVICES

Well-known in the glider pilots' community and often used at competitions are mechanical cleaning devices. A small mechanical shop in Austria manufacturing these devices has constructed a special mechanical cleaner for the Dornier Do 228 laminar flow glove.

After activating, the cleaning process runs up automatically. The "insect cleaner" is driven to the wing tip by aerodynamic forces and retracted by a thin wire, electrically driven, see figure 5.2.3-1. In combination with the fluidic system a 100-percent protection against insects is available. But then the aircraft has to be equipped with an additional system, which is far from a fully developed system in the present state of development.

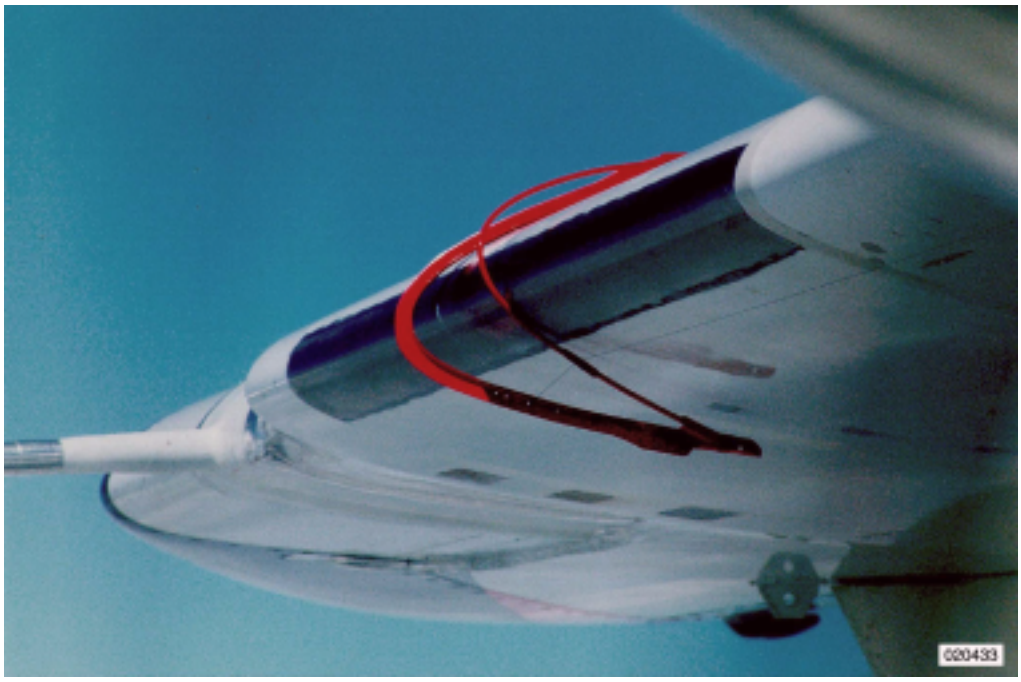

Figure 5.2.3-1. Mechanical cleaning system active during test flight.

6.0 Conclusions

This AGARDograph has been written to provide the future researcher in laminar flow with information on flight test techniques, related instrumentation, environmental effects, and flight procedures. Many techniques have been described to measure the location of boundary layer transition, from the very simple to the more complex. References are included to previous works for the reader to explore. Instrumentation has been described. Environmental effects have been noted. Procedures for flight test maneuvers have been included.

Flight test measurement techniques for the investigation of laminar boundary layer flow over aerodynamic surfaces cover a wide range of measurement techniques with focus on local as well as global measurements.

With the infrared thermographic technique firmly established as an indispensable tool for the global observation of laminar boundary layer flow on aerodynamic surfaces, no such in-flight measurement technique is available at present regarding surface static pressure measurements and surface shear stress measurements. Under development for future application is, however, the pressure-sensitive paint (PSP) technique which, if matured to a reliable airborne tool, could provide global information concerning the static pressure and shear stress on aerodynamic surfaces.

While a commercial laminar flow airplane is not a reality yet, much of the technology for one is in place. Laminar flow is a technology that has the potential for providing the greatest increase in aerodynamic efficiency. Up to this point in time, the risk of producing a commercially viable laminar flow aircraft appears greater than the benefit to manufacturers. Efforts are underway to remedy this situation.

This page has been deliberately left blank

Page intentionnellement blanche

7.0 References

[1] Stüper, J.; Untersuchungen von Reibungsschichten am fliegenden Flugzeug, Luftfahrtforschung, Band 11, Nr. 1., 1934, Also published in English as, *Investigation of Boundary Layers on an Airplane Wing in Free Flight*, NACA TM 751, 1934.

[2] Jones, B. M.; "Flight Experiments on the Boundary Layer," *Journal of the Aeronautical Sciences*, Vol. 5, No. 3, Jan. 1938. pp. 81–94.

[3] Bicknell, J.; *Determination of the Profile Drag of an Airplane Wing in Flight at High Reynolds Numbers*, NACA TR-667, 1939.

[4] Wetmore, J. W.; Zalovcik, J. A.; Platt, R. C.; *A Flight Investigation of the Boundary-Layer Characteristics and Profile Drag of the NACA 35-215 Laminar Flow Airfoil at High Reynolds Numbers*, NACA WR L-532, 1941.

[5] Zalovcik, J. A.; *Flight Investigation of Boundary-Layer and Profile-Drag Characteristics of Smooth Wing Sections of a P-47D Airplane*, ACR No. L5H11a, October 1945.

[6] Smith, F.; Higton, D. J.; *Flight Tests on King Cobra FZ-440 to Investigate the Practical Requirements for the Achievement of Low Profile Drag Coefficients and a Low Drag Airfoil*, ARC-R/M-2375, 1950.

[7] Plascott, R. H.; Higton, D. J.; Smith, F.; Bramwell, A. R.; *Flight Test on Hurricane II, Z.3687 Fitted With Special Wings of 'Low-Drag' Design*, ARC-R/M-2546, N21208, RAE-AERO-2153, RAE-AERO-2090, 1952.

[8] Pfenninger, W.; *Summary of Laminar Boundary Layer Control Research*, WADC Technical Report 56-111, April 1957.

[9] Banner, R. D.; McTigue, J. G.; Petty, G., Jr.; *Boundary-Layer-Transition Measurements in Full-Scale Flight*, NACA RM H58E28, July 1958.

[10] McTigue, J. G.; Overton, J. D.; Petty, G., Jr.; *Two Techniques for Detecting Boundary-Layer Transition in Flight at Supersonic Speeds and at Altitudes Above 20,000 Feet*, NASA TN D-18, August 1959.

[11] Pfenninger, W.; Groth, E.; "Low drag boundary layer suction experiments in flight on a wing glove of an F-94A airplane with suction through a large number of fine slots." *Boundary Layer and Flow Control*, Vol. 2, London, 1961, pp 981–999.

[12] Carmichael, R. F.; Pelke, D. E.; *In-Flight Noise Measurements Performed on the X-21A Laminar Flow Aircraft*, NOR-64-81, 1964.

[13] Pfenninger, W.; "Some results from the X-21 Program. part 1- Flow Phenomena at the Leading Edge of Swept Wings," *AGARD Recent Development Boundary Layer Research*, Pt. IV, May 1965.

[14] Whites, R. C.; Sudderth, R. W.; Wheldon, W. G.; "Laminar flow control on the X-21," *Astronautics and Aeronautics*, Vol. 4, Jul. 1966, P. 38–43.

[15] Landeryou, R. R.; Porter, P. G.; *Further Tests of a Laminar Flow Swept Wing With Boundary Layer Control by Suction*, C of A. Report Aero. No. 192, The College of Aeronautics Cranfield, May 1966.

[16] Fisher, D. F.; Peterson, J. B., Jr.; "Flight Experience on the Need and Use of Inflight Leading Edge Washing for a Laminar Flow Airfoil," AIAA Paper 78-1512, 1978.

[17] Runyan, L. J.; Steers, L. L.; "Boundary Layer Stability Analysis of a Natural Laminar Flow Glove on the F-111 TACT Airplane," *Viscous Flow Drag Reduction Symposium*, Dallas, Texas, Technical Papers, November 7–8, 1979, pp. 17–32.

[18] Steers, L. L.; "Natural Laminar Flow Flight Experiment," NASA CP-2172, NASA Langley Research Center, *Advanced Aerodynamics and Active Controls*, February 1981, pp. 135–144.

[19] Montoya, L. C.; Steers, L. L.; Trujillo, B.; "F-111 TACT Natural Laminar Flow Glove Flight Results," NASA CP-2208, NASA Langley Research Center, *Advanced Aerodynamics: Selected NASA Research*, December 1981, pp. 11–20.

[20] Meyer, R. R., Jr.; Jennett, L. A.; *In-Flight Surface Oil-Flow Photographs With Comparisons to Pressure Distribution and Boundary-Layer Data*, NASA TP-2395, April 1985.

[21] Holmes, B. J.; Obara, C. J.; Yip, L. P.; *Natural Laminar Flow Experiments on Modern Aircraft Surfaces*, NASA TP 2256, June 1984.

[22] Wentz, W. H., Jr.; Nyenhuis, R.; Ahmed, A.; "Natural Laminar Flow Flight Experiments on a Swept-Wing Business Jet," AIAA PAPER 84-2189, 1984.

[23] Wentz, W. H., Jr.; Ahmed, A.; Nyenhuis, R.; "Further Results of Natural Laminar Flow Flight Test Experiments," SAE PAPER 850862, 1985.

[24] Rozendaal, R. A.; *Natural Laminar Flow Flight Experiments on a Swept Wing Business Jet – Boundary Layer Stability Analysis*, NASA CR 3975, May 1986.

[25] Fisher, D. F.; Fischer, M. C.; "Development Flight Tests of JetStar LFC Leading-Edge Flight Test Experiment," NASA CP 2487, Pt.1, pp 117–140, 1987.

[26] Powell, A. G.; "The Right Wing of the L.E.F.T. Airplane," NASA CP 2487, Pt.1, pp 141–161, 1987.

[27] Davis, R. E.; Maddalon, D. V.; Wagner, R. D.; "Performance of Laminar-Flow Leading Edge Test Articles in Cloud Encounters," NASA CP 2487, Pt.1, pp 163–193, 1987.

[28] Maddalon, D. V.; Fisher, D. F.; Jennett, L. A.; Fischer, M. C.; "Simulated Airline Service Experience With Laminar-Flow Control Leading-Edge Systems," NASA CP 2487, Pt.1, pp 195–218, 1987.

[29] Maddalon, D. V.; Braslow, A. L.; *Simulated-Airline-Service Flight Tests of Laminar-Flow Control With Perforated-Surface Suction System*, NASA TP 2966, March 1990.

[30] Körner, H.; Horstmann, K. H.; Köster, H.; Quast, A.; Redeker, G.; "Laminarization of Transport Aircraft Wings - A German View," AIAA 87-0085, 1987, pp. 1–12.

[31] Körner, H.; Horstmann, K. H.; "The Use of Airplanes for Aerodynamic Research at DFVLR-Institute for Design-Aerodynamics," *Proc. Symposium on 80th Birthday of B.H. Goethert*. UTSI, Tullahoma/USA, 1987, pp. 8–14.

[32] Runyan, L. J.; Bielak, G. W.; Behbehani, R. A.; Chen, A. W.; Rozendaal, R. A.; *The 757 NLF Glove Flight Test Results*, NASA CP 2487, Pt. 3, 1987, pp 795–818.

[33] Meyer, R. R.; Trujillo, B. M.; Bartlett, D. W.; "F-14 VSTFE and Results of the Cleanup Flight Test Program," NASA CP-2487, NASA Langley Research Center, *Research in Natural Laminar Flow and Laminar-Flow Control*, Part 3, December 1987, pp. 819–844.

[34] Anderson, B. T.; Meyer, R. R., Jr.; Chiles, H. R.; *Techniques Used in the F-14 Variable-Sweep Transition Flight Experiment*, NASA TM-100444, 1988, also AIAA 88-2110.

[35] Collier, F. S., Jr.; Bartlett, D. W.; Wagner, R. D.; Tat, V. V.; Anderson, B. T.; "Correlation of Boundary Layer Stability Analysis With Flight Transition Data," Presented at the *IUTAM 3rd Symposium on Laminar-Turbulent Transition*, Toulouse, France, September 11–15, 1989, Springer-Verlag, Berlin and London, 1990, pp. 337–346.

[36] Anderson, B. T. and Meyer, R. R., Jr.; *Effects of Wing Sweep on Boundary-Layer Transition for a Smooth F-14A Wing at Mach Numbers From 0.700 to 0.825*, NASA TM-101712, May 1990.

[37] Anderson, B. T. and Meyer, R. R., Jr.; *Effects of Wing Sweep on In-Flight Boundary-Layer Transition for a Laminar Flow Wing at Mach Numbers From 0.60 to 0.79*, NASA TM-101701, July 1990.

[38] Anderson, B. T.; Meyer, R. R., Jr.; Chiles, H. R.; "Techniques Used in the F-14 Variable-Sweep Transition Flight Experiment," *Journal of Aircraft*, Vol. 28, No. 10, October 1991.

[39] Horstmann, K. H.; Quast, A.; Redeker, G.; "Flight and Wind-Tunnel Investigations on Boundary Layer Transition at Reynolds Numbers up to 10 to the 7th," *Proceedings of the 16th ICAS Congress*, Vol. 2, Jerusalem, Israel, Aug. 28–Sept. 2, 1988, pp. 979–986.

[40] Horstmann, K. H.; Redeker, G.; Quast, A.; Dressler, U.; Bieler, H.; "Flight Tests With a Natural Laminar Flow Glove on a Transport Aircraft," AIAA 90-3044, 1990.

[41] Redeker, G.; Horstmann, K. H.; Köster, H.; Thiede, P.; Szodruch, J.; "Design of a Natural Laminar Flow Glove for a Transport Aircraft," AIAA-90-3043, 1990.

[42] Körner, H., "Natural Laminar Flow Research for Subsonic transport aircraft in the FRG," ICAS-88.4.1.1, *International Congress of Aeronautical Sciences*, 16th, Jerusalem, Aug 28–Sept 2, 1988.

[43] Kreplin, H.-P. and Hoehler, G., "Surface hot film measurements at ATTAS laminar glove," In Tech. Univ. Berlin, *Measurement Technology for Flight Tests* p 1–11, May 1991, (In German).

[44] Horstmann, K. H.; Quast, A.; Redeker, G.; "Flight and Wind-Tunnel Investigations on Boundary-Layer Transition," *Journal of Aircraft*, Vol. 27, No. 2, Feb. 1990, pp. 146–150.

[45] Horstmann, K. H.; Redeker, G.; Miley, S. J.; "Flight Investigation of Tollmien-Schlichting Waves on an Aircraft Wing," ICAS-90-6.1.2, 1990, *Proceedings 17th ICAS Congress*, Stockholm, Sweden, Vol. 1, Sept. 9–14, 1990, pp. 186–192.

[46] Horstmann, K. H.; Miley, S. J.; "Comparison of Flight and Wind Tunnel Investigations of Tollmien-Schlichting-Waves on an Aircraft Wing," DGLR/AAAF/RaeS *First European Forum on Laminar Flow Technology*, DGLR-Bericht 92-06, 1992, pp. 45–51.

[47] Wohlrath, W.; Echtle, H.; Dick, P.; Welte, D.; Stock, H. W.; Moeken, B.; Horstmann, K. H.; Müller, R.; Rohardt, C.-H.; Quast, A.; "Design and Flight Test Evaluation of a Laminar Wing Glove on a Commuter Aircraft," *Proc. 19th ICAS Congress*, Vol. 2, 1994, pp. 1231–1240.

[48] Horstmann, K. H.; Müller, R.; Dick, P.; Wohlrath, W.; "Flugversuche Am Laminarhandschuh der DO228," *DGLR-Jahrbuch 1992*, pp. 1249–1258 (in German).

[49] Horstmann, K. H.; Körner, H.; Wagner, B.; Welte, D.; "Natural Laminar Flight Test Investigation for Commuter Aircraft Application," *Proc. Second European Forum on Laminar Flow Technology*, 1996, pp. 2.19–2.30.

[50] Bulgubure, C. and Arnal, D.; "DASSAULT Falcon 50 Laminar Flow Flight Demonstrator," *Proc. First European Forum on Laminar Flow Technology*, 1992, pp. 11–18.

[51] Sacco, G. and Piaggio, I. A. M. R.; "Piaggio P180: Natural Laminar Flow Test and In-service Experience," *Proc. Second European Forum on Laminar Flow Technology*, 1996, pp. 11.1–11.26.

[52] Voogt, N.; "Flight Testing a Fokker 100 Test Aircraft with Laminar Flow Glove," *Proc. Second European Forum on Laminar Flow Technology*, 1996, pp. 2.3–2.14.

[53] Bolsunovsky, A.; Buzoverya, N.; Kotscheev, A.; Cheryemukkin, G.; Shapiro, A.; Zavershnev, Yu.; Tabolov, M.; Turitschev, V.; "The Tu-22M Flying Test Bed for Laminar Flow Studies," *Proc. Second European Forum on Laminar Flow Technology,* 1996, pp. 2.15–2.18.

[54] Thibert, J. J.; Quast, A.; Robert, J. P., "The A320 Laminar Fin Programme," *Proc. First European Forum on Laminar Flow Technology*, 1992, pp. 19–25.

[55] Kühn, W., Strahmann, T.; Höhler, G.; Quast, A.; "Measuring Techniques for A320 Fin Reference and Hybrid Laminar Flight Tests," *Proc. Second European Forum on Laminar Flow Technology*, 1996, pp. 7.16–7.28.

[56] Ghnassia, J. C.; Kuon, T.; Rouquière, V.; "Flight Test Installation for Laminar Fin A320 Demonstrator," *Proc. Second European Forum on Laminar Flow Technology*, 1996, pp. 10.50–10.54.

[57] Henke, R.; Capbern, P.; Davies, A. J.; Hinsinger, R.; Santana, J. L.; The "A320 HCF Fin-Programme: Objectives and Challenges," *Proc. Second European Forum on Laminar Flow Technology*, 1996, pp. 12.3–12.11.

[58] Schrauf, G. H.; "Evaluation of the A320 Hybrid Laminar Fin Experiment," *European Congress on Computational Methods in Applied Sciences and Engineering*, Barcelona, 11–14, Sept. 2000, http://www.imamod.ru/jour/conf/ECCOMAS_2000/PDF/725.pdf, accessed Sept. 9, 2001.

[59] Becker, S.; Durst, F.; Lienhart, H.; "Laser Doppler Anemometer for In-Flight Velocity Measurements on Airplane Wings," *AIAA Journal*, Vol. 37, No. 6, June 1999.

[60] Ewald, B., Durst, F.; Krause, E.; Nitsche, W.; "In-flight measuring techniques for laminar flow wing development," *Proc. First European Forum on Laminar Flow Technology*, 1992, pp.110–122, also in *ZFW*, Vol.17, No.5, 1993, pp.294–310.

[61] Anderson, B. T. and Bohn-Meyer, M.; *Overview of Supersonic Laminar Flow Control Research on the F-16XL Ships 1 and 2*, NASA TM-104257, October 1992. Also presented as SAE Paper 92-1994 at the Aerotech '92 Conference, Anaheim, California, October 5–8, 1992.

[62] Marshall, L. A.; *Boundary Layer Transition Results From the F-16XL-2 Supersonic Laminar Flow Control Experiment*, NASA TM-1999-209013, Dec. 1999.

[63] Bertelrud, A.; de la Tova, G.; Hamory, P. J.; Young, R.; Noffz, G. K.; Dodson, M.; Graves, S. S.; Diamond, J. K.; Bartlett, J. E.; Noack, R.; Knoblock, D.; *Pegasus® Wing-Glove Experiment to Document Hypersonic Crossflow Transition: Measurement System and Selected Flight Results*, NASA/TM-2000-209016, Jan. 2000. Also AIAA Paper 2000-0505.

[64] Obara, C. J.; Hastings, E. C.; Schoenster, J. A.; Parrott, T. L.; Holmes, B. J.; "Natural Laminar Flow Flight Experiments on a Turbine Engine Nacelle Fairing," AIAA PAPER 86-9756, 1986.

[65] Hastings, E. C., Jr.; Faust, G. K.; Mungur, P.; Obara, C. J.; Dodbele, S. S.; Schoenster, J. A.; Jones, M. G.; "Status Report on a Natural Laminar-Flow Nacelle Flight Experiment," *Research in Natural Laminar Flow and Laminar-Flow Control*, NASA CP 2487, Part 3, pp 887–914, 1987.

[66] Shipley, P. P.; Birch, N. T.; Riedel, H.; Horstmann, K. H.; Lücking, P.; "A European Collaborative NLF Nacelle Flight Demonstrator," *Proc. First European Forum on Laminar Flow Technology*, 1992, pp. 26–34.

[67] Riedel, H. and Sitzmann, M., "Flight Investigations of the Effect of Yaw on the Intake and Fan Nozzle Flow of a Natural Laminar Flow Nacelle," *Proc. RAe Soc. Conference Engine-Airframe Integration*, 11–16 October 1996, pp. 10.1–10.14. Also in *The Aeronautical Journal of the Royal Aeronautical Society*, October 1997, pp. 389–397.

[68] Barry, B.; Parke, S. J.; Bown, N. W.; Riedel, H.; Sitzmann, M.; "The flight testing of natural and hybrid laminar flow nacelles," ASME Paper 94-GT-408, 1994.

[69] Mullender, A. J. and Riedel, H.; "A Laminar Flow Nacelle Flight Test Programme," Rolls Royce Report PNR92295, 1996. Also published in *Proc. Second European Forum on Laminar Flow Technology*, 1996, pp. 2.31–2.49.

[70] Riedel, H. and Sitzmann, M.; *Some Aspects of Flow Transition Detection When Flight Testing Carbon Fibre Composite Conventional and Laminar Flow Nacelles*, DLR-FB-1999-37, 1999.

[71] Tegarden, F. W.; "Hybrid Laminar Flow Nacelles - A Test for the Future," *Proc. RAe Soc. Conference Engine-Airframe Integration*, 11–16 October 1996, pp.11.1–11.10.

[72] Bilstein, R. E.; *Orders of magnitude: A History of the NACA and NASA*, *1915–1990*, NASA-SP-4406, 1989.

[73] Chuprun, J. and Cahill, J. F.; "LFC on Large Logistics Aircraft." *Astronaut. & Aeronaut*., vol. 4, no. 7, 1966, pp. 58–62.

[74] Braslow, A. L.; *A History of Suction-Type Laminar-Flow Control With Emphasis of Flight Research*, Monographs in Aerospace History, No. 13, 1999.

[75] Schlichting, H.; *Grenzschicht-Theorie*, publisher Verlag G. Braun, Karlsruhe, 1951. (Also published as *Boundary Layer Theory*, various editions, McGraw-Hill.)

[76] Cumpsty, N. A. and Head, M. R.; "The calculation of three-dimensional turbulent boundary layers, Part II: Attachment line flow on an infinite swept wing;" ARC-28180; FM-3730, 1966. Also published in *The Aeronautical Quart*., Vol. 18, 1967, pp. 150–164.

[77] Poll, D. I. A.; "Transition in the infinite swept attachment-line boundary layer," *The Aeronautical Quart*, Vol. 30, Nov. 1979, pp. 607–629.

[78] Granville, P. S.; "The Calculation of the Viscous Drag of Bodies of Revolution." *Navy Department; The David Taylor Model Basin, report no. 849*, NS715-102, 1953.

[79] Schrauf, G. and Horstmann, K. H.; "Linear Stability Theory Applied to Natural and Hybrid Laminar Flow Experiments." *Aerodynamic Drag Reduction Technologies*, Ed. Peter Thelde, CEAS/DragNet, European Drag Reduction Conference 2000, Berlin, June 2000, pp 157–163.

[80] Croom, Cynthia C. and Bruce J. Holmes; *Flight Evaluation of an Insect Contamination Protection System for Laminar Flow Wings*, SAE 850860, 1985.

[81] Goldstein, S.; *A note on roughness*, Aeronautical Research Committee R & M No. 1763, (2539) 1936.

[82] Fage, A.; Preston, J. H.; "On transition from laminar to turbulent flow in the boundary layer," *Proc. Roy. Soc*. A 178, pp 201–227, 1941

[83] Hall, G.R.; *On the Mechanics of Transition Produced by Particles Passing Through an Initially Laminar Boundary Layer and the Estimated Effect on the LFC Performance of the X-21 Aircraft*. Northrop Corp., Oct., 1964.

[84] Pfenninger, Werner and Verlin D. Reed, "Laminar-Flow Research and Experiments," *Astronautics & Aeronautics*, Vol. 4, no. 7, pp. 44–50, July 1966.

[85] Snyder, J.L.; *Effect of Clouds in LFC Applications*, Ops/Analysis, Directorate of Operations Research Report, AD454476, Deputy of Studies and Analysis, Systems Engineering Group, Research and Technology Division, Wright-Patterson Air Force Base, Ohio, Dec. 1964

[86] Jasperson, W.H.; Nastrom, G.D.; Davis, R.E.; and Holdeman, J.D.; *GASP Cloud- and Particle-Encounter Statistics, and their Application to LFC Studies-Volume II: Appendixes*, NASA TM-85835, 1984.

[87] Jasperson, W.H.; Nastrom, G.D.; Davis, R.E.; and Holdeman, J.D.; "GASP Cloud Encounter Statistics: Implications for Laminar Flow Control Flight." *AIAA J. Aircraft*, vol. 21, no. 11, Nov, 1984, pp 851–857.

[88] Wuest, W.; Pool, A.; Sanderson, K. C.; "Pressure and Flow Measurement," *AGARD Flight Test Instrumentation Series*, AGARD-AG-160, Volume 11, 1980.

[89] Bouchardy, A. M.; Durand, G.; Gauffre, G.; "Processing of infrared thermal images for aerodynamic research;" Technical Report No 1983-32, *SPIE International Conference Geneva*, 18–22 April 1983, ONERA, Chatillon.

[90] Riedel, H.; Horstmann, K.-H.; Ronzheimer, A.; Sitzmann, M.; "Aerodynamic Design of a Natural Laminar Flow Nacelle and the Design Validation by Flight Testing," *Aerospace Science and Technology*, Vol. 2, No. 1, 1998.

[91] Chiles, H.R.; Johnson, J.B.; *Development of a Temperature-Compensated Hot-Film Anemometer System for Boundary-Layer Transition Detection on High-Performance Aircraft*, NASA TM-86732, 1985.

[92] Chiles, H.R.; *The Design and Use of a Temperature-Compensated Hot-Film Anemometer System for Boundary-Layer Flow Transition Detection on Supersonic Aircraft*, NASA TM-100421, 1988.

[93] vanDam,C.P.; Los, S.M.; Miley, S.J.; Roback,V.E.; Yip, L.P.; Bertelrud, A.; Vijgen, P.M.H.W.; "In-Flight Boundary-Layer State Measurements on a High-Lift System: Slat," *AIAA Journal of Aircraft*, Vol. 34, No. 6, 1997, p. 748–756.

[94] Whitehead, J.H.; Harris, F.K.; Lytle, C.D.; "Research Requirements for a Real-Time Flight Measurements and Data Analysis System for Subsonic Transport High-Lift Research," *Proceedings of 39th International Instrumentation Symposium*, Albuquerque, NM, May 1993, pp 635–647.

[95] Bruun, H.H.; *Hot-Wire Anemometry–Principles and Signal Analysis*, Oxford University Press, ISBN 0 19 856342 6, 1995.

[96] Kaups, K.; Cebeci, T.; "Compressible Laminar Boundary Layers With Suction on Swept and Tapered Wings," *Journal of Aircraft*, Vol. 14, No. 7, pp.661–667, 1977.

[97] Seitz, A.; Horstmann, K.-H.; "Propagation of Tollmien-Schlichting waves in a wing boundary layer," to be published in: *Notes on Numerical Fluid Mechanics*, NNFM, Springer Verlag, 2002.

[98] Miley, S.J.; Horstmann, K.H.; *Data Report of Flight and Wind Tunnel Investigations of Tollmien-Schlichting Waves on an Aircraft Wing, Part I, Report IB 129-91/18*, Institute for Design Aerodynamics, DLR, Braunschweig, 1991.

[99] King, L.V.; "On Convection of Heat from Small Cylinders in a Stream of Fluid with Applications to Hot-Wire Anemometry," *Phil. Trans. Roy. Soc. London*, vol. 214, no. 14, p.373, 1914.

[100] George-Falvy, Dezso; "In Quest of the Laminar-Flow Airliner: Flight Experiments on a T-33 Jet Trainer," *IXth Hungarian Aeronautical Science Conference*, Budapest, Hungary, Nov. 1988.

[101] Fisher, David F. and Dougherty, N. Sam, Jr.; "Flight and Wind-Tunnel Correlation of Boundary Layer Transition on the AEDC Transition Cone," AGARD CP-339, paper no. 5, Feb. 1983.

[102] Fisher, David F. and Dougherty, N. Sam, Jr.; *In-Flight Transition Measurements on a 10° Cone at Mach Numbers From 0.5 to 2.0*, NASA TP 1971, June 1982.

[103] Damania, R. B. and Thomas, N. S. W.; "Flight Testing of a Wing Section With Laminar Flow Control," *Journal of the Aeronautical Society of India*, Vol. 36, pp. 95–106, May 1984.

[104] Hughes, J. P.; Brumby, R. E.; and Belevtsov, N.; "Flow Visualization From the Ground Up" AIAA 83-2691. Presented at the 2nd AIAA, AHS, IES, SETP, SFTE, and DGLR Flight Testing Conference, Las Vegas, Nevada, Nov. 1983.

[105] Fisher, David F.; Richwine, David M.; and Banks, Daniel W.; *Surface Flow Visualization of Separated Flows on the Forebody of an F-18 Aircraft and Wind-Tunnel Model*, NASA TM-100436, 1988.

[106] Fisher, David F. and Meyer, Robert R., Jr.; "Flow Visualization Techniques for Flight Research," *Flight Test Techniques*, AGARD CP-452, 1988. Also published as NASA TM 100455.

[107] Fisher, David F.; Del Frate, John H.; and Richwine, David M.; *In-Flight Flow Visualization Characteristics of the NASA F-18 High Alpha Research Vehicle at High Angles of Attack*, NASA TM 4193, May 1990.

[108] Klein, E. J.; *Application of Liquid Crystals to Boundary Layer Flow Visualization*, AIAA paper 68-376, 1968.

[109] Klein, Enrique J.; "Liquid Crystals in Aerodynamic Testing," *Astronautics & Aeronautics*, pp. 70–73, July 1968.

[110] Klein, E. J. and Margozzi, A. P.; *Exploratory Investigation on the Measurement of Skin Friction by Means of Liquid Crystals*, NASA TM X-1774, May 1969.

[111] Holmes, Bruce J.; Gall, Peter D.; Croom, Cynthia C.; Manuel, Gregory S.; and Kelliher, Warren C.; *A New Method for Laminar Boundary Layer Transition Visualization in Flight---Color Changes in Liquid Crystal Coatings*, NASA TM-87666, 1986.

[112] Holmes, Bruce J, and Obara, Clifford J.; *Advances in Flow Visualization Using Liquid-Crystal Coatings*, SAE Paper 871017, 1987.

[113] Gall, P. D. and Holmes, B. J.; "Liquid Crystals for High-Altitude In-Flight Boundary Layer Flow Visualization," AIAA Paper 86-2592, *General Aviation Technology Conference*, Anaheim, Calif., 1986.

[114] Smith, Stephen, C.; "Use of Shear-Sensitive Liquid Crystals for Surface Flow Visualization," *J. of Aircraft*, Vol. 29, No. 2, pp. 289–293, March-April 1992.

[115] http://www.hallcrest.com/industrial/industrial.pdf, Hallcrest, Inc., 1820 Pickwick Lane, Glenview, Il 60025, Industrial products, Temperature indicators.

[116] Reda, D. C., "Liquid Crystals for Unsteady Surface Shear Stress Visualization," AIAA Paper 88-3841. Presented at the 1st National Fluid Dynamics Congress, Cincinnati, OH, July 1988.

[117] Main-Smith, J.D.; "Chemical Solids as Diffusible Coating Films for Visual Indications of Boundary-Layer Transition in Air and Water," *ARC* British R&M No.2755, February 1950.

[118] Tanner, D. D., "Chemical Solid Sublimation Technique in ARO/Ames-Operated Facilities for Visual Indication of Boundary Layer Transition," TM No. 43, September 1972, ARO, Inc.

[119] Owen, P. R. and Ormerod, A. O.; "Evaporation from the Surface of a Body in an Airstream," ARC British R&M 2875, September 1951.

[120] Obara, C.J.; "Sublimating Chemical Technique for Boundary-Layer Flow Visualization in Flight Testing," *AIAA Journal of Aircraft*, Vol. 25, No. 6, June 1988, pages 493–498.

[121] Braslow, Albert L. and Knox, Eugene C.; *Simplified Method for Determination of Critical Height of Distributed Roughness Particles for Boundary Layer Transition at Mach Numbers From 0 to 5*, NACA TN-4363, 1958.

[122] Curry, Robert E.; Meyer, Robert R. Jr.; O'Connor, Maureen; *The Use of Oil for In-Flight Flow Visualization*, NASA Technical Memorandum 84915, Revised January 1984, August 1983.

[123] Schuemann, Wil; Sailplane Modifications,
http://w3.iac.net/~feguy/soaring_symposia/72-modif.html Accessed April 16, 2001.

[124] Bown, N.W.; *In-flight Boundary Layer Studies on Laminar Flow Nacelles*, PhD Thesis, University of Oxford, 1995.

[125] Dixon, T.; *VFW614-M45 Datum Flow Nacelle Dynamic Vibration Test*, Hurel-Dubois UK Ltd., Report No. HDSR/LAM/014, 1st October 1991.

[126] Riedel, H.; Sitzmann, M.; "In-flight Investigations of Atmospheric Turbulence," *AST* Vol. 2, No. 5, 1998, pp 310–319.

[127] Arnzt, K.-D.; *Flugmessungen zur Ermittlung von Druck- und Geschwindigkeitsschwankungen in der Atmosphäre mit der LFU-205*. Studienarbeit Nr. 91/3. Institut für Entwurfsaerodynamik, DLR Braunschweig, Germany, 1991.

[128] Suttan, J.; Baumann, M.; Frühling, S.; Erb, P.; Becker, S.; Müller, W.; "In-flight Research on Laminar-Turbulent Transition." *2nd European Forum on Laminar Flow Technology*, 10-18 to 10-41, Bordeaux, France, 1996.

[129] Jentink, H.W.; Beversdorff, M.; Förster, W.; "Laser Anemometry for In-flight Flow Investigations." *Proceedings of International Congress on Instrumentation in Aerospace Simulation Facilities* ICIASF'95, Wright Patterson AFB, Ohio, USA, July 1995. IEEE Publication 95CH34827-23.

[130] Bulgubure, C.; Arnal, D.; "Dassault Falcon 50 Laminar Flow Flight Demonstrator." Paper 92-01-003. *First European Forum on Laminar Flow Technology*, Hamburg, Germany, 1992.

[131] Steiner, R.; Rhyne, R.H.; "Atmospheric Turbulence and Airplane Response in Convective-Type Clouds." *Journal of Aircraft*, Vol. 1, No. 1, February, 1964.

[132] Viehweger, G.; Rebstock, R.; Stahl, B.; Wichmann, K.; Becker, W.; Kronen, R.; Distelrath, D.; *Der Kryo-Kanal Köln (KKK) der DLR (Stand 1992)*. DLR-Mitt. 93-10, 1993.

[133] Viehweger, G.; "Das Konzept des Kryo-Kanal Köln der DLR. Ergebnisse der Kraftmessungen mit dem AGARD-Kryo-Modell und Untersuchungen zur Strömungsqualität." *AG STAB Jahresbericht 1991*, S. 83-84, pp 83 and 84.

[134] Althaus, D.; *Niedriggeschwindigkeitsprofile*,. Friedr. Vieweg & Sohn Verlagsgesellschaft mbH, Braunschweig/Wiesbaden, Germany, 1996.

[135] Fowell, L.R. and Antonatos, P.P.; "Some Results From the X-21A Program-Part2: Laminar Flow Flight Test Results on the X-21A." *Recent Developments in Boundary Layer Research—Part IV*, AGARDograph 97, 1965.

[136] Imyanitov, I.M.; *Aircraft Electrification in Clouds and Precipitation*. FTD-HC-23-544-70, U.S. Air Force, Apr. 1971. (Available from DTIC as AD 726581.)

[137] Tanner, R.L. and Nanevicz, J.E.; *Precipitation Charging and Corona-Generated Interference in Aircraft*. AFCRL 336, Technical Report 73, U.S. Air Force, April, 1961.

[138] Boulay, J.L. and LaRoche, P.; *Aircraft Potential Variations in Flight*. ONERA TP No. 1982-11, 1982.

[139] Caranti, J. and Illingworth, A.J.; "Static Charging by Collisions With Ice Particles." *Proceedings International Aerospace Conference on Lightning and Static Electricity*, Volume 2, Culham Lab. (Abingdon, Oxon., England), 1982, pp E2-1–E2-6

[140] Campbell, R.E. and McPherson, J.P.; "Airborne Cloud Detector." *NASA Tech Briefs*, vol. 9, no. 2, Summer, 1985, pp 63–64.

[141] Varley, D.J; *Cirrus Particle Distribution Study, Part 1*. AFGL-TR-78-0192, U.S. Air Force Surveys in Geophysics No. 394, Aug. 7, 1978. (Available from DTIC as AD A061485.)

[142] Cohen, I.D.; *Cirrus Particle Distribution Study, Part 8*. AFGL-TR-81-0316, U.S. Air Force Surveys in Geophysics No. 437, Oct. 28, 1981. (Available from DTIC as AD A118715.)

[143] Davis, R.E.; Maddalon, D.V.; Wagner, R.D.; Fisher, D.F.; and Young, R.; *Evaluation of Cloud Detection Instruments and Performance of Laminar Flow Leading Edge Test Articles during NASA Leading Edge Flight Test Program*. NASA TP-2888, 1989.

[144] Povinelli, F.P.; Klineberg, J.M.; and Kramer, J.J.; "Improving Aircraft Energy Efficiency." *Astronaut. & Aeronaut.*, vol. 14, no. 2, Feb. 1976, pp 18–31.

[145] Wagner, R.D. and Fischer, M.C.; "Developments in the NASA Transport Aircraft Laminar Flow Program." AIAA-83-0090, Jan. 1983. Presented at AIAA 21st Aerospace Sciences Meeting, January 1983, Reno, Nevada.

[146] Fischer, M.C.; Wright, A.S., Jr.; and Wagner, R.D.; "A Flight Test of Laminar Flow Control Leading-Edge Systems." AIAA-83-2508, Oct., 1983. Presented at AIAA Aircraft Design, Systems, and Technology Meeting, October 1983, Fort Worth, Texas.

[147] Maddalon, D.V.; "Hybrid Laminar Flow Control Flight Research" *Research and Technology*. NASA TM-4331, 1991, p. 47.

[148] Bhutiani, P.K.; Keck, D.F.; Lahti, D.J.; and Stringas, M.J.; "Investigating the Merits of Hybrid Laminar Flow Nacelle." *The Leading Edge*, General Electric Corp., Spring, 1993, pp 32–35.

[149] Lee, C.C.; Wusk, M.S.; and Obara, C.J.; *Flight Experiments Studying the Growth of Disturbances in the Laminar Boundary Layer*. SAE Technical Paper 901979, 1990.

[150] Fisher, B.D.; Phillips, M.R.; and Maier, L.M.; *Joint NASA/USAF Airborne Field Mill, Program-Operational and Safety Considerations During Flights of Lear 28 Airplane in Adverse Weather*. AIAA Paper 92-4093, 1992.

[151] Atkins, P. B.; *Wing Leading Edge Contamination by Insects*, ARL Flight Note 17, Oct. 1951.

[152] Lachmann, G. C., *Aspects of Insect Contamination in Relation to Laminar Flow Aircraft*, C. P. No, 484, Aeronautical Research Council, London, UK, April 1959.

[153] Coleman, W. S., "Roughness Due to Insects," in *Boundary Layer and Flow Control*, edit by G.V. Lachman, Vol. 2, Pergamon Press, 1961, pp 682–747.

[154] Aircraft Advisory AC-20-73, "Aircraft Ice Protection," dated 04/21/71 FAA, U. S. Department of Transportation, 65 pages. Available on the Web at: http://www.airweb.faa.gov/Regulatory_and_Guidance_Library/rgAdvisoryCircular.nsf/6410bb5d2de0236685256a35006d56b1/9f168f3dadf6e71b862569ae006d3577?OpenDocument&ExpandSection=-2#_Section2 Accessed 9/3/2001.

Annex – AGARD and RTO
Flight Test Instrumentation and Flight Test Techniques Series

1. Volumes in the AGARD and RTO Flight Test Instrumentation Series, AGARDograph 160

Volume Number	Title	Publication Date
1.	Basic Principles of Flight Test Instrumentation Engineering (Issue 2) Issue 1: Edited by A. Pool and D. Bosman Issue 2: Edited by R. Borek and A. Pool	 1974 1994
2.	In-Flight Temperature Measurements by F. Trenkle and M. Reinhardt	1973
3.	The Measurements of Fuel Flow by J.T. France	1972
4.	The Measurements of Engine Rotation Speed by M. Vedrunes	1973
5.	Magnetic Recording of Flight Test Data by G.E. Bennett	1974
6.	Open and Closed Loop Accelerometers by I. McLaren	1974
7.	Strain Gauge Measurements on Aircraft by E. Kottkamp, H. Wilhelm and D. Kohl	1976
8.	Linear and Angular Position Measurement of Aircraft Components by J.C. van der Linden and H.A. Mensink	1977
9.	Aeroelastic Flight Test Techniques and Instrumentation by J.W.G. van Nunen and G. Piazzoli	1979
10.	Helicopter Flight Test Instrumentation by K.R. Ferrell	1980
11.	Pressure and Flow Measurement by W. Wuest	1980
12.	Aircraft Flight Test Data Processing – A Review of the State of the Art by L.J. Smith and N.O. Matthews	1980
13.	Practical Aspects of Instrumentation System Installation by R.W. Borek	1981
14.	The Analysis of Random Data by D.A. Williams	1981
15.	Gyroscopic Instruments and Their Application to Flight Testing by B. Stieler and H. Winter	1982
16.	Trajectory Measurements for Take-off and Landing Test and Other Short-Range Applications by P. de Benque D'Agut, H. Riebeek and A. Pool	1985
17.	Analogue Signal Conditioning for Flight Test Instrumentation by D.W. Veatch and R.K. Bogue	1986
18.	Microprocessor Applications in Airborne Flight Test Instrumentation by M.J. Prickett	1987
19.	Digital Signal Conditioning for Flight Test by G.A. Bever	1991

2. Volumes in the AGARD and RTO Flight Test Techniques Series, AGARDograph 300

Volume Number	Title	Publication Date
AG237	Guide to In-Flight Thrust Measurement of Turbojets and Fan Engines by the MIDAP Study Group (UK)	1979

The remaining volumes are published as a sequence of Volume Numbers of AGARDograph 300.

1.	Calibration of Air-Data Systems and Flow Direction Sensors by J.A. Lawford and K.R. Nippress	1988
2.	Identification of Dynamic Systems by R.E. Maine and K.W. Iliff	1988
3.	Identification of Dynamic Systems – Applications to Aircraft Part 1: The Output Error Approach by R.E. Maine and K.W. Iliff Part 2: Nonlinear Analysis and Manoeuvre Design by J.A. Mulder, J.K. Sridhar and J.H. Breeman	 1986 1994
4.	Determination of Antenna Patterns and Radar Reflection Characteristics of Aircraft by H. Bothe and D. McDonald	1986
5.	Store Separation Flight Testing by R.J. Arnold and C.S. Epstein	1986
6.	Developmental Airdrop Testing Techniques and Devices by H.J. Hunter	1987
7.	Air-to-Air Radar Flight Testing by R.E. Scott	1992
8.	Flight Testing under Extreme Environmental Conditions by C.L. Henrickson	1988
9.	Aircraft Exterior Noise Measurement and Analysis Techniques by H. Heller	1991
10.	Weapon Delivery Analysis and Ballistic Flight Testing by R.J. Arnold and J.B. Knight	1992
11.	The Testing of Fixed Wing Tanker & Receiver Aircraft to Establish Their Air-to-Air Refuelling Capabilities by J. Bradley and K. Emerson	1992
12.	The Principles of Flight Test Assessment of Flight-Safety-Critical Systems in Helicopters by J.D.L. Gregory	1994
13.	Reliability and Maintainability Flight Test Techniques by J.M. Howell	1994
14.	Introduction to Flight Test Engineering Edited by F. Stoliker	1995
15.	Introduction to Avionics Flight Test by J.M. Clifton	1996
16.	Introduction to Airborne Early Warning Radar Flight Test by J.M. Clifton and F.W. Lee	1999
17.	Electronic Warfare Test and Evaluation by H. Banks and R. McQuillan	2000
18.	Flight Testing of Radio Navigation Systems by H. Bothe and H.J. Hotop	2000
19.	Simulation in Support of Flight Testing by D. Hines	2000

20.	Logistics Test and Evaluation in Flight Testing by M. Bourcier	2001
21.	Flying Qualities Flight Testing of Digital Flight Control Systems by F. Webster and T.D. Smith	2001
22.	Helicopter/Ship Qualification Testing by D. Carico, R. Fang, R.S. Finch, W.P. Geyer Jr., Cdr. (Ret.) H.W. Krijns and K. Long	2002
23.	Flight Test Measurement Techniques for Laminar Flow by D. Fisher, K.H. Horstmann and H. Riedel	2003

At the time of publication of the present volume, the following volumes are in preparation:

Optical Air Flow Measurement in Flight

Flight Testing of Night Vision Systems

Unique Aspects of Flight Testing of Unmanned Aerial Vehicles/Unmanned Combat Aerial Vehicles

Aircraft-Stores Certification Testing

Selection of a Flight Test Instrumentation System

Testing of Precision Airdrop Systems

Flight Testing of Tactical Laser Systems

This page has been deliberately left blank

Page intentionnellement blanche

REPORT DOCUMENTATION PAGE

1. Recipient's Reference	2. Originator's References	3. Further Reference	4. Security Classification of Document
	RTO-AG-300 AC/323(SCI-040)TP/45 Volume 23	ISBN 92-837-1107-6	UNCLASSIFIED/ UNLIMITED

5. Originator

Research and Technology Organisation
North Atlantic Treaty Organisation
BP 25, F-92201 Neuilly-sur-Seine Cedex, France

6. Title

Flight Test Measurement Techniques for Laminar Flow

7. Presented at/Sponsored by

the Flight Test Technology Team (FT3) of the Systems Concepts and Integration Panel (SCI) of RTO.

8. Author(s)/Editor(s)	9. Date
Multiple	October 2003
10. Author's/Editor's Address	**11. Pages**
Multiple	130

12. Distribution Statement

There are no restrictions on the distribution of this document. Information about the availability of this and other RTO unclassified publications is given on the back cover.

13. Keywords/Descriptors

Aerodynamic characteristics	Hot-wire	Separation
ATTAS	Hybrid laminar flow control	Sublimating chemicals
Boundary layer flow	Infrared imaging	Surface properties
Boundary layer transition	JetStar	Surface temperatures
Data acquisition	Laminar flow control	Test facilities
Emitted fluid	Liquid crystal	Transonic characteristics
Flight maneuvers	Oil flow	Traversing pitot
Flight tests	Raised-pitot	X-21
Hot-film		

14. Abstract

This AGARDograph provides information on flight test techniques, instrumentation, environmental effects, and flight procedures that have been used successfully in laminar flow research. Many techniques are described for measuring the location of boundary layer transition in-flight, from the very simple to the more complex. References to previous works are included for readers to explore. Specific instrumentation for flight is described and the unique environmental effects of flight noted. Procedures for flight test maneuvers are also included.

Techniques discussed cover both local and global measurements. Some of the local flow techniques include surface temperatures, hot-film and hot-wire anemometry, raised-pitot, and traversing surface pitot. Global flow techniques include the infrared imaging, oil flow, liquid crystal, sublimating chemicals, and emitted fluid techniques. Some of the environmental concerns discussed include atmospheric particulate (ice crystals) and turbulence. Flight test procedures for infrared imaging and for insect contamination avoidance are described.

This page has been deliberately left blank

Page intentionnellement blanche

NORTH ATLANTIC TREATY ORGANISATION

RESEARCH AND TECHNOLOGY ORGANISATION

BP 25
F-92201 NEUILLY-SUR-SEINE CEDEX • FRANCE
Télécopie 0(1)55.61.22.99 • E-mail mailbox@rta.nato.int

DIFFUSION DES PUBLICATIONS

RTO NON CLASSIFIEES

Les publications de l'AGARD et de la RTO peuvent parfois être obtenues auprès des centres nationaux de distribution indiqués ci-dessous. Si vous souhaitez recevoir toutes les publications de la RTO, ou simplement celles qui concernent certains Panels, vous pouvez demander d'être inclus soit à titre personnel, soit au nom de votre organisation, sur la liste d'envoi.

Les publications de la RTO et de l'AGARD sont également en vente auprès des agences de vente indiquées ci-dessous.

Les demandes de documents RTO ou AGARD doivent comporter la dénomination « RTO » ou « AGARD » selon le cas, suivi du numéro de série. Des informations analogues, telles que le titre est la date de publication sont souhaitables.

Si vous souhaitez recevoir une notification électronique de la disponibilité des rapports de la RTO au fur et à mesure de leur publication, vous pouvez consulter notre site Web (www.rta.nato.int) et vous abonner à ce service.

CENTRES DE DIFFUSION NATIONAUX

ALLEMAGNE
Streitkräfteamt / Abteilung III
Fachinformationszentrum der
Bundeswehr (FIZBw)
Friedrich-Ebert-Allee 34, D-53113 Bonn

BELGIQUE
Etat-Major de la Défense
Département d'Etat-Major Stratégie
ACOS-STRAT – Coord. RTO
Quartier Reine Elisabeth
Rue d'Evère, B-1140 Bruxelles

CANADA
DSIGRD2
Bibliothécaire des ressources du savoir
R et D pour la défense Canada
Ministère de la Défense nationale
305, rue Rideau, 9e étage
Ottawa, Ontario K1A 0K2

DANEMARK
Danish Defence Research Establishment
Ryvangs Allé 1, P.O. Box 2715
DK-2100 Copenhagen Ø

ESPAGNE
SDG TECEN / DGAM
C/ Arturo Soria 289
Madrid 28033

ETATS-UNIS
NASA Center for AeroSpace
Information (CASI)
Parkway Center, 7121 Standard Drive
Hanover, MD 21076-1320

FRANCE
O.N.E.R.A. (ISP)
29, Avenue de la Division Leclerc
BP 72, 92322 Châtillon Cedex

GRECE (Correspondant)
Defence Industry & Research
General Directorate, Research Directorate
Fakinos Base Camp, S.T.G. 1020
Holargos, Athens

HONGRIE
Department for Scientific Analysis
Institute of Military Technology
Ministry of Defence
H-1525 Budapest P O Box 26

ISLANDE
Director of Aviation
c/o Flugrad
Reykjavik

ITALIE
Centro di Documentazione
Tecnico-Scientifica della Difesa
Via XX Settembre 123
00187 Roma

LUXEMBOURG
Voir Belgique

NORVEGE
Norwegian Defence Research Establishment
Attn: Biblioteket
P.O. Box 25, NO-2007 Kjeller

PAYS-BAS
Royal Netherlands Military
Academy Library
P.O. Box 90.002
4800 PA Breda

POLOGNE
Armament Policy Department
218 Niepodleglosci Av.
00-911 Warsaw

PORTUGAL
Estado Maior da Força Aérea
SDFA – Centro de Documentação
Alfragide
P-2720 Amadora

REPUBLIQUE TCHEQUE
DIC Czech Republic-NATO RTO
VTÚL a PVO Praha
Mladoboleslavská ul.
Praha 9, 197 06
Česká republika

ROYAUME-UNI
Dstl Knowledge Services
Kentigern House
Room 2246
65 Brown Street
Glasgow G2 8EX

TURQUIE
Milli Savunma Bakanlığı (MSB)
ARGE ve Teknoloji Dairesi Başkanlığı
06650 Bakanliklar – Ankara

AGENCES DE VENTE

NASA Center for AeroSpace Information (CASI)
Parkway Center, 7121 Standard Drive
Hanover, MD 21076-1320
ETATS-UNIS

The British Library Document Supply Centre
Boston Spa, Wetherby
West Yorkshire LS23 7BQ
ROYAUME-UNI

Canada Institute for Scientific and Technical Information (CISTI)
National Research Council
Acquisitions, Montreal Road, Building M-55
Ottawa K1A 0S2, CANADA

Les demandes de documents RTO ou AGARD doivent comporter la dénomination « RTO » ou « AGARD » selon le cas, suivie du numéro de série (par exemple AGARD-AG-315). Des informations analogues, telles que le titre et la date de publication sont souhaitables. Des références bibliographiques complètes ainsi que des résumés des publications RTO et AGARD figurent dans les journaux suivants :

Scientific and Technical Aerospace Reports (STAR)
STAR peut être consulté en ligne au localisateur de
ressources uniformes (URL) suivant:
http://www.sti.nasa.gov/Pubs/star/Star.html
STAR est édité par CASI dans le cadre du programme
NASA d'information scientifique et technique (STI)
STI Program Office, MS 157A
NASA Langley Research Center
Hampton, Virginia 23681-0001
ETATS-UNIS

Government Reports Announcements & Index (GRA&I)
publié par le National Technical Information Service
Springfield
Virginia 2216
ETATS-UNIS
(accessible également en mode interactif dans la base de
données bibliographiques en ligne du NTIS, et sur CD-ROM)

NORTH ATLANTIC TREATY ORGANISATION

RESEARCH AND TECHNOLOGY ORGANISATION

BP 25
F-92201 NEUILLY-SUR-SEINE CEDEX • FRANCE
Télécopie 0(1)55.61.22.99 • E-mail mailbox@rta.nato.int

DISTRIBUTION OF UNCLASSIFIED RTO PUBLICATIONS

AGARD & RTO publications are sometimes available from the National Distribution Centres listed below. If you wish to receive all RTO reports, or just those relating to one or more specific RTO Panels, they may be willing to include you (or your Organisation) in their distribution.

RTO and AGARD reports may also be purchased from the Sales Agencies listed below.

Requests for RTO or AGARD documents should include the word 'RTO' or 'AGARD', as appropriate, followed by the serial number. Collateral information such as title and publication date is desirable.

If you wish to receive electronic notification of RTO reports as they are published, please visit our website (www.rta.nato.int) from where you can register for this service.

NATIONAL DISTRIBUTION CENTRES

BELGIUM
Etat-Major de la Défense
Département d'Etat-Major Stratégie
ACOS-STRAT – Coord. RTO
Quartier Reine Elisabeth
Rue d'Evère
B-1140 Bruxelles

CANADA
DRDKIM2
Knowledge Resources Librarian
Defence R&D Canada
Department of National Defence
305 Rideau Street
9th Floor
Ottawa, Ontario K1A 0K2

CZECH REPUBLIC
DIC Czech Republic-NATO RTO
VTÚL a PVO Praha
Mladoboleslavská ul.
Praha 9, 197 06
Česká republika

DENMARK
Danish Defence Research Establishment
Ryvangs Allé 1
P.O. Box 2715
DK-2100 Copenhagen Ø

FRANCE
O.N.E.R.A. (ISP)
29, Avenue de la Division Leclerc
BP 72
92322 Châtillon Cedex

GERMANY
Streitkräfteamt / Abteilung III
Fachinformationszentrum der Bundeswehr (FIZBw)
Friedrich-Ebert-Allee 34
D-53113 Bonn

GREECE (Point of Contact)
Defence Industry & Research General Directorate, Research Directorate
Fakinos Base Camp, S.T.G. 1020
Holargos, Athens

HUNGARY
Department for Scientific Analysis
Institute of Military Technology
Ministry of Defence
H-1525 Budapest P O Box 26

ICELAND
Director of Aviation
c/o Flugrad, Reykjavik

ITALY
Centro di Documentazione Tecnico-Scientifica della Difesa
Via XX Settembre 123
00187 Roma

LUXEMBOURG
See Belgium

NETHERLANDS
Royal Netherlands Military Academy Library
P.O. Box 90.002
4800 PA Breda

NORWAY
Norwegian Defence Research Establishment
Attn: Biblioteket
P.O. Box 25, NO-2007 Kjeller

POLAND
Armament Policy Department
218 Niepodleglosci Av.
00-911 Warsaw

PORTUGAL
Estado Maior da Força Aérea
SDFA – Centro de Documentação
Alfragide, P-2720 Amadora

SPAIN
SDG TECEN / DGAM
C/ Arturo Soria 289
Madrid 28033

TURKEY
Milli Savunma Bakanlığı (MSB)
ARGE ve Teknoloji Dairesi Başkanlığı
06650 Bakanliklar – Ankara

UNITED KINGDOM
Dstl Knowledge Services
Kentigern House, Room 2246
65 Brown Street
Glasgow G2 8EX

UNITED STATES
NASA Center for AeroSpace Information (CASI)
Parkway Center, 7121 Standard Drive
Hanover, MD 21076-1320

SALES AGENCIES

NASA Center for AeroSpace Information (CASI)
Parkway Center
7121 Standard Drive
Hanover, MD 21076-1320
UNITED STATES

The British Library Document Supply Centre
Boston Spa, Wetherby
West Yorkshire LS23 7BQ
UNITED KINGDOM

Canada Institute for Scientific and Technical Information (CISTI)
National Research Council
Acquisitions
Montreal Road, Building M-55
Ottawa K1A 0S2, CANADA

Requests for RTO or AGARD documents should include the word 'RTO' or 'AGARD', as appropriate, followed by the serial number (for example AGARD-AG-315). Collateral information such as title and publication date is desirable. Full bibliographical references and abstracts of RTO and AGARD publications are given in the following journals:

Scientific and Technical Aerospace Reports (STAR)
STAR is available on-line at the following uniform resource locator:
http://www.sti.nasa.gov/Pubs/star/Star.html
STAR is published by CASI for the NASA Scientific and Technical Information (STI) Program
STI Program Office, MS 157A
NASA Langley Research Center
Hampton, Virginia 23681-0001
UNITED STATES

Government Reports Announcements & Index (GRA&I)
published by the National Technical Information Service
Springfield
Virginia 2216
UNITED STATES
(also available online in the NTIS Bibliographic Database or on CD-ROM)

ISBN 92-837-1107-6